ISTANBUL TECHNICAL UNIVERSITY★ GRADUATE SCHOOL

NUMERICAL INVESTIGATION OF HEAT TRANSFER IN GENERIC GAS TURBINE BLADE WITH IMPINGEMENT COOLING UNDER HIGH CROSSFLOW EFFECT

M.Sc. THESIS

Sefa YILMAZ

Department of Mechanical Engineering

Heat and Fluid Programme

JUNE 2026

ISTANBUL TECHNICAL UNIVERSITY★ GRADUATE SCHOOL

NUMERICAL INVESTIGATION OF HEAT TRANSFER IN GENERIC GAS TURBINE BLADE WITH IMPINGEMENT COOLING UNDER HIGH CROSSFLOW EFFECT

M.Sc. THESIS

Sefa YILMAZ
(503231132)

Department of Mechanical Engineering

Heat and Fluid Programme

Thesis Advisor: Assoc. Prof. Dr. Sertaç ÇADIRCI

JUNE 2026

İSTANBUL TEKNİK ÜNİVERSİTESİ ★ LİSANSÜSTÜ EĞİTİM ENSTİTÜSÜ

YÜKSEK ÇAPRAZ AKIŞ ETKİSİ ALTINDA ÇARPMA JET SOĞUTMALI JENERİK BİR GAZ TÜRBİNİ KANADINDA ISI TRANSFERİNİN SAYISAL İNCELENMESİ

YÜKSEK LİSANS TEZİ

Sefa YILMAZ
(503231132)

Makina Mühendisliği Anabilim Dalı

Isı Akışkan Programı

Tez Danışmanı: Doç. Dr. Sertaç ÇADIRCI

HAZİRAN 2026

Sefa YILMAZ, a M.Sc. student of ITU Graduate School student ID 503231132, successfully defended the thesis/dissertation entitled "NUMERICAL INVESTIGATION OF HEAT TRANSFER IN GENERIC GAS TURBINE BLADE WITH IMPINGEMENT COOLING UNDER HIGH CROSSFLOW EFFECT", which he prepared after fulfilling the requirements specified in the associated legislations, before the jury whose signatures are below.

Thesis Advisor:	**Assoc. Prof. Dr. Sertaç ÇADIRCI** Istanbul Technical University	.....
Jury Members :	**Prof. Dr. Bayram ŞAHİN** Istanbul Technical University	.....
	Prof. Dr. Derya Burcu ÖZKAN Yıldız Technical University	.....

Date of Submission : 21 May 2026
Date of Defense : 10 June 2026

To my father,

FOREWORD

I would like to express my deepest and most sincere gratitude to my advisor, Assoc. Prof. Sertaç ÇADIRCI, for his invaluable guidance, insightful advice, unwavering support, and enduring patience throughout the course of this thesis. Above all, I am profoundly grateful for his dedication and efforts in transforming this project into an exceptionally enriching and memorable learning experience.

I would like to express my most heartfelt gratitude to my beloved wife, whose unwavering presence, patience, and support accompanied me throughout the entire thesis-writing process. Without her endless understanding, encouragement, and devotion, the completion of this study would not have been possible. I would like to express my sincere gratitude to my dear sisters and friends, who have always stood by me and offered their unwavering support throughout my life. Their encouragement, kindness, and constant presence have been a great source of strength and motivation for me.

Finally, I wish to express my profound longing and immeasurable gratitude to my late father Ahmet YILMAZ, the very reason for my existence, whose wisdom, guidance, and life lessons continue to illuminate my path.

May 2026 Sefa YILMAZ

TABLE OF CONTENTS

Page

FOREWORD ..... **ix**
TABLE OF CONTENTS ..... **xi**
ABBREVIATIONS ..... **xiii**
SYMBOLS ..... **xv**
LIST OF TABLES ..... **xvii**
LIST OF FIGURES ..... **xix**
SUMMARY ..... **xxi**
ÖZET ..... **xxv**
1. INTRODUCTION **1**
2. TYPES OF COOLING IN GAS TURBINE ENGINES **7**
2.1 Convective Cooling 8
2.2 Rib-Turbulated (Augmented Convective) Cooling 9
2.3 Pin-Fin Cooling 11
2.4 Film Cooling 11
2.5 Impingement Cooling 12
3. STUDIES ON JET IMPINGEMENT **17**
3.1 Fundamentals of Single Jet Impingement 17
3.2 Impingement on Concave (Leading-Edge) Surfaces 19
3.3 Impingement Arrays and Crossflow 21
3.4 Numerical Studies and Turbulence Modelling 25
3.5 Knowledge Gap and Focus of the Thesis 28
4. COMPUTATIONAL FLUID DYNAMICS **31**
4.1 Governing Equations of Fluid Flow 31
4.1.1 Continuity equation 31
4.1.2 Momentum equations 32
4.1.3 Energy equation 32
4.2 Reynolds Averaging and the RANS Equations 33
4.3 The k–ω SST Turbulence Model 35
4.3.1 Transport equation for the turbulence kinetic energy 35
4.3.2 Transport equation for the specific dissipation rate 36
4.3.3 Eddy viscosity 36
4.4 Justification of the k–ω SST Model for the Present Work 37
5. VALIDATION CASE **39**
5.1 Validation Case Introduction 39
5.1.1 Experimental rig 40
5.1.2 Leading-edge geometry 41
5.1.3 Crossflow configurations and test matrix 42
5.1.4 Heat-transfer measurement technique 43
5.2 Literature-Based CFD Model 45
5.2.1 Geometry, mesh generation and mesh-independency 45

5.2.2 Definition of the Reynolds and Nusselt numbers 48
5.2.3 Boundary conditions 49
5.2.4 Solver settings and convergence check 50
5.3 Literature Validation Results 52
6. CFD SIMULATIONS FOR CORRELATION 59
6.1 Methodology 59
6.2 Results and Correlation 61
6.3 Overall Heat-Transfer Characteristics 65
6.4 Effect of the Jet Reynolds Number 65
6.5 Effect of the Jet-to-Surface Spacing (H/D) 67
6.6 Effect of the Jet-to-Jet Pitch (P/D) 69
6.7 Correlation Performance and Physical Consistency 70
7. CONCLUSIONS AND RECOMMENDATIONS 71
7.1 Key Conclusions 71
7.2 Practical Implications 72
7.3 Recommendations for Future Work 73
REFERENCES 75
CURRICULUM VITAE 79

ABBREVIATIONS

CFD	**:** Computational Fluid Dynamics
DIN	**:** Deutsches Institut für Normung
DNS	**:** Direct Numerical Simulation
HP	**:** High-pressure (turbine stage)
ITLR	**:** Institut für Thermodynamik der Luft- und Raumfahrt
LES	**:** Large-Eddy Simulation
MAE	**:** Mean Absolute Error
MAPE	**:** Mean Absolute Percentage Error
NASA	**:** National Aeronautics and Space Administration
RANS	**:** Reynolds-Averaged Navier–Stokes
RMSE	**:** Root-Mean-Square Error
SIMPLE	**:** Semi-Implicit Method for Pressure-Linked Equations
SST	**:** Shear-Stress Transport (k–ω model variant)
TLC	**:** Thermochromic Liquid Crystal

SYMBOLS

A	: Jet exit area
C_s	: Streamwise jet-to-jet distance
D, D_{jet}	: Impingement jet diameter
D_{fc}	: Film-cooling hole diameter
d, d_j	: Generic jet diameter
F_1, F_2	: Blending functions of the SST model
G_x, G_z	: Crossflow and jet mass-flow velocities
h	: Local convective heat-transfer coefficient
H	: Jet-to-target separation distance
k	: Turbulent kinetic energy / thermal conductivity
L	: Jet-to-plate spacing
ℓ, l	: Length / characteristic distance
M	: Jet-to-crossflow velocity ratio
$\dot{m}$	: Total inlet mass-flow rate
$\dot{m}_c$, $\dot{m}_j$	: Crossflow and jet mass-flow rates
MAE	: Mean absolute error
MAPE	: Mean absolute percentage error
N	: Number of streamwise rows in an array
Nu	: Nusselt number
p	: Static pressure
P	: Jet-to-jet pitch
Pr	: Prandtl number
q	: Surface heat flux
R	: Leading-edge radius of curvature
R^2	: Coefficient of determination
Re	: Reynolds number
Re_D	: Jet Reynolds number based on D
Re_c	: Crossflow Reynolds number
Re_j	: Per-jet Reynolds number
RMSE	: Root-mean-square error

$\mathbf{S_{ij}}$: Mean strain-rate tensor

St : Stanton number

T : Temperature

$\mathbf{T_0}$: Initial wall temperature

$\mathbf{T_{ref}}$: Reference (flow) temperature

$\mathbf{T_w}$: Wall temperature

$\mathbf{T_{ind}}$: TLC indication temperature

t : Time

$\mathbf{t_{ind}}$: TLC indication time

u, $\mathbf{u_i}$: Velocity component(s)

$\mathbf{U_0}$: Crossflow free-stream velocity

$\mathbf{U_j}$: Mean jet velocity

x, y, z : Cartesian coordinates

$\mathbf{x_0}$, $\mathbf{y_0}$: Streamwise and spanwise hole spacings

$\mathbf{y^+}$: Dimensionless wall distance

Z, $\mathbf{Z_0}$: Jet-to-target standoff distance

α : Coefficient in the SST model

β, β* : Coefficients in the SST model

$\mathbf{\beta_{fc}}$: Film-cooling hole inclination angle

δ : Layer thickness

Δ : Difference / increment

ε : Turbulent dissipation rate

λ : Thermal conductivity

μ : Dynamic viscosity of air

$\mathbf{\mu_t}$: Turbulent (eddy) viscosity

ν : Kinematic viscosity

ρ : Fluid density

$\mathbf{\sigma_k}$, $\mathbf{\sigma_\omega}$: Turbulent Prandtl numbers for k and ω

$\mathbf{\tau_{ij}}$: Reynolds-stress tensor

ω : Specific turbulence dissipation rate

LIST OF TABLES

Page

Table 5.1 : Grid independence data: mesh size N, its reciprocal 1/N, and the average Nusselt number normalized by the L4 value. **47**
Table 5.2 : Mesh quality metrics for the selected reference mesh L4..... **48**
Table 5.3 : CFD vs. experiment [8] area average Nusselt number. **57**
Table 6.1 : CFD surface-averaged Nusselt numbers for the H/D=1.4 configurations. **62**
Table 6.2 : CFD surface-averaged Nusselt numbers for the H/D=2.7 configurations. **62**
Table 6.3 : CFD surface-averaged Nusselt numbers for the H/D=4.0 configurations. **63**
Table 6.4 : CFD surface-averaged Nusselt numbers for the H/D=5.3 configurations. **63**
Table 6.5 : Fit-quality parameters of the proposed correlation. **65**
Table 6.6 : Control runs for the correlation..... **70**

LIST OF FIGURES

Page

Figure 1.1 : Schematic of a simple-cycle gas turbine. **1**
Figure 1.2 : Ideal Brayton cycle on a temperature–entropy diagram..... **2**
Figure 1.3 : Evolution of turbine inlet temperature, blade material capability, and cooling-technology generations [1,3]. **3**
Figure 2.1 : Typical cooling techniques applied to a high-pressure turbine blade and vane [1]. **8**
Figure 2.2 : Schematic of a modern cooled HP turbine blade combining leading-edge impingement, multi-pass serpentine convective cooling with ribs, pin-fin cooling, and film cooling [3]. **8**
Figure 2.3 : Flow pattern in a rib-turbulated cooling channel showing recirculation zones and reattachment points [10]. **10**
Figure 2.4 : Flow regions of a single round jet impinging on a flat surface [12]. **13**
Figure 2.5 : Impingement cooling on a concave leading-edge surface of a turbine blade. **14**
Figure 2.6 : Impingement jet array with progressive crossflow accumulation along the streamwise direction [15]..... **15**
Figure 3.1 : Schematic of the model used by Chupp et al. [13]. **20**
Figure 5.1 : Schematic of the experimental rig used by Forster and Weigand [8]. .. **41**
Figure 5.2 : Leading-edge geometry of the perspex test model of Forster and Weigand [8]. **42**
Figure 5.3 : Geometry of numerical model used by Forster and Weigand [8]. **42**
Figure 5.4 : Three crossflow configurations realized by closing one, both, or zero lateral lids of the outlet plenum [8]. **43**
Figure 5.5 : Transient TLC measurement principle [8]. **44**
Figure 5.6 : Geometry of the present study: a) Leading-edge geometry, b) Spacing for impingement jet and film holes. **46**
Figure 5.7 : Detail of the hybrid mesh used in the simulations. **46**
Figure 5.8 : Variation of the normalized average Nusselt number Nu_{ave} / $Nu_{ave,L4}$ with the inverse mesh size 1/N for meshes L1–L5. ..... **47**
Figure 5.9 : Computational domain and boundary conditions used in the present simulations. **50**
Figure 5.10 : Convergence history of scaled residuals for Re_D = 30 000, H/D = 2.7, P/D = 4. ..... **51**
Figure 5.11 : Convergence history of jet Reynolds number for Re_D = 30 000, H/D = 2.7, P/D = 4. ..... **52**
Figure 5.12 : Convergence history of surface-averaged Nusselt number for Re_D = 30 000, H/D = 2.7, P/D = 4. ..... **52**
Figure 5.13 : y+ contours for Case 1: a) whole domain, b) leading-edge..... **53**
Figure 5.14 : y+ contours for Case 2: a) whole domain, b) leading-edge..... **54**
Figure 5.15 : Leading-edge data sampling locations and excluded regions. **55**
Figure 5.16 : Case 1 CFD vs. experiment [8] local Nusselt number distribution. **55**

Figure 5.17 : Case 2 CFD vs. experiment [8] local Nusselt number distribution. **56**
Figure 5.18 : Non-dimensional velocity contours from Forster and Weigand [8]: a) Center plane (Y=0), b) $X/D_{jet}=1$ **57**
Figure 5.19 : Non-dimensional velocity contours of the present study: a) Center plane (Y=0), b) X/Djet=1 .... **57**
Figure 6.1 : Change of the domain for different H/D values: a) H/D=1.4, b) H/D=2.7, c) H/D=4.0, d) H/D=5.3. .... **60**
Figure 6.2 : Change of the domain for different P/D values: a) P/D=2, b) P/D=4, c) P/D=6, d) P/D=8. .... **60**
Figure 6.3 : Comparison of CFD data vs derived correlation. **64**
Figure 6.4 : Effect of the jet Reynolds number Re_D on the surface-averaged Nusselt number for fixed P/D = 4 and varying H/D. **66**
Figure 6.5 : Nu for H/D=2.7, P/D=4: a) $Re_D=10^3$, b) $Re_D=2x10^3$, c) $Re_D=3x10^3$, d) $Re_D=4x10^3$. **67**
Figure 6.6 : Effect of the jet-to-surface spacing ratio H/D on the surface-averaged Nusselt number for fixed P/D = 4 and varying Re_D. **68**
Figure 6.7 : Nu for $Re_D=3x10^3$, P/D=4: a) H/D=1.4, b) H/D=2.7, c) H/D=4.0, d) H/D=5.3. .... **68**
Figure 6.8 : Effect of the jet-to-jet pitch ratio P/D on the surface-averaged Nusselt number for fixed H/D = 2.7 and varying Re_D. **69**
Figure 6.9 : Nu for $Re_D=3x10^3$, H/D=2.7: a) P/D=2, b) P/D=4, c) P/D=6, d) P/D=8. .... **70**

NUMERICAL INVESTIGATION OF HEAT TRANSFER IN GENERIC GAS TURBINE BLADE WITH IMPINGEMENT COOLING UNDER HIGH CROSSFLOW EFFECT

SUMMARY

Gas turbines have been among the most transformative thermal machines since the mid-20th century, playing a central role in aviation, power generation, and industrial energy systems. Following the rapid technological progress after World War II, gas turbines became indispensable due to their high power-to-weight ratio, continuous-flow operation, operational reliability, and compact structural design. Over time, advancements in aerodynamic design, materials science, and combustion technology have enabled these systems to operate at increasingly demanding conditions. Today, gas turbines are widely utilized in Aerospace Engineering and energy production sectors, where continuous improvements in efficiency and performance remain primary objectives.

A key parameter governing gas turbine performance is the turbine inlet temperature. Increasing this temperature directly enhances thermodynamic cycle efficiency and specific power output. However, this improvement comes at the expense of significantly elevated thermal loads on turbine components, particularly rotor blades and stator vanes. These components are subjected to extreme temperature gradients, high thermal stresses, and aggressive environmental conditions, which may lead to degradation mechanisms such as thermal fatigue, oxidation, corrosion, and creep. Consequently, the development of advanced cooling strategies, along with high-temperature-resistant materials and thermal barrier coatings, has become essential for ensuring component durability and operational safety.

In addition to thermal considerations, modern gas turbine systems must also meet stringent requirements related to aerodynamic efficiency, fuel consumption, and emission reduction. These multi-objective design constraints necessitate a highly integrated approach, where thermal management, structural integrity, and aerodynamic performance are simultaneously optimized. As gas turbine technology continues to evolve toward higher operating temperatures and more compact configurations, the importance of efficient and reliable cooling techniques becomes increasingly pronounced.

Among various internal cooling techniques, jet impingement cooling has gained significant attention due to its ability to produce very high local heat transfer coefficients, particularly in stagnation regions where the cooling jet directly impacts the surface. This characteristic makes it especially suitable for critical regions such as the leading edge of turbine blades, where heat fluxes are highest and geometric constraints limit the use of alternative cooling approaches. The effectiveness of impingement cooling is primarily attributed to strong jet momentum, intense turbulence generation, and thin thermal boundary layers formed at the impingement zone.

Nevertheless, in realistic gas turbine environments, impinging jets are rarely isolated. Instead, they interact with a crossflow that develops within the cooling passage as the coolant progresses downstream. This crossflow introduces significant complexity into the flow field by deflecting the jet trajectory, weakening the stagnation region, and altering the overall heat transfer distribution. Furthermore, the interaction between the jet and crossflow leads to the formation of shear layers, vortical structures, and enhanced turbulence in the wall-jet region. These effects collectively result in a substantial deviation from classical impingement behavior, making the prediction of heat transfer characteristics considerably more challenging. Therefore, a detailed understanding of jet–crossflow interaction mechanisms is essential for the accurate design and optimization of turbine blade cooling systems.

The present study provides a comprehensive numerical investigation of internal heat transfer characteristics in a generic gas turbine blade passage cooled by jet impingement under high crossflow conditions. A three-dimensional computational fluid dynamics (CFD) model was developed using a Reynolds-Averaged Navier–Stokes (RANS) framework, incorporating a suitable turbulence model capable of resolving complex flow features such as jet deflection, flow separation, reattachment, and turbulence generation. Particular attention was given to accurately capturing near-wall flow behavior and its influence on convective heat transfer.

To ensure the reliability of the numerical approach, the model was validated against experimental data available in the literature. Comparisons of local Nusselt number distributions and area-averaged values demonstrated strong agreement, confirming that the simulation framework is capable of accurately representing both the flow physics and thermal characteristics of the system.

A detailed parametric study was conducted to evaluate the influence of key governing parameters, including jet Reynolds number (Re_D), jet-to-surface distance (H/D), and jet-to-jet spacing (P/D). Simulations were performed under a high crossflow intensity of approximately 60%, representative of realistic operating conditions in gas turbine cooling passages. The investigated parameter ranges include Re_D = 10,000–40,000, H/D = 1.4–5.3, and P/D = 2–8. This wide parameter space allows for a systematic assessment of both momentum-driven and geometric effects on heat transfer performance.

Using the numerical dataset, an empirical correlation was developed to predict the Nusselt number as a function of Re_D, H/D, and P/D. The proposed correlation exhibits high predictive accuracy, with a Mean Absolute Percentage Error (MAPE) of 3.72%, indicating excellent agreement with the simulation results. The power-law form of the correlation highlights the dominant role of jet Reynolds number, while also capturing the secondary influence of geometric parameters.

The results clearly demonstrate that the jet Reynolds number is the primary parameter controlling heat transfer enhancement. Increasing Re_D leads to stronger jet penetration, higher turbulence intensity, and more effective disruption of the thermal boundary layer, thereby significantly increasing the Nusselt number. Conversely, increasing the jet-to-surface distance (H/D) reduces the jet's momentum before reaching the surface, weakening the stagnation region and decreasing heat transfer performance. Similarly, increasing the jet spacing (P/D) reduces jet interaction and results in a less uniform and generally lower heat transfer distribution. Although both H/D and P/D have notable effects, their influence remains secondary compared to that of Re_D.

In conclusion, this study provides a detailed numerical framework and a robust empirical correlation for analyzing jet impingement cooling under high crossflow conditions. The findings offer valuable insights into the complex interaction mechanisms governing heat transfer in turbine blade cooling passages. The proposed correlation serves as a practical engineering tool for rapid performance estimation during preliminary design stages, while the numerical methodology establishes a strong foundation for further advanced investigations. Overall, this work contributes to the development of more efficient and reliable cooling strategies for next-generation gas turbine systems.

YÜKSEK ÇAPRAZ AKIŞ ETKİSİ ALTINDA ÇARPMA JET SOĞUTMALI JENERİK BİR GAZ TÜRBİNİ KANADINDA ISI TRANSFERİNİN SAYISAL İNCELENMESİ

ÖZET

Gaz türbinleri, 20. yüzyılın ortalarından itibaren havacılık, enerji üretimi ve endüstriyel güç sistemlerinde devrim yaratan en önemli ısıl makineler arasında yer almaktadır. Özellikle II. Dünya Savaşı sonrasında jet motoru teknolojisinin hızla gelişmesiyle birlikte gaz türbinleri; yüksek güç/ağırlık oranı, sürekli akış prensibi ve kompakt yapıları sayesinde modern mühendislik uygulamalarının vazgeçilmez bileşenlerinden biri haline gelmiştir. Günümüzde Havacılık ve Uzay Mühendisliği başta olmak üzere enerji üretim sistemlerinde yaygın olarak kullanılan gaz türbinleri, artan performans beklentileri doğrultusunda sürekli olarak daha yüksek türbin giriş sıcaklıklarında çalışacak şekilde tasarlanmaktadır.

Türbin giriş sıcaklığının artırılması, çevrim veriminin yükseltilmesi açısından kritik bir parametre olmakla birlikte, bu durum türbin kanatlarının çok yüksek ısıl yüklere maruz kalmasına neden olmaktadır. Bu nedenle, ileri seviye malzeme teknolojileri, kaplama yöntemleri ve özellikle etkin soğutma teknikleri, gaz türbini tasarımının ayrılmaz bir parçası haline gelmiştir. Yüksek sıcaklık gradyanları, termal yorulma, oksidasyon ve sürünme (creep) gibi hasar mekanizmaları, kanat ömrünü doğrudan sınırlayan temel faktörlerdir. Bu bağlamda, türbin kanatlarının güvenli ve uzun ömürlü çalışabilmesi için iç ve dış soğutma yöntemlerinin optimize edilmesi kritik öneme sahiptir.

Ayrıca, modern gaz türbinlerinde artan performans gereksinimleri yalnızca termal dayanım ile sınırlı kalmayıp, aynı zamanda aerodinamik verim, yakıt tüketimi ve emisyon değerleri gibi parametreleri de doğrudan etkilemektedir. Bu nedenle, yüksek sıcaklık koşullarında çalışan türbin bileşenlerinin hem yapısal hem de termal açıdan dengeli bir şekilde tasarlanması gerekmektedir. Sonuç olarak, gaz türbinlerinin tarihsel gelişimi, günümüzde ulaşılan yüksek performans seviyeleri ve gelecekteki tasarım hedefleri göz önüne alındığında, etkin ve güvenilir soğutma teknolojilerinin geliştirilmesi kaçınılmaz bir mühendislik gereksinimi olarak ortaya çıkmaktadır.

Modern gaz türbini kanatlarının maruz kaldığı son derece yüksek sıcaklık ve ısıl yükler, bu bileşenlerin güvenilir çalışması, yapısal bütünlüğü ve servis ömrü açısından gelişmiş ve etkin iç soğutma stratejilerinin uygulanmasını zorunlu kılmaktadır. Bu bağlamda, çarpma jet soğutması (impingement cooling), akışın yüzeye dik olarak çarpması sonucu stagnasyon bölgesinde oldukça yüksek yerel ısı transfer katsayıları oluşturabilmesi nedeniyle en etkili iç soğutma tekniklerinden biri olarak öne çıkmaktadır. Özellikle türbin kanatlarının leading-edge (hücum kenarı) bölgelerinde, yüksek ısı akısı ve sınırlı soğutma alanı nedeniyle bu yöntem yaygın olarak tercih edilmektedir. Bununla birlikte, gerçek gaz türbini çalışma koşullarında, çarpma jetleri izole bir ortamda davranmaz; aksine, kanal boyunca gelişen ve giderek güçlenen bir çapraz akış (crossflow) ile etkileşime girer. Bu çapraz akış, jet çekirdeğini eğerek

stagnasyon bölgesinin konumunu ve şiddetini değiştirir, jet penetrasyonunu sınırlar ve duvar jeti (wall-jet) bölgesinde kesme tabakası kaynaklı karmaşık türbülans yapılarının oluşmasına neden olur. Sonuç olarak, ısı transferi dağılımı önemli ölçüde yeniden şekillenir ve klasik çarpma jet davranışından belirgin şekilde sapmalar gözlemlenir. Bu nedenle, jet–çapraz akış etkileşiminin fiziksel mekanizmalarının doğru şekilde anlaşılması ve modellenmesi, yüksek performanslı türbin kanadı soğutma tasarımlarının geliştirilmesi açısından kritik bir gerekliliktir.

Bu çalışma, belirli bir yüksek çapraz akış koşulu altında çarpma jetleri ile soğutulan jenerik bir gaz türbini kanadı geçidindeki iç ısı transferi karakteristiklerinin kapsamlı ve sistematik bir sayısal incelemesini sunmaktadır. Çalışmada, jet–çapraz akış etkileşimi, akış ayrılması (flow separation), yeniden yapışma bölgeleri (reattachment), türbülans üretimi ve duvar yakınındaki akış yapılarının ısı transferine olan etkilerini doğru şekilde yakalayabilmek amacıyla, uygun Reynolds ortalamalı Navier–Stokes (RANS) türbülans modeli kullanılarak üç boyutlu bir hesaplamalı akışkanlar dinamiği (HAD/CFD) modeli geliştirilmiştir. Özellikle yüksek çapraz akış şiddeti altında ortaya çıkan jet eğilmesi, birleşme ve etkileşim mekanizmaları detaylı olarak ele alınmıştır. Geliştirilen sayısal metodoloji, literatürde yer alan ilgili bir deneysel çalışma ile karşılaştırılarak doğrulanmış; hem yerel Nusselt sayısı dağılımları hem de alan ortalamalı değerler açısından iyi bir uyum elde edilmiştir. Bu doğrulama süreci, modelin hem akış yapısını hem de ısı transferi karakteristiklerini güvenilir bir şekilde temsil edebildiğini göstermektedir.

Çalışma kapsamında gerçekleştirilen parametrik analizlerde, geometrik ve akış parametrelerinin geniş bir aralıkta etkileri incelenmiştir. Özellikle jetler arası adım (P/D), jet–yüzey mesafesi (H/D) ve jet Reynolds sayısı (Re_D) temel kontrol parametreleri olarak seçilmiştir. Farklı çarpma deliği düzenleri altında gerçekleştirilen simülasyonlar, yaklaşık %60 seviyesinde yüksek çapraz akış şiddeti koşulunda yürütülmüş olup, bu durum gerçek motor içi çalışma şartlarını temsil etmektedir. İncelenen parametre aralığı, Re_D = 10000–40000, H/D = 1.4–5.3 ve P/D = 2–8 değerlerini kapsamaktadır. Bu geniş parametre uzayı, hem düşük hem de yüksek jet momentum koşullarında jet–yüzey etkileşiminin değişimini analiz etmeye olanak sağlamaktadır. Elde edilen sonuçlar, hem yerel hem de alan ortalamalı Nusselt sayısı (Nu) dağılımları üzerinden değerlendirilmiş ve farklı parametrelerin ısı transferi performansı üzerindeki etkileri sistematik olarak karşılaştırılmıştır.

Sayısal sonuçlar kullanılarak, Nusselt sayısını Re_D, H/D ve P/D parametrelerinin bir fonksiyonu olarak ifade eden ampirik bir korelasyon geliştirilmiştir. Bu korelasyon, hem mühendislik uygulamalarında hızlı tahmin imkânı sunmakta hem de temel akış fiziğini yansıtacak şekilde yapılandırılmıştır. Önerilen model, %3.72 ortalama mutlak yüzde hata (MAPE) ile sayısal verileri yüksek doğrulukla tahmin etmekte olup, incelenen parametre aralığında güvenilir bir tasarım aracı olarak kullanılabilir. Korelasyonun üstel yapısı, jet momentumunun baskın rolünü ve geometrik parametrelerin ikincil etkilerini açık bir şekilde ortaya koymaktadır.

Elde edilen bulgular, jet Reynolds sayısının ısı transferi artışını belirleyen en önemli parametre olduğunu göstermektedir. Re_D'nin artması, jetin yüzeye ulaşma enerjisini artırarak stagnasyon bölgesinde daha yüksek konvektif ısı transfer katsayılarının oluşmasına neden olmaktadır. Ayrıca, artan türbülans yoğunluğu ve jet–yüzey etkileşimi, duvar jeti bölgesinde de ısı transferinin güçlenmesini sağlamaktadır. Buna karşılık, jet–yüzey mesafesinin (H/D) artması, jetin yüzeye ulaşmadan önce çevre akış ile karışarak momentum kaybetmesine ve dolayısıyla stagnasyon etkisinin

zayıflamasına neden olmaktadır. Benzer şekilde, jetler arası adımın (P/D) artması, jetler arasındaki etkileşimi azaltarak yüzey üzerindeki ısı transfer dağılımının daha heterojen ve düşük seviyelerde gerçekleşmesine yol açmaktadır. Ancak bu iki geometrik parametrenin etkileri, büyüklük olarak birbirine yakın olup ikincil derecede rol oynamaktadır.

Sonuç olarak, bu çalışmada geliştirilen sayısal yaklaşım ve elde edilen ampirik korelasyon, yüksek çapraz akış koşulları altında çalışan çarpma jet soğutma sistemlerinin performansının anlaşılması, modellenmesi ve optimize edilmesi açısından önemli katkılar sunmaktadır. Önerilen model, ön tasarım aşamalarında hızlı ve güvenilir tahminler yapılmasına olanak sağlarken, aynı zamanda daha detaylı sayısal veya deneysel çalışmalar için de sağlam bir temel oluşturmaktadır. Bu yönüyle çalışma, gaz türbini kanatlarının termal yönetimine yönelik mühendislik uygulamalarında doğrudan kullanılabilecek pratik ve fiziksel olarak tutarlı bir yaklaşım ortaya koymaktadır.

1. INTRODUCTION

Gas turbines occupy a central role in the era of modern energy and aerospace industries because of their compactness, high power density, and ability to convert a broad range of liquid and gaseous fuels into mechanical work at high thermodynamic efficiency. Today's energy market spans gas turbines from approximately 1 MW to more than 500 MW per unit, used in stationary power generation, aircraft propulsion, mechanical drive on natural-gas pipelines, and marine propulsion [1]. As Naik [1] emphasizes, the constant pressure to reduce fuel consumption and CO_2 emissions has driven sustained progress in turbine aerothermal design, blade-cooling schemes, high-temperature alloys, metallic anti-oxidation coatings, and thermal-barrier coatings. Korpela [2] further notes that gas turbines burning natural gas have made significant inroads into electricity generation since the 1980s, both as stand-alone units and, especially, as the topping cycle in heat-recovery combined-cycle plants whose overall plant thermal efficiency now approaches the 60–65 % range—substantially higher than that of either machine operating alone.

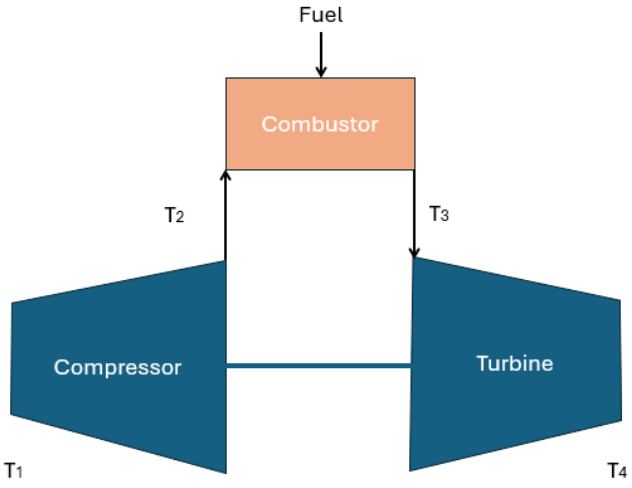

Figure 1.1 : Schematic of a simple-cycle gas turbine.

From a thermodynamic perspective, the simple gas-turbine engine may be represented by a compressor, a combustion chamber, an expansion turbine, and an exhaust section operating in sequence under the idealized Brayton-cycle framework. The working

cycle, idealized as the Brayton cycle, comprises compression of ambient air, constant-pressure heat addition by fuel combustion, expansion of the hot gases through the turbine, and heat rejection at the exhaust [1,3]. A simplified arrangement of these components is shown in Figure 1.1, while the corresponding ideal Brayton cycle on a temperature–entropy plane is illustrated in Figure 1.2. Both the cycle thermal efficiency and the specific work output increase with the turbine inlet temperature (TIT) and with the overall compressor pressure ratio, so that raising the TIT has historically been the principal lever for improving engine performance, and modern engines are characterized by progressively higher firing temperatures and pressure ratios than their predecessors [1,2,4].

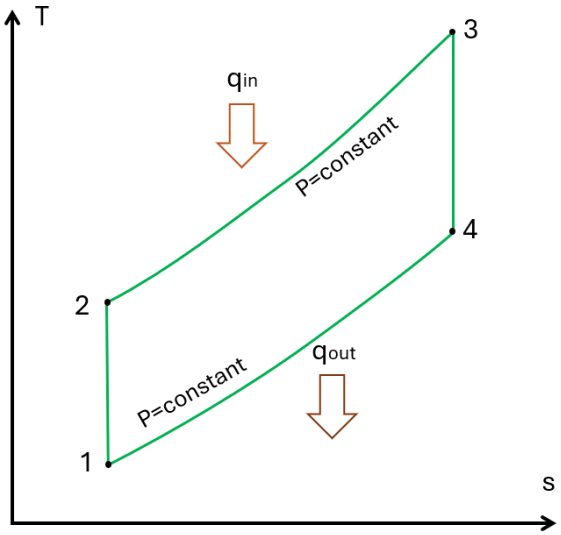

Figure 1.2 : Ideal Brayton cycle on a temperature–entropy diagram.

However, this drive toward ever higher firing temperatures introduces a fundamental thermo-mechanical challenge. Han, Dutta, and Ekkad [3] document that the working-fluid temperatures of advanced engines, today routinely above 1700 K in the first stages, lie hundreds of Kelvins above the permissible metal temperatures of even the most advanced single-crystal nickel-based superalloys protected by ceramic thermal-barrier coatings. Without active cooling, the hot-gas-path components would not survive long enough to perform any useful work. Bunker [5] adds that, despite four decades of intensive research and several generations of advanced cooling concepts, the design of cooled hot-gas-path components remains constrained by a number of unresolved engineering challenges, including durability under increasingly aggressive thermal cycles, the prediction of three-dimensional conjugate heat-transfer fields, and the integration of cooling, aerodynamic, and stress design into a single manufacturable

component. Figure 1.3 illustrates the long-standing gap between the rising TIT and the slower progression of metal capability—a gap that, in modern engines, is bridged by a layered combination of internal cooling, film cooling, and thermal-barrier coatings.

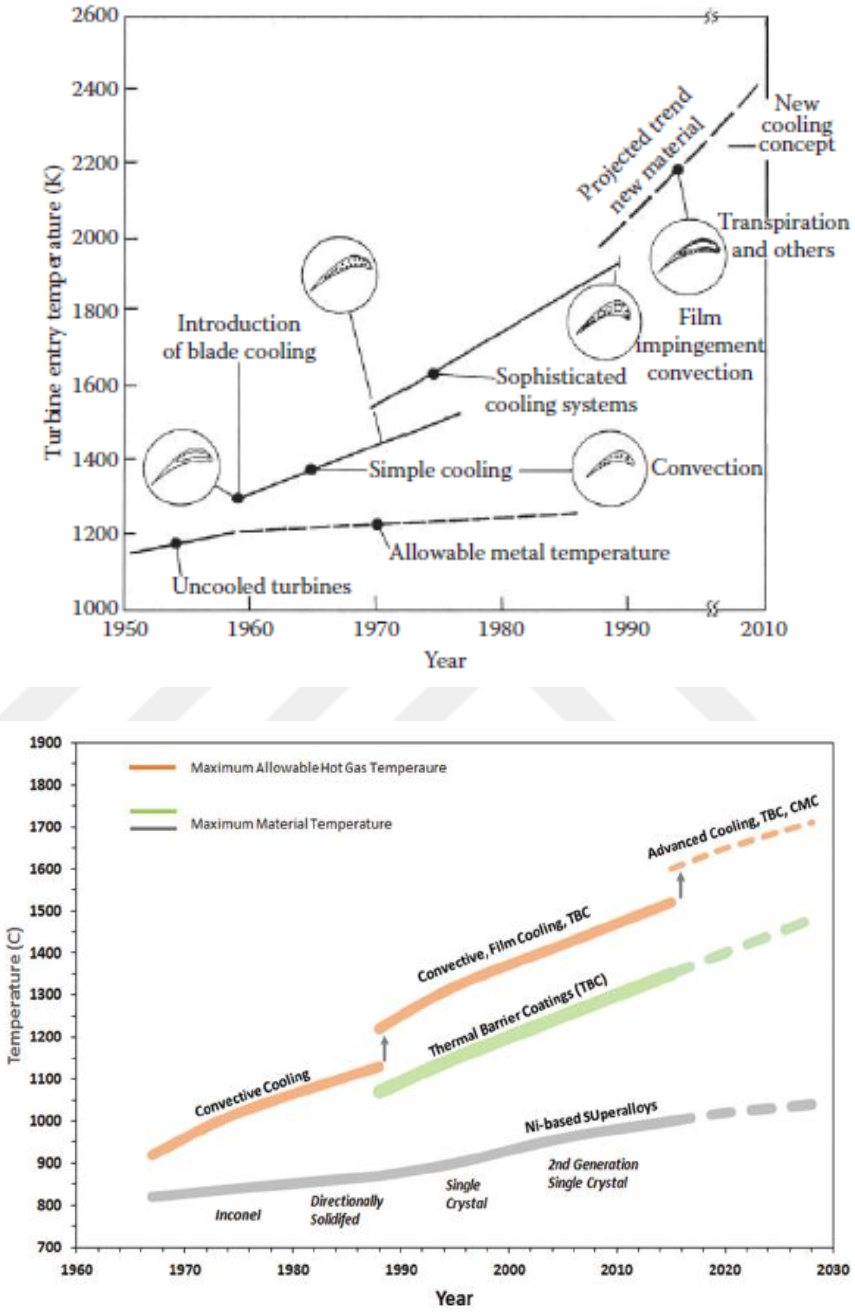

Figure 1.3 : Evolution of turbine inlet temperature, blade material capability, and cooling-technology generations [1,3].

The thermal environment surrounding a cooled airfoil is extremely demanding. As reported by Zuckerman and Lior [6], cooling air drawn from the compressor is expected to protect blades exposed to gas streams whose total temperatures reach approximately 1800 K — a condition that translates into wall heat fluxes on the order

of 1 MW/m² and demands internal convective coefficients between roughly 1000 and 3000 W/m²K. Han and Dutta [7] further note that recent developments in turbine internal cooling have been driven by the simultaneous demand for higher heat-transfer rates and longer life, and that the current designs use a tightly integrated combination of impingement, ribbed serpentine passages, pin-fin banks, and film cooling. Naik [1] adds that the front-stage airfoils, exposed to the highest hot-gas temperatures, demand the most aggressive cooling and routinely combine all of these techniques together with a thermal-barrier coating, while the rear-stage airfoils—which see significantly cooler gas—may rely on simple convective schemes alone.

The cooling air is normally extracted from the high-pressure compressor and supplied to the airfoil at a temperature of around 900 K, several hundred Kelvin colder than the surrounding hot gas [6]. The bleed air is routed through internal cooling cavities of the blade and is also discharged through film-cooling holes on the external surface, where it forms a protective film that shields the metal from the hot stream [3]. Although extracting air from the compressor incurs a thermodynamic penalty—the extracted air no longer participates in the expansion process and therefore reduces the turbine work output—this penalty is small compared with the benefit of permitting a substantially higher TIT [6]. The selection and arrangement of the cooling techniques on a particular airfoil depend strongly on the local heat load, the geometric constraints imposed by the airfoil profile, and the available coolant pressure relative to the local hot-gas pressure [1].

Among all internal cooling methods, jet impingement is one of the most thermally effective. If it is compared with conventional convective cooling, in which the coolant flows parallel to a heated surface, it can be said that impingement results with local heat-transfer coefficients that can be reached almost higher than three times at a given coolant mass flow rate, owing to the very thin boundary layers formed at the stagnation region and to the high turbulence intensity of the spent flow [3,6]. In a typical implementation, an internal insert with a perforated wall directs cooling-air jets onto the inner surface of the blade. After impinging, the spent air either exits through film-cooling holes—thereby providing additional external film cooling—or is convected toward the trailing edge, where it is finally ejected into the main hot-gas stream [3,6]. Impingement is preferentially used at the leading edge, where the external heat load is the highest and the geometry is most strongly curved [8]; in the midchord region of

the airfoil, two-dimensional arrays of jets are used to cool the pressure and suction sides, and the spent air is then constrained to exit toward the trailing edge through the channel formed between the impingement insert and the inner blade wall [9].

A practical complication that arises in such midchord and leading-edge arrays is the crossflow effect. The spent air of the upstream jets cannot simply disappear and instead accumulates inside the cooling cavity, forming a transverse stream, the crossflow,that interacts with the downstream jets [9]. The presence of crossflow deflects the jets away its the normal direction, causes a decrease at the stagnation-point heat transfer, and creates changes in the local distribution of the Nusselt number on the given target surface [8]. In midchord cooling configurations the crossflow becomes increasingly strong toward the rear of the airfoil, since the spent air of every upstream row must be evacuated through the same confined channel; in some designs the crossflow at the array entrance is further amplified by an upstream extension of the channel that carries the spent leading-edge coolant into the midchord region. Understanding and predicting the heat-transfer behaviour of impingement arrays under such crossflow is therefore essential for the design of advanced turbine cooling systems.

The present thesis addresses this issue through a three-dimensional numerical investigation of jet impingement cooling on a generic gas-turbine-blade configuration, performed within the Reynolds-Averaged Navier–Stokes (RANS) framework. The study focuses on a high-crossflow regime, with crossflow intensity of approximately 60 %, and considers a wide parametric space encompassing jet Reynolds numbers between 10 000 and 40 000, jet-to-target spacing ratios H/D between 1.4 and 5.3, and jet-to-jet pitch ratios P/D between 2 and 8. The objectives are twofold: first, to characterize the local and global heat-transfer behaviour over this parameter range; and second, to derive a compact engineering correlation for the area-averaged Nusselt number as a function of the principal geometric and flow parameters under high-crossflow operation. The remainder of this thesis introduces the principal cooling techniques used in modern gas-turbine engines (Chapter 2), reviews the literature most relevant to the present problem and identifies the knowledge gap that the work fills (Chapter 3), develops the underlying CFD theory (Chapter 4), and presents the validation case (Chapter 5), shows the numerical methodology and the parametric results (Chapter 6), and finally summarizes the principal conclusions and recommendations for future work (Chapter 7).

2. TYPES OF COOLING IN GAS TURBINE ENGINES

The thermal protection of modern gas-turbine airfoils is achieved by a layered combination of cooling technologies, each addressing a specific region of the blade and a specific aspect of the heat-transfer problem. Han, Dutta, and Ekkad [3] divide blade cooling into two broad categories: internal cooling, in which coolant is routed through enhanced internal passages and extracts heat from the hot external surfaces by conduction through the metal wall; and external cooling, more commonly known as film cooling, in which the spent internal coolant is ejected through discrete holes or slots to form a protective film on the outside of the blade. Both jet impingement and pin-fin cooling are also classified as internal techniques. Naik [1] further subdivides the internal heat-transfer technologies into impingement cooling, ribbed (turbulated) channels, pin or pedestal banks, dimples, shaped internal passages, and combinations of these. As Bunker [5] emphasizes in his survey of remaining hot-gas-path challenges, the integration of these elements into a single manufacturable, durable, and aerodynamically efficient component is itself one of the principal open problems in modern turbine design.

The selection and arrangement of these cooling techniques depend strongly on the local heat load, on the geometric constraints imposed by the airfoil profile, and on the available coolant pressure ratio relative to the local hot-gas pressure [1]. As a general rule, the front stages of the turbine receive coolant extracted at the highest pressures from the compressor discharge, while the middle and rear stages receive coolant from progressively lower-pressure inter-stage bleeds [1]. The front-stage airfoils therefore use the most aggressive combinations—typically film cooling combined with internal impingement and turbulator-augmented serpentine passages—while rear-stage airfoils may rely on pure convective cooling alone [1,3]. Figure 2.1 illustrates the typical distribution of the principal cooling schemes across the cross-section of a high-pressure turbine blade, while Figure 2.2 shows a more detailed schematic of a fully cooled blade integrating leading-edge impingement, multi-pass serpentine convective

cooling with ribs, trailing-edge pin-fin cooling, and showerhead and gill film cooling. The remainder of this chapter describes each of these cooling techniques in turn.

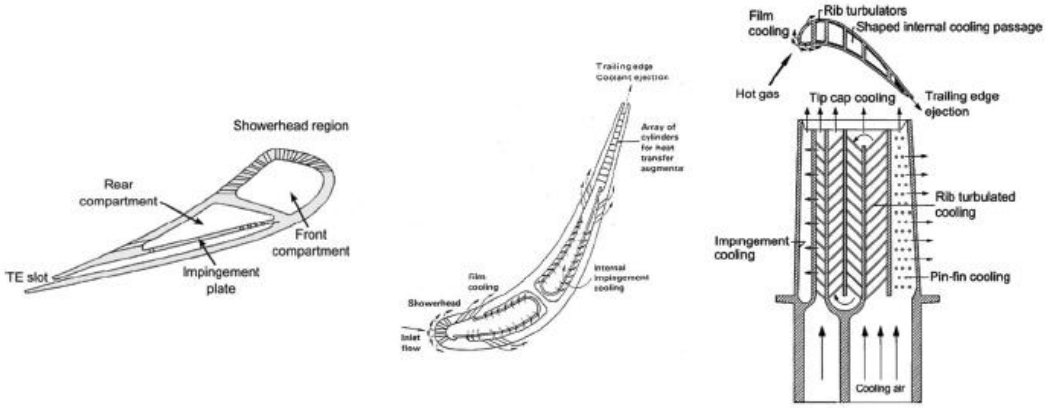

Figure 2.1 : Typical cooling techniques applied to a high-pressure turbine blade and vane [1].

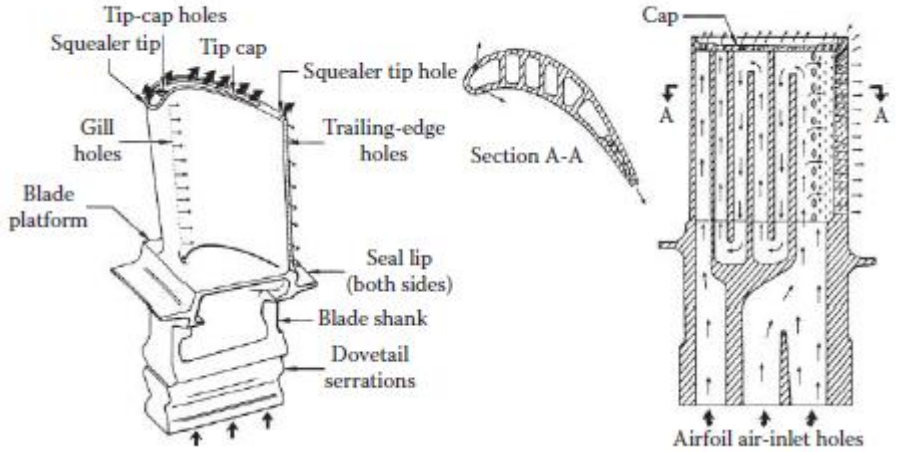

Figure 2.2 : Schematic of a modern cooled HP turbine blade combining leading-edge impingement, multi-pass serpentine convective cooling with ribs, pin-fin cooling, and film cooling [3].

2.1 Convective Cooling

Convective cooling is the simplest and most fundamental form of internal cooling. Cool compressor bleed air is routed through one or more internal passages within the airfoil, and the heat conducted from the external hot surfaces through the metal wall is removed by forced convection of the coolant flowing inside [3,7]. The heat removed depends on the local heat-transfer coefficient between the coolant and the inner wall, on the wetted area, and on the local temperature difference between the wall and the bulk coolant.

In rotating blades, the internal passages are typically arranged as multi-pass serpentine systems oriented radially [1,3]. Coolant is supplied at the blade root, flows radially outward through the first pass to the blade tip, turns through 180°, flows radially inward through the second pass, and so on. This configuration both maximises the residence time of the coolant in contact with the heated wall and accommodates the strong radial pressure gradients caused by rotation. In rotating channels, however, Coriolis and centrifugal-buoyancy forces generate secondary flows that significantly alter the local heat-transfer distribution between the leading and trailing surfaces of the channel relative to a stationary case [3,7]. The leading and trailing sides of a radially outward pass therefore exhibit different heat-transfer levels, and proper accounting of these effects is essential in modern blade design.

Although convective cooling alone may be sufficient for the relatively cool rear stages of a turbine, where the hot-gas temperature is close to or below the material capability, the front stages—which are exposed to gas temperatures hundreds of degrees above the metal limit—require its combination with more aggressive techniques such as ribs, pin fins, impingement, and film cooling [1,3].

2.2 Rib-Turbulated (Augmented Convective) Cooling

To increase the heat-transfer coefficient available in the radial cooling passages without prohibitively increasing the coolant flow rate, repeated rib-shaped turbulence promoters—commonly called turbulators or ribs—are cast on two opposite walls of the internal channels of advanced gas-turbine blades [3,10]. The ribs trip the boundary layer and produce regions of flow separation immediately downstream of each rib, followed by reattachment of the separated shear layer onto the heated wall some distance further downstream. As reviewed by Han [10], this separation–reattachment cycle generates intense local turbulence that thins the thermal boundary layer and substantially raises the heat-transfer coefficient. Figure 2.3 schematically illustrates the flow pattern, including the recirculation zones immediately behind each rib and the periodic reattachment points that drive the augmentation. Because the ribs primarily disturb only the near-wall flow, the associated pressure-drop penalty remains acceptable for blade-cooling designs [10].

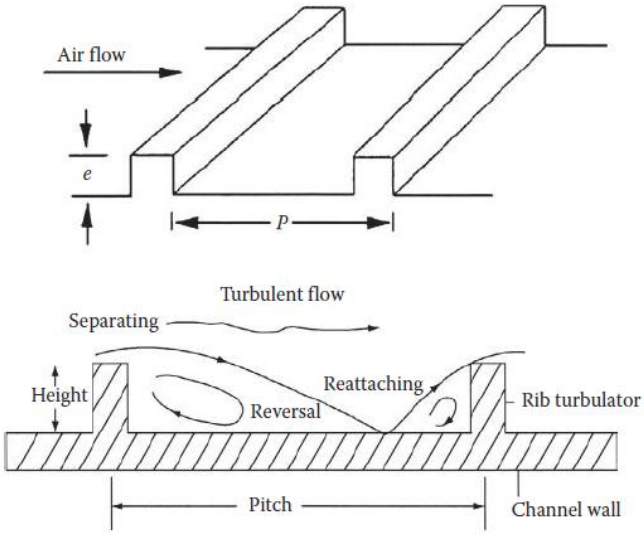

Figure 2.3 : Flow pattern in a rib-turbulated cooling channel showing recirculation zones and reattachment points [10].

The performance of a ribbed channel depends on several geometric and flow parameters: the rib angle of attack α, the rib pitch-to-height ratio P/e, the rib height-to-hydraulic-diameter ratio e/D_h (typically 5–10 %), the rib shape, the channel aspect ratio W/H, the flow Reynolds number, and the rotation number [3,10]. Han [10] reports that ribs oriented at 45° or 60° to the main flow generate cross-stream secondary flows that further enhance turbulent mixing and yield approximately three-fold heat-transfer enhancement over a smooth channel, although at a friction penalty four to eight times that of the smooth case. Transverse ribs at 90° enhance heat transfer with a slightly smaller penalty but provide less benefit overall in narrow channels.

In rotating channels the picture is further complicated by Coriolis and centrifugal-buoyancy forces. For radially outward flow, the Coriolis force pushes the coolant toward the trailing side of the channel, thinning the boundary layer there and enhancing heat transfer while reducing it on the leading side; for radially inward flow the effect is reversed [3,7,10]. The channel orientation relative to the axis of rotation—which depends on whether the channel is in the leading-edge or mid-chord region of the blade—alters this Coriolis-driven asymmetry. Modern blade designs therefore optimise the rib geometry on a passage-by-passage basis, and variants such as broken ribs, V-shaped ribs, and chevron ribs are routinely used to control the secondary-flow structure and to balance heat-transfer augmentation against the friction penalty [1,3, 10].

2.3 Pin-Fin Cooling

The narrow trailing-edge region of a turbine blade imposes severe geometric constraints: the airfoil thickness here is too small to accommodate impingement inserts or large rib-roughened serpentine passages, yet this region is also subject to high heat fluxes and to a highly non-uniform external flow [1]. Pin-fin cooling is the preferred internal cooling solution in this region. Pin fins are short cylindrical (or, in advanced designs, conical or shaped) elements that bridge the pressure and suction sides of the airfoil, typically arranged in staggered patterns with three to ten rows in the streamwise direction [1,3].

Pin fins enhance heat transfer through three simultaneous mechanisms: the increased wetted area provided by the pins themselves, the high heat-transfer coefficients on both the pin surfaces and the endwalls in the vicinity of the pin–endwall junction, and the intense wake-induced turbulence that develops behind each row of pins and persists into subsequent rows [1,3]. The local heat-transfer coefficient typically rises from the first row of pins to a peak in the second or third row, after which it gradually decays as the wake structure becomes well mixed. An important secondary advantage is that pin banks provide direct mechanical bridging between the pressure and suction sides of the airfoil, improving the structural rigidity of the thin trailing edge and the castability of the blade core [1]. The penalty is a relatively high pressure drop, but this is generally acceptable in the trailing-edge region because the available coolant pressure is high relative to the local hot-gas pressure. Recent investigations have explored conical pins and hybrid pin–turbulator configurations, all aiming at higher heat-transfer enhancement at acceptable pressure-drop penalties [1].

2.4 Film Cooling

Film cooling is the principal external cooling technique and is applied along the perimeter of an airfoil through rows of discrete holes drilled at compound angles to the surface [1,3]. The internal coolant—several hundred degrees colder than the surrounding hot gas—is ejected into the external boundary layer and forms a protective film along the airfoil surface that reduces the effective driving temperature for the heat transfer between the gas and the wall [1]. The protective film is gradually eroded by

turbulent mixing with the hot gas, so additional rows of holes are typically distributed along the blade chord wherever the local heat load justifies their presence.

The performance of film cooling is characterized by the film-cooling effectiveness η, defined as a normalized temperature difference between the gas, the wall, and the coolant. The effectiveness depends on a wide set of geometric and flow parameters: the hole shape (cylindrical, fan-shaped, or three-dimensionally contoured), the inclination angle and compound angle of the hole, the blowing ratio (the mass-flux ratio of coolant to mainstream), the density ratio, the freestream turbulence level, and the surface curvature [1,3]. As Naik [1] notes, increasing the average film-cooling effectiveness on a turbine blade reduces the temperature ratio between the film and the hot gas and can lower the near-wall film temperature by several hundred Kelvins relative to the surrounding hot-gas temperature.

Although increasing the number of film-cooling rows improves the average effectiveness, it also raises the coolant consumption and therefore reduces turbine efficiency. For this reason, much of the modern film-cooling research has focused on alternative ways of improving effectiveness without increasing the coolant flow: in particular, fan-shaped (diffusing) holes, three-dimensionally contoured holes, and trench geometries that promote lateral spreading of the film [1]. Film cooling is most heavily applied on the front-stage airfoils and is typically combined with internal impingement and rib-turbulated cooling, providing a layered defence against the hot gas [1,3].

2.5 Impingement Cooling

Impingement cooling is the most thermally effective internal cooling method available for gas-turbine airfoils, and it constitutes the central topic of this thesis. Cooling air emerges as a series of high-velocity jets from a perforated insert or impingement plate located inside the airfoil cavity, and these jets strike the inner surface of the blade wall [3,6]. As the jets approach the wall, the boundary layer thins drastically in the stagnation region, leading to local heat-transfer coefficients that can exceed those achievable by conventional convective or rib-turbulated cooling by a factor of two to three at the same coolant mass flow rate [6,11]. As a consequence, for a required heat-transfer coefficient the coolant flow rate of an impingement device may be up to two orders of magnitude smaller than that of a wall-parallel convection arrangement [6].

The flow field developing under a single round impinging jet on a flat surface is illustrated in Figure 2.4. As classified by Martin [11], Viskanta [12], and Zuckerman and Lior [6], it is conventionally divided into three regions. In the free-jet region, the jet emerges from the nozzle and accelerates downward; a potential core surrounds the jet centreline near the nozzle exit, surrounded by a thickening shear layer that grows as the jet entrains ambient fluid. In the stagnation (impingement) region, immediately above and around the impingement point, the flow decelerates rapidly and turns radially outward; the boundary layer here is exceptionally thin, which is the underlying reason for the very high local heat-transfer coefficient. Finally, in the wall-jet region, the flow accelerates radially outward along the surface and then decelerates again as boundary-layer growth and wall friction take over. The local Nusselt number is highest at the stagnation point and then decreases monotonically with radial distance, although for small jet-to-target spacings (typically $H/D < 6$) a secondary peak may appear in the wall-jet region [11,12].

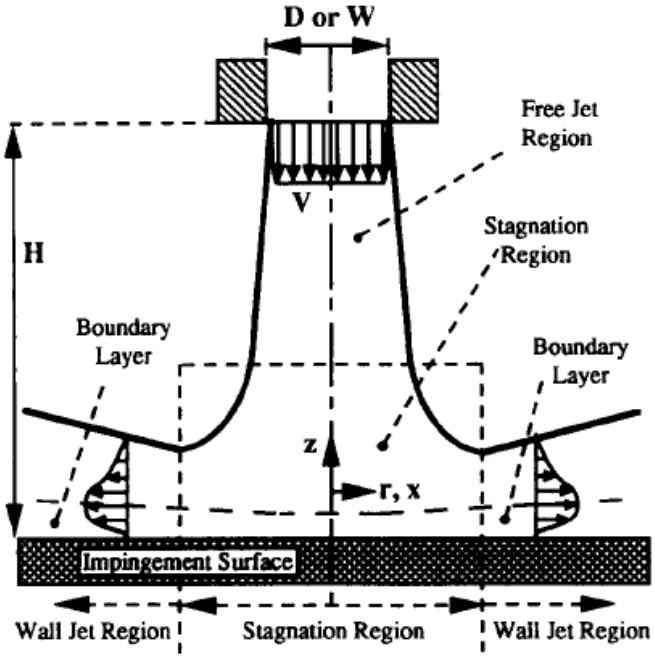

Figure 2.4 : Flow regions of a single round jet impinging on a flat surface [12].

Impingement cooling is preferentially applied at the leading edge of the airfoil, where the external heat load is at its highest and the geometry is highly curved [8]. A typical leading-edge configuration is shown schematically in Figure 2.5. As described by Chupp et al. [13] in one of the earliest detailed experimental studies of this geometry, a thin internal insert (or impingement tube) is positioned just inside the leading edge

with a row of small holes facing the inner curved wall; the cooling air enters the insert from the blade root, exits through the holes as a row of jets, and impinges directly on the concave inner surface of the leading edge. After impinging, the spent air either turns chordwise toward the trailing edge through the midchord cooling system or exits through the leading-edge film-cooling holes (the showerhead) to provide additional external film cooling on the highly curved leading-edge surface [1].

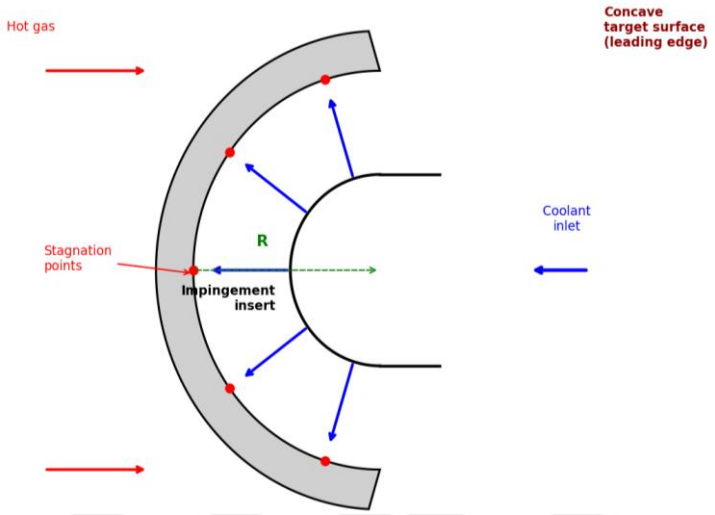

Figure 2.5 : Impingement cooling on a concave leading-edge surface of a turbine blade.

Multiple-row impingement arrangements are also used in midchord regions to cool the pressure and suction sides of the blade [1,3]. In these midchord regions, the jets are arranged in two-dimensional arrays—either inline or staggered—and the spent air is discharged either toward the trailing edge or through film-cooling holes located between the jets [1,9]. The thermal performance of an impingement system is governed by several geometric and flow parameters [11,12]:

- the jet Reynolds number $Re_D = u_{jet} \cdot D / \nu$, based on the jet hole diameter D and the jet velocity ujet, which is the dominant parameter governing the magnitude of the heat-transfer coefficient [11];

- the jet-to-target spacing ratio H/D, which controls how much of the high-momentum jet core actually reaches the wall before being eroded by the surrounding shear layer;

- the jet-to-jet pitch ratios X/D and Y/D (or simply P/D for a uniform array), which determine the degree of interaction between adjacent wall jets and the area-averaged heat-transfer level [14];

• the jet arrangement (in-line or staggered), which affects both the local heat-transfer pattern and the build-up of crossflow [14];

• the curvature of the target surface, which can either enhance or suppress heat transfer through the generation of Taylor–Görtler vortices on concave surfaces and the thickening of the boundary layer on convex surfaces [8];

• the amount of crossflow generated by the spent air of the upstream jets, which has been studied since the early experimental work of Metzger and Korstad [15] on a single line of jets in a deflecting crossflow.

Although impingement cooling provides outstanding heat-transfer rates, it has two important limitations [5,6]. First, the introduction of an impingement insert is itself a hardware modification that may locally weaken the structural strength of the blade and complicate manufacturing; for this reason, impingement is more easily applied to stator vanes than to rotor blades [6]. Second, in multi-row arrays the inevitable accumulation of spent air creates a crossflow that strongly interacts with the downstream jets and can severely degrade the heat-transfer performance if not properly accounted for in the design [9,15]. Figure 2.6 illustrates the progressive accumulation of crossflow in a typical multi-row impingement array, with the jets of successive rows being progressively deflected away from the normal direction by the growing crossflow. The latter effect is the central technical motivation for the present numerical study and is therefore reviewed in detail in the following chapter.

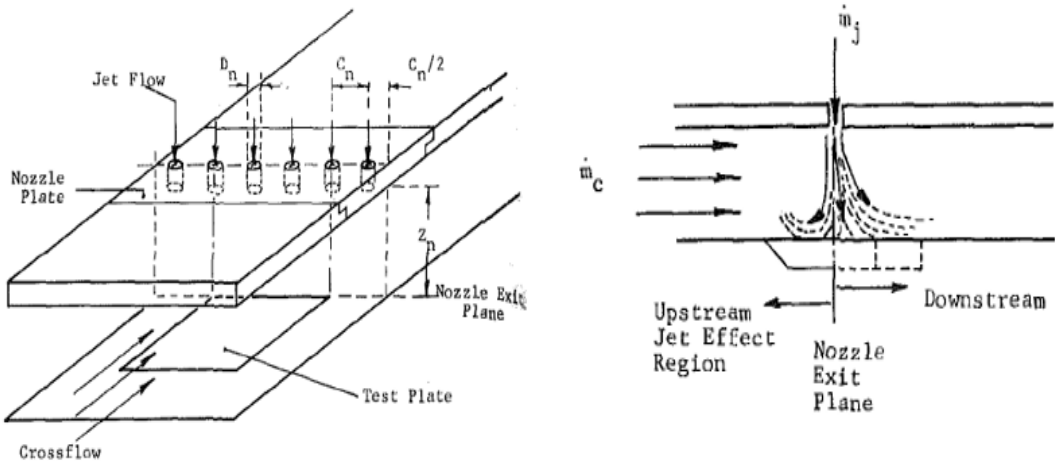

Figure 2.6 : Impingement jet array with progressive crossflow accumulation along the streamwise direction [15].

3. STUDIES ON JET IMPINGEMENT

Jet impingement heat transfer has attracted research attention for more than half a century, motivated by applications ranging from glass tempering and paper drying to electronics cooling and gas-turbine-blade cooling. The literature is therefore vast, and the present chapter reviews only those studies most directly relevant to the gas-turbine impingement-cooling problem under crossflow that is the focus of this thesis. The chapter is organized into five parts: Section 3.1 reviews fundamental single-jet impingement studies; Section 3.2 covers impingement on concave (leading-edge) surfaces; Section 3.3 reviews impingement arrays in crossflow; Section 3.4 surveys numerical studies and discusses turbulence-modelling considerations; and Section 3.5 identifies the knowledge gap and states the specific objectives of the present work.

3.1 Fundamentals of Single Jet Impingement

The earliest investigations of jet impingement heat transfer focused on a single round or slot jet impinging normally on a flat plate. The most influential early synthesis is the comprehensive review by Martin [11], who collected experimental data from a wide range of nozzle geometries and operating conditions and proposed compact correlations for the average Nusselt number as a function of the jet Reynolds number, the Prandtl number, the dimensionless nozzle-to-target spacing H/D, and the relative nozzle area. Martin's correlations remain widely used today as a reference benchmark for new experimental and numerical results. Subsequent reviews by Jambunathan, Lai, Moss, and Button [16], by Viskanta [12], and by Zuckerman and Lior [6] extended this synthesis to additional configurations. Jambunathan et al. [16] in particular collected an extensive set of single-jet heat-transfer data covering a wide range of Reynolds numbers and nozzle-to-target spacings, and proposed correlations for the average Nusselt number that have since become a standard reference benchmark in the impingement-cooling literature. Viskanta [12] in particular emphasizes the role of the radial pressure distribution and the radial velocity gradient in setting the stagnation-point heat-transfer coefficient, and notes that for small separation distances (H/D = 1.2

in his examples) impingement happens within the potential core of the jet so that the distribution of the presssure is compatible with the non-viscous solution, while for larger H/D the velocity profile becomes more non-uniform and the pressure distribution becomes correspondingly broader. Han, Dutta, and Ekkad [3] and Weigand and Spring [17] provide more recent and gas-turbine-oriented overviews of the same fundamental material.

A second body of single-jet data that has had a strong influence on the development of CFD-grade turbulence models is the work of Cooper, Jackson, Launder, and Liao [18]. The authors performed careful hot-wire surveys of a normally impinging round turbulent jet at two Reynolds numbers (Re = 23 000 and 70 000) and at standoff ratios H/D ranging from 2 to 10, with detailed measurements at H/D = 2 and 6. Two key choices distinguish the Cooper experiment from earlier ones and explain its prominence in the model-validation literature. First, the jet was issued from a smooth pipe long enough to ensure fully developed turbulent flow at the orifice, and the same configuration was duplicated using two distinct pipe diameters (26 mm and 101.6 mm) so that Reynolds-number scaling could be cross-checked between the two facilities. Second, the operating point at Re = 23 000 was chosen to coincide exactly with the Nusselt-number measurements that Baughn and Shimizu had reported only a few years earlier, so that aerodynamic and thermal data sets could subsequently be combined when validating a CFD code. Cooper et al. recorded the mean velocity field near the plate along with the three meridional-plane Reynolds-stress components; a companion computational article based on their data showed that turbulence closures which mispredicted the mean velocity also failed on the Reynolds-stress level, establishing the Cooper data set as the de facto reference benchmark for impinging-jet RANS validation.

Two related single-jet studies by Goldstein and co-workers laid the experimental foundation for the way crossflow and oblique incidence deform the local heat-transfer footprint. In the first of these, Goldstein and Franchett [19] used a cholesteric-liquid-crystal heat-flux measurement technique—the crystal sheet was sandwiched between an electrically heated metallic foil on one side and a thermostatically controlled water bath on the other—to map the surface heat transfer beneath an obliquely impinging jet emerging from a 10 mm square-edged orifice. They covered impingement angles between 30° and 90°, separations L/D of 4, 6, and 10, and Reynolds numbers from 10

000 up to 35 000. Two principal findings emerged. First, the location of the peak heat-transfer coefficient drifts away from the geometric jet axis as the impingement angle becomes more oblique, and the magnitude of this drift correlates almost exclusively with the inclination angle. Second, an empirical correlation for the iso-Nu contours was constructed in which the local Nusselt number scales as $Re^{0.7}$ and the impingement angle enters as an explicit parameter. The companion paper by Goldstein and Behbahani [20] examined the same single-jet configuration but with a crossflow superimposed on the jet, and reported that the local Nu footprint loses its axial symmetry as the crossflow grows: the high-h region migrates downstream of the geometric stagnation point, the peak Nu drops, and the high-Nu region widens in the streamwise direction. The two Goldstein studies, taken together, provide the canonical single-jet evidence for the deflection-driven mechanism that, in array configurations, gives rise to the systematic streamwise degradation of stagnation-point heat transfer documented in Section 3.3. Earlier synthesis work by Bathie [4], framed in a gas-turbine context, also contributed to the basic understanding of stagnation-point heat transfer in cooled airfoils.

A consistent observation across these single-jet studies is that the Nusselt number scales approximately as Re_D^n, with the exponent n typically lying between 0.5 and 0.8 depending on H/D, surface curvature, and turbulence level [11,12,13]. The radial profile of the local Nusselt number frequently exhibits a secondary peak at small H/D values (typically $H/D < 6$), an effect attributed to a transition from laminar to turbulent flow in the wall jet and to ring-shaped vortical structures generated near the wall [11, 12]. The location of this secondary peak depends on the nozzle geometry, the local turbulence level of the impinging jet, and the value of H/D itself.

3.2 Impingement on Concave (Leading-Edge) Surfaces

Real turbine-blade leading edges are sharply curved, with curvature radii on the order of a single jet diameter, and the heat-transfer behaviour at such curvatures departs noticeably from what is observed on flat plates. The first dedicated experimental study of impingement on a small-radius concave wall typical of a real airfoil leading edge is that of Chupp, Helms, McFadden, and Brown [13]. Their motivation was that flat-plate correlations developed at large l/d ratios could not be safely extrapolated to the very small jet diameters present in real turbine blades, and that scale effects internal to the

cylindrical-target geometry made it necessary to test models at full scale rather than at convenient laboratory scale. Figure 3.1 illustrates the model. To measure local heat-transfer coefficients on the curved interior wall, the authors instrumented the model with thin platinum strips, dissipated a known electrical power in each strip, and reduced the resulting Joule heating to a spanwise-averaged Nusselt number. The correlation that came out of the campaign expresses the stagnation-strip Nu as a power law in Re with exponent 0.7, with parametric dependence on the three relevant length scales—the jet diameter d, the leading-edge diameter D, and the jet-to-target standoff l—and treats the chordwise decay Nu/Nu(0) separately as a function of the chordwise coordinate x/d, with l/d entering as an additional parameter.

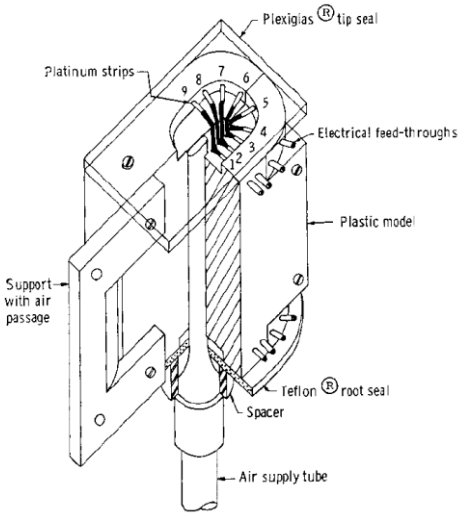

Figure 3.1 : Schematic of the model used by Chupp et al. [13].

Building on Chupp et al. [13], Metzger, Baltzer, and Jenkins [21] extended the same configuration to include explicit variations in leading-edge sharpness and demonstrated that the local heat-transfer coefficient is sensitive to the radius of curvature at the airfoil nose. Subsequently, Bunker and Metzger [22] published a detailed local-h data set on a representative airfoil leading edge under jet impingement, with a power-law dependence on Re of approximately $Re^{0.6}$ and significant additional sensitivity to three further parameters: the leading-edge sharpness, the jet-to-jet pitch-to-diameter ratio, and the standoff distance. Their measurements have been adopted as a standard CFD-validation benchmark for leading-edge impingement work, employed for example in the recent numerical study of Madwesh, Purohit, and Karanth [23].

From a fluid-mechanical perspective, target curvature affects the local heat transfer through two mechanisms that act in opposite directions [8,12]. On the one hand, the

centrifugal acceleration produced by the curved streamlines along the wall destabilizes the flow, in particular by promoting longitudinal Taylor–Görtler vortices, which intensify the near-wall turbulent mixing and therefore enhance the local h. On the other hand, the spent wall-jet fluid spreads outward along a divergent (curved) surface, and this divergence adversely affects the boundary-layer development. The net effect on the local Nu depends on the dimensionless curvature, on the jet Reynolds number, and on the standoff distance, and is therefore not amenable to a single universal correlation. Forster and Weigand [8] remark that, on a strongly concave target, the local Nu footprint typically takes a characteristic figure-of-eight shape in the stagnation region of each jet, accompanied by additional zones of elevated h between the jets due to the secondary fountain flow that is set up by the colliding wall jets.

3.3 Impingement Arrays and Crossflow

In practical turbine-blade cooling, single isolated jets are very rarely used; multiple-jet arrays are nearly universal. The original experimental reference for the average heat transfer of a square array of round jets striking a flat surface is the campaign of Kercher and Tabakoff [14], which is also the first to account explicitly for the influence of the spent jet flow on the heat transfer in the downstream rows. The Nu correlations that resulted from [14]—expressed as functions of the jet Re, the hole spacings normalized by the diameter, the standoff ratio, and the spent-air mass-flow ratio—became canonical design tools for impingement-array cooling. They continue to be cited in essentially every subsequent multi-jet impingement study and in the principal gas-turbine textbooks [3,11].

The picture sketched by Kercher and Tabakoff was sharpened considerably by the NASA-supported experimental programme of Florschuetz, Truman, and Metzger [9] at Arizona State University, which produced spanwise-row-resolved Nusselt-number correlations for two-dimensional impingement arrays operated under crossflow. The arrays studied in [9] include both inline and staggered hole patterns, and the spent jet flow is forced to exit in a single streamwise direction along the channel that is formed between the jet plate and the heat-transfer surface. The parameter window of the experiment is broad: jet Reynolds numbers Rej from 2.5×10^3 up to 7×10^4, crossflow-to-jet velocity ratios G_c/G_j between 0 and 0.8, streamwise pitches x_n/d from 5 to 15 for the inline patterns (5 to 10 for the staggered ones), spanwise pitches y_n/d from 4 to 8,

and channel heights z/d from 1 to 3. The central conclusion of [9] is that the row-resolved heat-transfer coefficient at any given spanwise row is governed by only three parameters—the local jet Reynolds number Rej of that row, the local velocity ratio Gc/Gj experienced at that row, and the geometric ratios (x_n/d, y_n/d, z/d). In addition to the heat-transfer correlations, [9] also derived and validated a one-dimensional streamwise momentum model that, given the discharge coefficient of the jet plate, accurately predicts the row-by-row split between jet and crossflow flows; the same one-dimensional model also showed that, in inline arrays, the crossflow channels itself preferentially between adjacent streamwise jet rows, generating a non-uniform spanwise velocity distribution in which the inter-row velocity exceeds the velocity directly upstream of the next jet.

A companion paper of the same NASA programme, Florschuetz, Berry, and Metzger [24], focused specifically on the periodicity of the local heat-transfer coefficient along the streamwise direction in the same inline and staggered arrays. The authors quantified, row by row, the deviation of the local h from the value measured at the first (upstream) row as the streamwise crossflow accumulates, and concluded that this deviation is most severe for inline arrays operated at low channel-height-to-diameter ratios z/d. Read together with the row-resolved correlations of [9] above and the initial-crossflow extension of [25] discussed next, the three Florschuetz contributions [9,24,25] constitute a self-consistent body of design data that covers the principal features of jet-array impingement under streamwise-accumulating crossflow.

The third Florschuetz publication, Florschuetz, Metzger, and Su [25], extended the above correlations to a configuration in which the array is exposed to an initial (preexisting) crossflow that enters from upstream of the first jet row, the situation that most closely emulates the midchord region of a real airfoil where the spent coolant from the leading-edge cavity arrives as crossflow at the midchord array. The geometric matrix examined in [25] consists of streamwise/spanwise pitch combinations (x_n/d, y_n/d) of (5, 4), (5, 8), (10, 4), and (10, 8) at the three z/d values of 1, 2, and 3, with the average jet Reynolds number held near 10^4 and the initial-to-total crossflow mass ratios m_c/m_j set at 0.2, 0.5, and 1.0. The principal observation is that the introduction of an initial crossflow generally lowers the mean Nu over the array, since although the jet flow itself is held nearly constant the total coolant budget rises. The only exceptions are some of the z/d = 1 cases, where one or more of the initial-crossflow runs gave a

slightly higher mean Nu than the corresponding zero-initial-crossflow run; even in those cases, however, the comparison turns unfavorable once the data are normalized per unit of total coolant flow rate. A further conclusion of [25] is that, whenever the upstream crossflow has been preheated above the jet temperature—as is the case when the coolant has already collected heat from the leading-edge cavity before reaching the midchord—the effective coolant temperature seen by the midchord surface is no longer simply the jet plenum temperature, and the local design model must include both the aerodynamic jet deflection and the thermal mixing of the two streams.

The basic mechanism by which a crossflow degrades array impingement was already isolated experimentally by Metzger and Korstad [15] in a configuration consisting of a single line of round jets striking a flat target with the spent flow of the upstream jets exhausted along the wall as crossflow on the downstream jets. They found that the upstream-side Stanton ratio (St divided by its zero-crossflow value) drops monotonically as the crossflow rate is increased, while the downstream-side Stanton ratio is non-monotonic when the jet-to-jet spacing is tight ($C_n/D_n < 3.0$), passing through a relative minimum on the upstream face and a relative maximum on the downstream face at moderate crossflow rates. Their interpretation rests on two competing effects that occur simultaneously as the crossflow grows. The first is that the jet is bent away from the wall normal, which lowers the local heat-transfer coefficient at the geometric stagnation point. The second is that the actual impingement footprint is displaced downstream, which causes a larger fraction of the downstream area to be exposed to the high-coefficient region of the deflected jet. For small jet pitches, the two effects partially compensate one another and produce the non-monotonic Stanton ratio; for larger pitches, the first effect dominates and the heat-transfer rate falls monotonically as the crossflow strengthens.

A second comprehensive data set on staggered jet arrays subjected to streamwise crossflow was reported by Hollworth and Cole [26], who fitted the test piece with side skirts so that the entire spent flow was forced to exhaust through one end of the channel. The matrix tested in [26] comprises three hole patterns (X, Y) = (4d, 4d), (4d, 8d) and (8d, 4d), three standoff ratios Z/d = 1, 2, 3, and three numbers of streamwise rows N = 4, 6, 8, all spanning jet Reynolds numbers from 2 500 up to 25 000. The local heat-transfer coefficient was extracted from microfoil heat-flux sensors approximately 0.3d wide in the streamwise direction—comfortably smaller than the

hole spacing—giving excellent local spatial resolution. The principal finding of [26] is that the spanwise-averaged streamwise distribution of h is periodic, with one peak per spanwise row, and that as the crossflow accumulates the row-aligned peaks drift downstream, with the largest displacements occurring close to the exhaust end of the channel. After numerical integration of the local data, the array-averaged Nu values produced by [26] were checked against the earlier Kercher–Tabakoff correlation [14] over the parameter range that the two studies share, and the agreement was good, providing an independent cross-validation of both data sets.

San and Lai [27] investigated the optimum jet-to-jet spacing for staggered arrays of impinging air jets and provided design correlations for the area-averaged Nusselt number as a function of the streamwise pitch x/d, the spanwise pitch y/d, and the jet Reynolds number Re_j over a wide range of these parameters. They identified the spacing values that maximize the area-averaged Nusselt number under their test conditions, providing a useful complement to the Kercher–Tabakoff and Florschuetz correlations for the design of practical impingement systems.

More recent overviews of multi-jet impingement performance are provided by the review article of Weigand and Spring [17] and by the edited volume of Amano and Sundén [28]. Weigand and Spring [17] argue that, in array configurations, the inter-jet interactions can be sorted into two distinct categories: a pre-impingement interaction in which the cores of two neighboring jets begin to merge before either of them has reached the target wall (important at small jet pitches and large standoffs), and a post-impingement interaction in which an arriving jet sees a wall already covered by the wall-jet flow of the neighboring jets (important at small pitches, small standoffs, and high jet velocities—i.e. precisely the conditions under which crossflow becomes strong). They also stress that the design of the outflow path is what ultimately sets the level of crossflow within the cavity. The chapters of [28] collectively cover impingement design, applications, configurations, combustor-liner cooling, impingement–effusion hybrids, flow control, swirling jets, and rib-roughened impingement, and so represent a useful modern complement to the older but still authoritative review papers of Martin [11] and Viskanta [12]. A sufficiently strong crossflow systematically lowers the stagnation-point heat transfer and homogenizes the local Nu distribution, because deflected jets no longer impinge perpendicularly on

the wall [9,15,20]. As a consequence, both the peak-to-mean ratio and, in the affected rows, the global level of the Nu distribution drop with increasing crossflow.

3.4 Numerical Studies and Turbulence Modelling

Numerical simulation has long been an indispensable companion to experimental work on impingement cooling, but, as the comprehensive review of Zuckerman and Lior [6] makes clear, the impinging-jet flow field stands among the most demanding test cases for any RANS turbulence closure. Several distinct physical phenomena coexist within only a few jet diameters and each of them stresses some of the standard modelling assumptions: a strongly stagnating flow with high normal-strain rates, low turbulence anisotropy in the impingement core, a curved wall-jet boundary layer subjected to a non-trivial streamwise pressure gradient, and a free shear layer whose spreading rate has to be accurately captured. Within this context, the relative behaviour of the most common closures is now well understood [6]. The standard k–ε family overestimates the turbulent kinetic energy in the stagnation zone—an artefact of the Boussinesq isotropic-eddy-viscosity hypothesis applied to a flow with strong normal strain—and consequently can over-predict the local Nu by as much as 60 %. Variants of the k–ω family fare better in the wall-jet region but suffer from the well-known sensitivity to freestream values of ω. The Menter k–ω SST model, by combining the better near-wall behaviour of k–ω with the better freestream behaviour of k–ε, achieves an attractive compromise: stagnation-point and wall-jet Nu values typically fall within 20–40 % of experimental data and the mean velocity field is captured very well [6]. More elaborate two-equation models (v^2–f) and full Reynolds-stress closures yield further improvements but at appreciable computational cost; LES and DNS are more accurate still but remain prohibitive for the engine-scale geometries of practical interest. Several chapters of the Amano and Sundén volume [28] reinforce and extend these conclusions over a wider variety of impingement configurations.

More recent CFD-driven leading-edge studies have built directly upon the foundations laid by these earlier experiments. The combined experimental and numerical study of Forster and Weigand [8] has already been introduced above and is the validation reference of the present thesis (see Chapter 5); for completeness it is summarized once here in the literature-review context. Their test piece is a generic gas-turbine blade leading edge with nine round impingement jets arranged in a single row and a target

wall whose curvature radius equals the jet diameter, supplemented by film-cooling holes of half the jet diameter (D_{fc} = 0.5 D_{jet}) staggered between adjacent jets at an inclination of 45°. Two standoff ratios (H/D_{jet} = 2.7 and 4) and three independently controlled crossflow regimes (no, intermediate, and maximum) were examined at a single Reynolds number of 30 000. The local heat-transfer coefficient on the inner perspex wall was obtained by the transient TLC method, with the indication temperature read from the green channel of the camera output. The accompanying RANS simulations, run in OpenFOAM with the k–ω SST closure, reproduced the measured Nu fields to within the experimental uncertainty and captured the dominant flow features correctly. From the parametric variations the authors concluded that crossflow simultaneously lowers the peak (stagnation) Nu and the overall surface-averaged Nu but flattens the local distribution, and that decreasing the standoff to H/D_{jet} = 2.7—although it strengthens the crossflow inside the cavity—nevertheless increases the global heat-transfer level.

In a more recent CFD investigation, Madwesh, Purohit, and Karanth [23] examined the leading-edge cooling of a high-pressure turbine blade in which the conventional cylindrical impingement nozzles are replaced by an array of converging-shape nozzles. Their simulations were performed in Ansys Fluent with the k–ω SST closure and swept a multi-dimensional design space: jet flow Mach numbers between 0.2 and 0.8, nozzle converging ratios from 2 to 8 at two values of the throat diameter (0.25 and 0.5 mm), nozzle pitch between 3 and 5 mm, and lateral inter-jet distance between 3 and 6 mm. Their post-processing distinguished a primary stagnation zone—on which the Nu enhancement relative to a reference is largest—from a weaker secondary stagnation zone further along the wall. The principal trends extracted from the parametric data set are: (i) crossflow significantly suppresses the peak local Nu in the downstream half of the array; (ii) the peak Nu enhancement is maximized at high jet Mach numbers combined with small jet-to-target distances and large converging ratios at the smaller throat diameter; and (iii) the average Nu over the array tends to grow as the nozzle pitch is reduced.

Miao, Wu, and Chen [29] reported a steady three-dimensional incompressible RANS investigation of confined multiple-jet impingement onto a flat target at gas-turbine-relevant Reynolds numbers, Re_j between 2440 and 14640. Both staggered and inline configurations were considered, with three values of the jet-to-plate spacing ratio Z_n/d_j

(1, 3, and 6) and three different crossflow-exit orientations (parallel, hybrid, and counter) chosen to emulate practical exhaust configurations. The turbulence closure was the realizable k–ε model with the enhanced wall-treatment option, and the simulations returned full local Nu fields on the target. The principal conclusions of [29] are: that the area-averaged Nu rises monotonically with Re_j; that the inline arrangement combined with the hybrid crossflow orientation boosts the area-averaged Nu over the cases considered; that thermal performance benefits from reducing Z_n/d_j from 6 to 3, but that a further reduction to $Z_n/d_j = 1$ produces a strongly non-uniform local Nu pattern irrespective of the crossflow orientation. The authors also fit a Reynolds-number-dependent correlation for the area-averaged Nu, separately for the inline and staggered patterns.

Wang, Sundén, Borg, and Abrahamsson [30] used liquid-crystal thermography to obtain detailed surface heat-transfer maps for an impinging jet inclined at 10° with respect to its target plate and operated in the presence of an external crossflow. Their parameter window covered three jet Reynolds numbers (Re_j = 20 000, 28 000, 40 000) and three crossflow Reynolds numbers (Re_C = 80 000, 112 000, 160 000) in the fully turbulent regime, with the velocity ratio $M = U_j/U_0$ held at intermediate values. The salient features of the resulting Nu maps are as follows: in the impingement region, the iso-Nu contours form an oval whose shape and orientation depend on both M and Rej; raising Rej at constant M shifts the location of peak Nu upstream and sharpens the bell-shape of the Nu profile through the stagnation point; and, perhaps most importantly for the design of practical configurations, in the wall-jet region downstream of the oval impingement core the local heat transfer demonstrates negligible sensitivity to Re_C, suggesting that under the conditions of [30] the crossflow primarily acts on the impingement region while leaving the wall-jet zone largely unaffected.

Beyond the impingement-only literature, the broader review of Naik [1] discusses how impingement is combined with rib turbulators and pin fins inside conjugate-heat-transfer-based design loops and points out the role of perspex test models and high-speed cascades in validating cooled-blade designs. Bunker [5] surveys the open challenges that remain for CFD-aided design of gas-turbine hot-gas-path components, with particular emphasis on validated turbulence closures, robust conjugate heat-transfer procedures, and accurate specification of the operating boundary conditions.

3.5 Knowledge Gap and Focus of the Thesis

The literature reviewed above demonstrates that jet impingement cooling has been extensively studied for several decades, both experimentally and numerically. The fundamental flow regions and the canonical correlations of Martin [11], Kercher and Tabakoff [14], and Florschuetz et al. [9,25] for both single jets and arrays under moderate crossflow are well established, and modern CFD with the k–ω SST turbulence model is capable of reproducing experimental heat-transfer data within a tolerance acceptable for engineering design [6,8,23]. However, several gaps remain that motivate the present work:

1. High-crossflow regimes are under-represented. Most published correlations—including those of Kercher and Tabakoff [14], Florschuetz, Truman, and Metzger [9], and Florschuetz, Metzger, and Su [25]—cover crossflow-to-jet velocity ratios up to moderate values. The single-jet study of Goldstein and Behbahani [20] and the inclined-jet study of Wang et al. [30] also concentrate on relatively moderate crossflow ratios. As impingement cooling is increasingly applied to highly loaded blades, to confined cavity geometries, and to configurations where the leading-edge crossflow feeds directly into tip regions, design data at high crossflow intensity are needed but remain scarce in the open literature.

2. Combined parametric maps for Re_D, H/D, and P/D are limited. Existing correlations often vary one or two parameters while keeping the others fixed at canonical values. A unified, closed-form description that simultaneously accounts for the dominant influence of the Reynolds number and the secondary, but coupled, effects of the jet-to-target spacing and the jet-to-jet pitch is still useful for preliminary design and for the rapid screening of cooling concepts.

3. Validation against modern experimental data combined with practical engineering correlations. Detailed CFD studies such as Forster and Weigand [8] and Madwesh et al. [23] provide highly resolved local heat-transfer fields, but a compact engineering correlation for the area-averaged Nusselt number under high-crossflow conditions, derived from a CFD campaign that has been validated against modern experimental data and that spans a wide parameter range, is valuable for designers who need a rapid evaluation tool at the conceptual-design stage. As Bunker [5] notes, such

compact engineering tools remain a recurrent need in the practical design of cooled hot-gas-path components.

The aim of the present thesis is therefore to perform a systematic numerical investigation of heat transfer in a generic gas-turbine blade with impingement cooling under a high crossflow effect. The specific objectives are:

- To develop and validate a three-dimensional CFD model of an impingement-cooling configuration representative of a generic turbine blade, using a RANS approach with an appropriate turbulence model selected on the basis of the modelling guidance available in the literature [6,8,23,28].
- To validate the numerical methodology against a corresponding experimental study available in the open literature, ensuring confidence in the predictive capability of the model and quantifying the residual modelling error.
- To carry out parametric simulations covering jet Reynolds numbers from 10 000 to 40 000, jet-to-surface spacing ratios H/D between 1.4 and 5.3, and jet-to-jet pitch ratios P/D between 2 and 8, all under a representative high crossflow condition with an intensity of approximately 60 %.
- To analyze the influence of these parameters on the area-averaged Nusselt-number distributions and on the underlying flow phenomena (jet deflection, stagnation-point degradation, and inter-jet interaction).
- To derive an empirical correlation for the area-averaged Nusselt number as a function of Re_D, H/D, and P/D, providing a compact and physically consistent design tool whose accuracy is quantified within the investigated parameter range.

The expected outcome is a validated set of CFD results and a single closed-form correlation that captures the dominant effect of the jet Reynolds number and the secondary but comparable influences of H/D and P/D under high-crossflow conditions, thereby supporting the preliminary design and optimization of impingement-cooled gas-turbine blades. The proposed correlation is anticipated to predict the numerical data with a mean absolute percentage error of approximately 4 %, demonstrating good accuracy within the investigated parameter range, and confirming the dominant role of the jet Reynolds number relative to the geometric parameters under high-crossflow operation.

4. COMPUTATIONAL FLUID DYNAMICS

This chapter presents the theoretical foundation of the computational fluid dynamics (CFD) framework that underpins the numerical simulations of the present thesis. The exposition starts from the fundamental conservation laws of fluid mechanics—mass, momentum, and energy—that govern any continuum flow. It then introduces the Reynolds averaging procedure that is applied to these equations to obtain the Reynolds-Averaged Navier–Stokes (RANS) equations used here, discusses the closure problem associated with the resulting Reynolds-stress terms, and finally describes Menter's k–ω shear-stress-transport (SST) turbulence model that is selected to close the RANS equations in this work. The presentation is consistent with the formulation implemented in the Ansys Fluent solver [31], which is used for all simulations of this thesis. At the end of the chapter, the rationale for choosing the k–ω SST model for the present impingement-cooling study is discussed.

4.1 Governing Equations of Fluid Flow

All fluid-flow phenomena in the absence of relativistic or quantum effects are described by three conservation laws applied to a continuum: conservation of mass, conservation of linear momentum, and conservation of energy [31]. In differential, conservative form and using Cartesian-tensor index notation with the Einstein summation convention over repeated indices, these laws can be written as follows.

4.1.1 Continuity equation

The continuity equation expresses the conservation of mass: the rate of change of mass within a fixed control volume must equal the net mass flux through its boundaries. In differential form it reads

$$\frac{\partial \rho}{\partial t} + \frac{\partial (\rho u_i)}{\partial x_i} = 0 \tag{4.1}$$

where ρ is the fluid density [kg/m³], u_i is the i-th component of the velocity vector [m/s], t is time [s], and x_i (i = 1, 2, 3) are the Cartesian coordinates. Equation (4.1) is valid for both compressible and incompressible flows. For an incompressible fluid, ρ

is constant in space and time, and the continuity equation reduces to the divergence-free condition $\partial u_i/\partial x_i = 0$ [31].

4.1.2 Momentum equations

The conservation of linear momentum in an inertial reference frame yields the Navier–Stokes equations [31]:

$$\frac{\partial(\rho u_i)}{\partial t} + \frac{\partial(\rho u_i u_j)}{\partial x_j} = -\frac{\partial p}{\partial x_i} + \frac{\partial \tau_{ij}}{\partial x_j} + \rho g_i + F_i \tag{4.2}$$

where p is the static pressure [Pa], τ_{ij} is the viscous stress tensor [Pa], g_i is the gravitational body force per unit volume [N/m³], and F_i represents any other external body force per unit volume (such as electromagnetic forces or porous-media resistance) [31]. The left-hand side of Equation (4.2) represents the local rate of change of momentum and the convective flux of momentum, while the right-hand side groups the surface forces (pressure gradient and viscous stresses) and the body forces.

For a Newtonian fluid, the viscous stress tensor is linearly related to the rate of strain through

$$\tau_{ij} = \mu\left(\frac{\partial u_i}{\partial x_j} + \frac{\partial u_j}{\partial x_i}\right) - \frac{2}{3}\mu\frac{\partial u_k}{\partial x_k}\delta_{ij} \tag{4.3}$$

where μ is the molecular (dynamic) viscosity [Pa·s] and δ_{ij} is the Kronecker delta. The first term on the right-hand side of Equation (4.3) is the deviatoric stress, while the second term accounts for volume dilatation and vanishes identically in incompressible flow [31].

4.1.3 Energy equation

For flows that involve heat transfer or compressibility effects, an additional conservation equation for energy is solved. In Ansys Fluent the total-energy form is used [31]:

$$\frac{\partial(\rho E)}{\partial t} + \frac{\partial}{\partial x_j}\Big(u_j(\rho E + p)\Big) = \frac{\partial}{\partial x_j}\left(k\frac{\partial T}{\partial x_j} + u_i\tau_{ij}\right) + S_h \tag{4.4}$$

where E is the specific total energy [J/kg], defined as the sum of internal and kinetic energy ($E = h - p/\rho + u_i u_i/2$, with h the specific enthalpy), k is the effective thermal conductivity [W/m·K], T is the static temperature [K], and Sh is a volumetric source

term that accounts for volumetric heat sources, radiation, chemical reactions, or other contributions to the energy balance [31]. The first term on the right-hand side represents heat conduction (Fourier's law combined with turbulent transport, when applicable), while the second represents viscous dissipation. In the present impingement-cooling study, the flow is essentially incompressible at the imposed Reynolds numbers, and the energy equation is solved in its low-Mach-number form to track the heat transfer between the heated target wall and the impinging jets.

Together, Equations (4.1), (4.2), and (4.4) constitute a closed set when complemented by an equation of state (typically the ideal-gas law for compressible flows or the constant-density assumption for incompressible flows) and by appropriate boundary conditions on the velocity, pressure, and temperature. This system describes laminar flow exactly. For turbulent flow, however, the chaotic, unsteady, three-dimensional nature of the velocity and pressure fields makes a direct solution prohibitively expensive for engineering applications, and an averaging procedure is therefore introduced.

4.2 Reynolds Averaging and the RANS Equations

Turbulent flows are characterized by a wide spectrum of temporal and spatial scales: the largest, energy-containing eddies are of the order of the geometric length scale of the problem, while the smallest, dissipative (Kolmogorov) eddies may be many orders of magnitude smaller. Resolving all these scales directly—as in Direct Numerical Simulation—is computationally feasible only for very simple geometries at modest Reynolds numbers. For the engineering Reynolds numbers considered in this thesis (ReD up to 4×10^4 inside complex internal cooling cavities), the Reynolds-Averaged approach is adopted, in which the focus is shifted from the instantaneous flow variables to their statistical averages.

Following Reynolds, every instantaneous flow variable ϕ is decomposed into a time-averaged (or, more generally, ensemble-averaged) mean component $\bar{\phi}$ and a fluctuating component ϕ' [31]:

$$u_i = \overline{u}_i + u_i', \qquad p = \overline{p} + p' \tag{4.5}$$

By definition, the time average of the fluctuating part is zero: $\phi' = 0$. When this decomposition is substituted into the continuity and momentum equations, and the time-averaging operator is applied to the resulting equations, the so-called Reynolds-Averaged Navier–Stokes (RANS) equations are obtained [31]:

$$\frac{\partial \rho}{\partial t} + \frac{\partial (\rho \overline{u}_i)}{\partial x_i} = 0 \tag{4.6}$$

$$\frac{\partial (\rho \overline{u}_i)}{\partial t} + \frac{\partial \left(\rho \overline{u}_i \overline{u}_j\right)}{\partial x_j} = -\frac{\partial \overline{p}}{\partial x_i} + \frac{\partial}{\partial x_j}\left[\mu\left(\frac{\partial \overline{u}_i}{\partial x_j} + \frac{\partial \overline{u}_j}{\partial x_i}\right)\right] + \frac{\partial}{\partial x_j}\left(-\rho \overline{u_i' u_j'}\right) \tag{4.7}$$

Equation (4.6) is formally identical to the original continuity equation but written in terms of the mean velocity. Equation (4.7), the RANS momentum equation, is also formally similar to the Navier–Stokes equation but contains an additional term on the right-hand side that arises from the non-linearity of the convective term: the Reynolds-stress tensor, defined as

$$\tau_{ij}^{R} = -\rho \overline{u_i' u_j'} \tag{4.8}$$

Physically, the Reynolds-stress tensor τ_{ij}^{R} represents the momentum flux carried by the turbulent fluctuations: the turbulent eddies transport momentum across mean-velocity gradients in the same manner as molecular diffusion does, but several orders of magnitude more efficiently. Mathematically, however, the appearance of the new tensor introduces six additional unknowns (the three diagonal components and the three off-diagonal components, since the tensor is symmetric) into the system. The number of equations remains four (one continuity, three momentum), so the RANS system is no longer closed. This is the well-known closure problem of turbulence modelling [31].

Two distinct strategies exist to close the RANS equations [31]. The first is the Reynolds Stress Model (RSM), in which separate transport equations are solved for each of the six independent components of the Reynolds-stress tensor; this approach captures the anisotropy of turbulence at the cost of solving five (in 2D) or seven (in 3D) additional transport equations. The second strategy, used in the present work, is the eddy-viscosity (Boussinesq) approach. The Boussinesq hypothesis postulates an analogy between molecular and turbulent momentum transfer and writes the Reynolds stress as proportional to the mean strain rate through a turbulent (eddy) viscosity μt [31]:

$$-\rho\overline{u_i'u_j'} = \mu_t\left(\frac{\partial\overline{u}_i}{\partial x_j}+\frac{\partial\overline{u}_j}{\partial x_i}\right)-\frac{2}{3}\left(\rho k+\mu_t\frac{\partial\overline{u}_k}{\partial x_k}\right)\delta_{ij} \tag{4.9}$$

where k is the turbulence kinetic energy. With this hypothesis, the closure problem is reduced to determining a single scalar quantity, the eddy viscosity μ_t, instead of six independent stress components. The Boussinesq hypothesis works well for many shear-dominated flows such as wall boundary layers, mixing layers, and jets, although it implicitly assumes that the turbulence is locally isotropic, which is not strictly true [31]. Under this hypothesis, two-equation eddy-viscosity models such as k–ε, k–ω, and k–ω SST close the system by solving two additional transport equations for two turbulence scalars and constructing μt from them.

4.3 The k–ω SST Turbulence Model

The k–ω shear-stress-transport (SST) turbulence model was developed by Menter [32] to combine the advantageous near-wall behaviour of the original Wilcox k–ω model with the freestream-independence of the standard k–ε model. In its modern form, as implemented in Ansys Fluent, the SST model solves two additional transport equations—one for the turbulence kinetic energy k and one for the specific dissipation rate ω—and constructs the eddy viscosity μ_t from k, ω, and the local strain rate. The model uses two blending functions to switch automatically between a k–ω formulation in the near-wall region and a transformed k–ε formulation in the freestream and shear-layer regions, thereby retaining the strengths of both approaches.

4.3.1 Transport equation for the turbulence kinetic energy

The transport equation for the turbulence kinetic energy k [m²/s²] takes the form [31]:

$$\frac{\partial(\rho k)}{\partial t}+\frac{\partial\left(\rho\overline{u}_j k\right)}{\partial x_j}=\frac{\partial}{\partial x_j}\left[\left(\mu+\frac{\mu_t}{\sigma_k}\right)\frac{\partial k}{\partial x_j}\right]+\tilde{P}_k-\beta^*\rho k\omega \tag{4.10}$$

The terms on the left-hand side represent (in order) the local rate of change of k and the convective transport of k by the mean flow. On the right-hand side, the first term is the molecular and turbulent diffusion of k (with the turbulent contribution scaled by $1/\sigma_k$), the second term $\tilde{P}_k$ is the production of k due to mean-velocity gradients, and the third term $\beta^*\rho k\omega$ is the destruction of k by the small-scale turbulent dissipation. The production term is computed from the Reynolds-stress–strain-rate inner product but is limited by a clipping factor to prevent the unphysical accumulation of k in stagnation

regions, which is one of the well-known weaknesses of the standard k–ε family of models [31].

4.3.2 Transport equation for the specific dissipation rate

The transport equation for the specific dissipation rate ω [1/s] takes the form [31]:

$$\frac{\partial(\rho\omega)}{\partial t}+\frac{\partial\left(\rho\overline{u}_j\omega\right)}{\partial x_j}=\frac{\partial}{\partial x_j}\left[\left(\mu+\frac{\mu_t}{\sigma_\omega}\right)\frac{\partial\omega}{\partial x_j}\right]+\alpha\frac{\rho}{\mu_t}\tilde{P}_k-\beta\rho\omega^2 +2(1-F_1)\rho\sigma_{\omega 2}\frac{1}{\omega}\frac{\partial k}{\partial x_j}\frac{\partial\omega}{\partial x_j} \tag{4.11}$$

The terms on the right-hand side represent, in order: (i) the molecular and turbulent diffusion of ω; (ii) the production of ω, which is proportional to the production of k; (iii) the destruction of ω; and (iv) the cross-diffusion term that originates from the transformation of the k–ε dissipation equation into k–ω form and is activated only in the outer flow through the blending function F_1 [31]. The function F_1 equals one in the near-wall region (where the cross-diffusion term is switched off and the model reduces to the original k–ω model) and zero in the freestream (where the cross-diffusion term is switched on and the model reduces to the standard k–ε model in disguise). The blending function F_1 is given by

$$F_1=\tanh\left\{\left[\min\left(\max\left(\frac{\sqrt{k}}{\beta^*\omega y},\frac{500\nu}{y^2\omega}\right),\frac{4\rho\sigma_{\omega 2}k}{CD_{k\omega}y^2}\right)\right]^4\right\} \tag{4.12}$$

where y is the distance to the nearest wall, ν is the kinematic viscosity, and $CD_{k\omega}$ is a positive function of the cross-diffusion term [31].

4.3.3 Eddy viscosity

The eddy viscosity in the SST model is computed from k and ω with an additional limiter that enforces the so-called shear-stress-transport assumption in adverse-pressure-gradient boundary layers [31]:

$$\mu_t=\frac{\rho a_1 k}{\max(a_1\omega,SF_2)} \tag{4.13}$$

where a_1 is a constant ($a_1 = 0.31$), S is the magnitude of the strain-rate tensor, and F_2 is a second blending function defined by

$$F_2 = \tanh\left\{\left[\max\left(\frac{2\sqrt{k}}{\beta^*\omega y}, \frac{500\nu}{y^2\omega}\right)\right]^2\right\} \tag{4.14}$$

F_2 is constructed so that it equals one inside boundary layers and zero in free-shear flows. The limiter in Equation (4.13) prevents the eddy viscosity from becoming too large in regions of strong shear (such as separated boundary layers under adverse pressure gradients) and is the principal feature that distinguishes the SST formulation from the original Wilcox k–ω model [31]. This limiter improves the prediction of flow separation and of the wall shear stress, both of which are critical in impingement-cooling applications where the spent jet flow forms a wall jet under a strong adverse pressure gradient.

4.4 Justification of the k–ω SST Model for the Present Work

The selection of an appropriate turbulence model is one of the most consequential modelling decisions in any RANS-based CFD study, particularly for impingement cooling, where stagnation flow, wall-bounded shear, and free-shear-layer mixing all coexist within a few jet diameters. As discussed in Section 3.4 and reviewed in detail by Zuckerman and Lior [6], no two-equation eddy-viscosity model is capable of perfectly reproducing the heat transfer in the impinging-jet configuration; nevertheless, the relative merits and weaknesses of the different model families are well documented, and a practical compromise must be chosen for engineering computations.The k–ω SST model is selected for the present work for the following reasons:

- Validated track record in impingement-cooling CFD. Recent peer-reviewed numerical studies of leading-edge impingement cooling, including Forster and Weigand [8] and Madwesh, Purohit, and Karanth [23], as well as several chapters of the dedicated edited volume by Amano and Sundén [28], have used the k–ω SST model and demonstrated good agreement with high-quality experimental data. Using the same model in the present work facilitates direct comparison with these published results.

- Best compromise between accuracy and computational cost. Zuckerman and Lior [6] note that, among the RANS models in widespread engineering use, the SST model typically predicts impinging-jet Nusselt numbers within 20–40 % of

experimental values, outperforming both the standard k–ε family (which can produce errors of up to 60 % in stagnation regions) and the original Wilcox k–ω model (which is highly sensitive to freestream values of ω). The benchmark RANS study of Behnia, Parneix, and Durbin [33] for an axisymmetric turbulent jet impinging on a flat plate confirmed that the standard k–ε model is unreliable in the stagnation region and that more advanced near-wall closures are required for quantitative agreement with experimental Nusselt-number distributions; the SST model has since become the recommended baseline two-equation model for impingement-cooling RANS simulations. More accurate alternatives such as the v^2–f model used by Behnia et al. [33] and full Reynolds-stress closures exist but are computationally significantly more expensive and require finer meshes for stable convergence.

- Robust near-wall treatment. The SST model integrates directly through the viscous sublayer and avoids the need for empirical wall functions, provided the first cell is placed at $y^+ \lesssim 1$. This is critical for accurate prediction of the heat-transfer coefficient on the target wall.

- Improved performance under adverse pressure gradients and separation. The shear-stress-transport limiter in Equation (4.13) prevents the over-prediction of eddy viscosity in regions of strong shear, an issue that affects most other two-equation models. This is particularly relevant for impingement cooling under crossflow, where the deflected jets and the resulting wall jets exhibit strong streamwise pressure gradients and incipient separation behind the impingement points, as observed experimentally by Goldstein and Behbahani [20] and by Wang et al. [30].

It is acknowledged that the k–ω SST model, like all eddy-viscosity models that rely on the Boussinesq hypothesis, assumes locally isotropic turbulence so cannot exactly reproduce the footprint observed by Forster and Weigand [8] under impinging jets on concave surfaces, where streamline curvature and Taylor–Görtler vortices generate strongly anisotropic turbulence. This limitation typically manifests as a slight over-prediction of the stagnation-point Nusselt number in CFD compared with experimental data; however, for the area-averaged Nusselt numbers and for the parametric trends are the primary objective of the present work, the model has been shown to be sufficiently accurate. The residual modelling error is quantified through validation against experimental data in Chapter 5 and is considered when interpreting the parametric results in Chapter 6 .

5. VALIDATION CASE

Validation of the numerical methodology against an experimental reference is an indispensable step before any parametric campaign is launched, because it quantifies the level of error introduced by the modelling choices of Chapter 4 in a controlled, well-documented setting. This chapter therefore reproduces a published experimental data set with the present CFD methodology and compares the two on a like-for-like basis. The validation case has been selected so that the geometry of the reference experiment and the operating range covered there match the configuration of interest of the present thesis as closely as possible. The remainder of the chapter is organised in three parts: Section 5.1 introduces the experimental reference adopted for the validation, Section 5.2 specifies the CFD model used to simulate it, and Section 5.3 reports the resulting comparison together with a brief discussion of the residual disagreement.

5.1 Validation Case Introduction

Prior to executing the parametric simulation campaign that constitutes Chapter 6, the present chapter benchmarks the chosen numerical approach against a published experimental data set with the goal of demonstrating that the methodology can reproduce measured heat-transfer behaviour to engineering accuracy. The combined experimental–numerical study reported by Forster and Weigand [8] at the Institute of Aerospace Thermodynamics (ITLR), University of Stuttgart, has been adopted for this purpose. Two factors made this work the most appropriate benchmark available in the open literature.

First, the geometric arrangement examined in [8]—nine round impingement jets discharging onto a concave target plate that also carries a staggered film-cooling hole pattern—matches the configuration of interest of the present thesis almost one-for-one. Second, the authors report spatially resolved Nusselt-number distributions taken at engine-representative Reynolds numbers and at three independently controlled levels of internal crossflow. The four sub-sections that follow document, on the basis of a

careful re-reading of [8], the test rig, the geometry of the perspex test piece, the family of crossflow configurations together with the operating-point matrix, and the transient liquid-crystal procedure used to extract the heat-transfer coefficients—all elements that the reader needs to understand before turning to the validation comparison reported in Section 5.3.

5.1.1 Experimental rig

Figure 5.1 sketches the test facility used by Forster and Weigand [8]. The loop is configured as a draw-through (suction-mode) circuit: the working air is pulled across the test section by a vacuum pump positioned at the downstream end of the line, rather than being delivered under positive pressure. Atmospheric air enters through a particulate inlet filter and is then heated almost instantaneously—within under one second—from ambient temperature to roughly 70 °C by an electrically energized wire-mesh heater. The very short rise time of this near-step temperature change is essential, because it provides the boundary condition required to interpret the transient liquid-crystal procedure of Section 5.1.4. Downstream of the heater, the conditioned stream enters a settling plenum of converging cross-section that flattens the temperature and velocity profiles, with strategically placed thermocouples and wall-pressure taps used to verify the resulting flow uniformity.

The fluid then reaches the transparent perspex test piece that emulates a blade leading edge; nine thermocouples positioned at the geometric center of each impingement-jet nozzle continuously record the local reference temperature on which the subsequent heat-transfer evaluation depends. After leaving the test piece, the spent air is gathered in an outlet plenum that distributes the suction equally to all exit ports, and the static pressure inside this plenum is itself read by dedicated pressure taps. Before being expelled by the vacuum pump, the working fluid is metered by a Venturi nozzle sized according to DIN EN ISO 5167; the differential pressure across the nozzle yields the integral mass-flow rate of the run.

Optical access to the test piece is provided by a single camera mounted approximately two meters from the model, with two folding mirrors used to bring both halves of the leading-edge span into a common field of view, so that the entire spanwise extent of the TLC colour play can be recorded with one device.

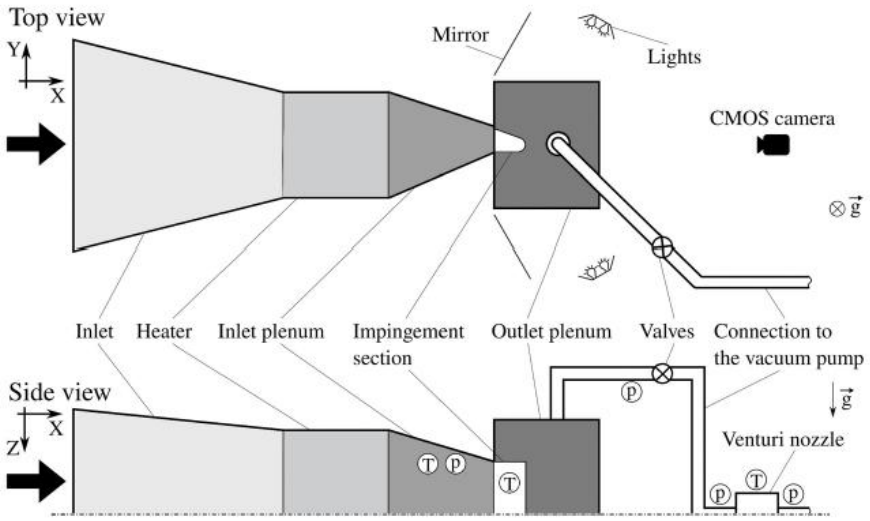

Figure 5.1 : Schematic of the experimental rig used by Forster and Weigand [8].

5.1.2 Leading-edge geometry

The internal geometry of the perspex test piece is presented in Figure 5.2. It comprises a curved central segment whose radius of curvature equals the impingement-jet diameter ($R = D_{jet}$) and which is flanked on both sides by short straight sections; together these mimic the cross-sectional shape of a typical gas-turbine blade leading edge. An exchangeable insert—$2\,D_{jet}$ thick and slid into the model through a side opening—houses nine cylindrical bores of diameter D_{jet} arranged at a uniform streamwise pitch of $4\,D_{jet}$, and it is these bores that act as the impingement jets during a run. Altering the geometry of the insert (or replacing it with a different one) shifts the apex of the curved target surface relative to the jet exit plane, so the standoff distance H, and therefore the ratio H/D, can be varied without otherwise modifying the test piece. A second feature of the perspex model is its row of film-cooling discharges. The film holes have a diameter $D_{fc} = 0.5\,D_{jet}$, are positioned midway between successive impingement jets, and are inclined at $\beta_{fc} = 45°$ in a staggered pattern that surrounds each impingement jet with three film holes. Although the external film-cooling heat transfer is not measured in [8], the holes themselves substantially affect the internal flow field and therefore the internal-side Nusselt-number distribution. All film-cooling outlets feed into a single common outlet plenum, from which two suction lines—one on the top, one on the bottom—remove the spent air; with both line valves fully open, the mass flows extracted on the two sides are essentially equal, and the pressure field around the model is correspondingly symmetric.

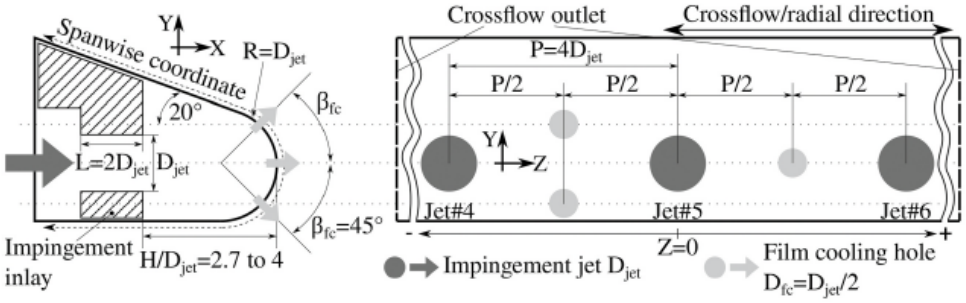

Figure 5.2 : Leading-edge geometry of the perspex test model of Forster and Weigand [8].

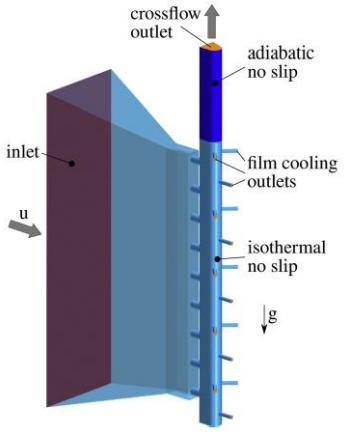

Figure 5.3 : Geometry of numerical model used by Forster and Weigand [8].

5.1.3 Crossflow configurations and test matrix

What sets the rig of Forster and Weigand [8] apart from earlier impingement test sections is the deliberate, mechanically adjustable level of internal crossflow that it permits. The spent jet air, after striking the target, has to evacuate the cavity through two routes: the film-cooling holes that pierce the target wall, and two lateral (spanwise) ports that open at the two ends of the impingement array. Closing zero, one, or both of these lateral ports with mountable lids therefore yields three discrete crossflow regimes, sketched in Figure 5.4:

- a zero-crossflow regime, with both lateral lids removed so that the discharged air leaves symmetrically through both ends of the array and the streamwise component of velocity inside the cavity is negligible;
- an intermediate-crossflow regime, with one of the two lids in place so that all lateral discharge is funneled through the remaining open side, generating a moderate but appreciable streamwise crossflow over the target plate;

• a maximum-crossflow regime, with both lids fitted so that the only available exit for the spent fluid is through the film-cooling holes, which leaves the array fully embedded in the strongest crossflow that the apparatus can produce.

The three regimes are intended to mimic conditions found at different chordwise stations along an actual cooled airfoil—approximately the hub (no crossflow), the mid-span (intermediate crossflow), and the tip (maximum crossflow). For each regime two values of the standoff ratio (H/D_{jet} = 2.7 and H/D_{jet} = 4) were probed, and the jet Reynolds number was kept at the single value Re_D = 30 000. In total, this yields six experimental operating points [8].

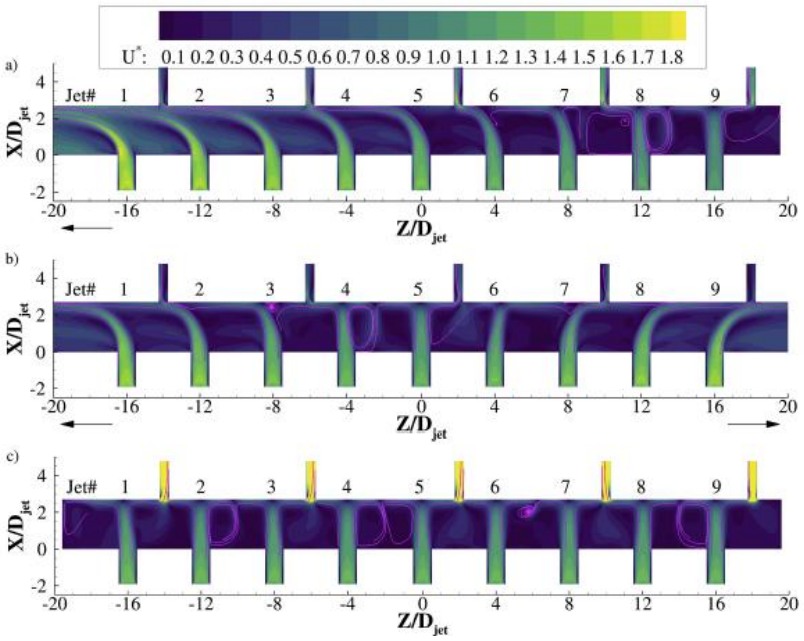

Figure 5.4 : Three crossflow configurations realized by closing one, both, or zero lateral lids of the outlet plenum [8].

5.1.4 Heat-transfer measurement technique

To obtain the local heat-transfer coefficients on the concave inner surface, Forster and Weigand [8] employed the transient Thermochromic Liquid Crystal (TLC) technique. The principle of the technique exploits the fact that the colour reflected by a liquid-crystal layer depends in a reproducible way on its instantaneous temperature; once the colour–temperature relationship is known from a calibration step, the temperature at any point on the coated surface can be deduced by reading the colour from a single pixel of the recorded video. In [8] the inner perspex wall was sprayed with a narrow-bandwidth TLC formulation (band-width of approximately 1 K) and then coated with a layer of black paint; the latter serves as an opaque background that improves the

contrast of the colour signal as seen by the camera. Both layers are thin enough that their thermal resistance and thermal capacity can be ignored when the data are reduced. Each TLC batch was calibrated prior to its first use, the calibration yielding the indication temperature T_{ind}, defined as the temperature at which the green channel of the camera output reaches its maximum brightness for that specific mixture.

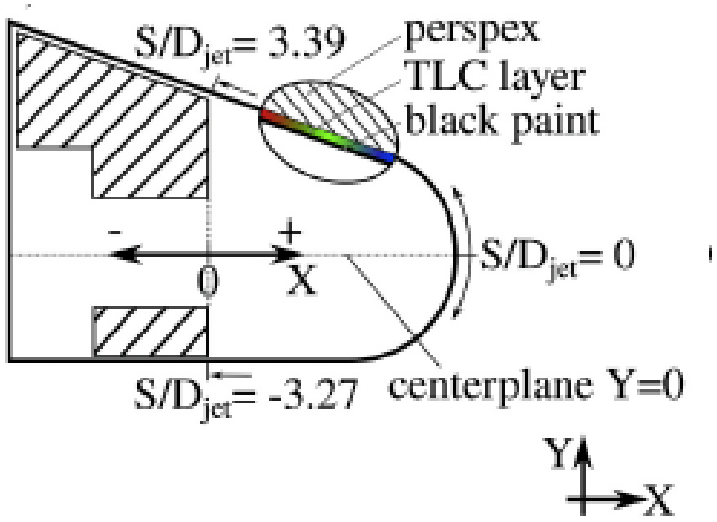

Figure 5.5 : Transient TLC measurement principle [8].

Figure 5.5 depicts how the transient measurement is realized in practice. Before each run the perspex model sits at a uniform initial temperature T_0. At t = 0 the mesh heater is energized, and the flow temperature jumps almost stepwise to its operating value Tref. From this moment onwards, heat is convected from the heated stream to the inner wall, and the wall temperature climbs gradually as energy diffuses into the solid perspex. The wall-temperature history is captured by the camera; for every pixel one then extracts the indication time tind, defined as the elapsed time at which the local wall temperature first reaches Tind. Because a high local convective coefficient pumps energy into the wall faster, regions of strong heat transfer reach Tind earlier (small tind), whereas weakly cooled regions reach it later (large tind). The reduction from tind to the local heat-transfer coefficient h is then performed by treating the wall as a one-dimensional semi-infinite solid—with the standard analytical solution and a Buttsworth–Jones curvature correction applied wherever the wall is curved—and by inserting the calibrated material properties of perspex. The local Nusselt number follows immediately as $Nu = h D_{jet} / k$. The uncertainty analysis carried out in [8] places the worst-case error in Nu at about 10 %, with an additional uncertainty in the Reynolds number of less than 2 %.

5.2 Literature-Based CFD Model

Having defined the validation case in Section 5.1, this section now specifies the CFD model used to simulate it. The numerical setup is built closely on that of Forster and Weigand [8], so that any deviation between the present prediction and the measurements of [8] can be attributed to the modelling choices themselves rather than to differences in the imposed boundary conditions, the mesh strategy, or the discretization. Only the choice of CFD code distinguishes the present work from [8] — Ansys Fluent [31] is used here in place of OpenFOAM v7. The four sub-sections that follow document, in turn, the geometry and mesh (Section 5.2.1), the definitions of the non-dimensional groups used in the validation comparison (Section 5.2.2), the inlet, outlet, and wall boundary conditions (Section 5.2.3) and the solver settings (Section 5.2.4).

5.2.1 Geometry, mesh generation and mesh-independency

In the present numerical study, the experimentally validated geometry proposed by Forster and Weigand [8] is adopted as the baseline to investigate impingement cooling performance in a generic gas turbine blade leading edge under high crossflow conditions. The objective is to examine the influence of crossflow on local heat transfer distributions over a concave surface representative of turbine blade internal leading-edge cavities.

The computational domain consists of a concave target surface with constant curvature, emulating the internal leading-edge geometry of a turbine blade. An array of nine circular impingement jets with diameter D discharges perpendicularly toward the concave surface, consistent with the reference configuration. The details of the leading-edge geometry and the jet-to-surface spacing are illustrated in Figure 5.6. All geometric dimensions are normalized using the jet diameter to allow direct comparison with the reference study and existing literature. In the present parametric investigation, only the jet-to-jet pitch P and the jet-to-surface distance H are varied as geometric parameters. Consequently, the impingement jet diameter D, film-cooling hole diameter d, leading-edge radius R, and jet length L are held constant throughout the study.

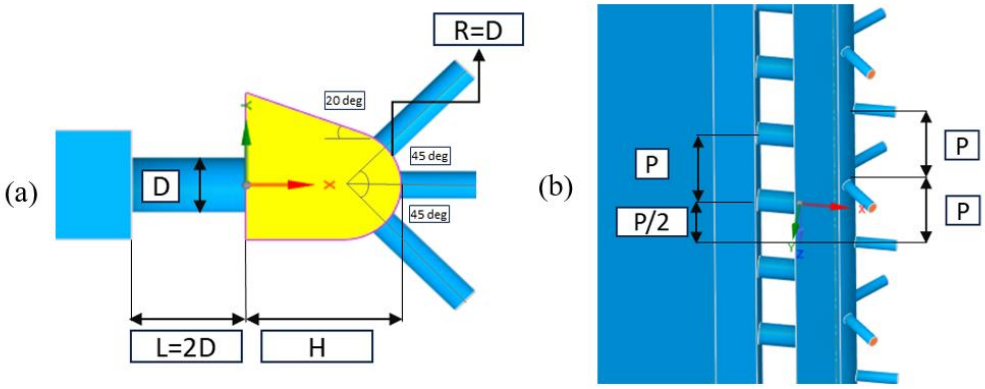

Figure 5.6 : Geometry of the present study: a) Leading-edge geometry, b) Spacing for impingement jet and film holes.

All computational grids used in the present work were built within the Ansys Fluent Meshing environment. A hybrid unstructured topology was adopted: polyhedral cells dominate the bulk of the fluid volume, while a structured layer of prism elements is grown from every solid boundary so that the steep velocity and temperature gradients within the boundary layer can be properly captured. Two regions received additional local refinement: the immediate vicinity of each jet exit, where the developing shear layers must be well resolved, and the impingement target itself, where the stagnation-zone heat-transfer signature is concentrated. A representative section of the resulting mesh is shown in Figure 5.7.

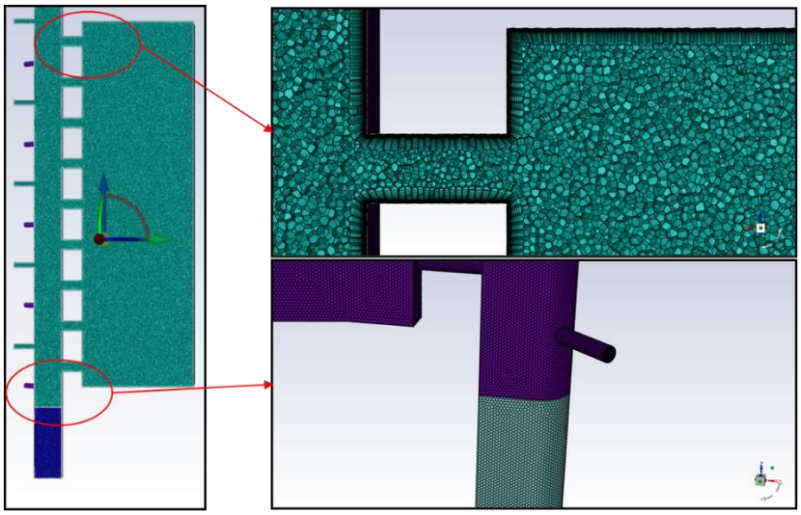

Figure 5.7 : Detail of the hybrid mesh used in the simulations.

Because the k–ω SST closure is intended to be integrated through the viscous sublayer rather than relying on wall functions, the height of the first prism cell at every solid boundary was tuned to keep the dimensionless wall distance below unity ($y^+ \lesssim 1$) throughout the domain. The sensitivity of the numerical solution to the computational

grid was assessed by progressively refining the mesh from level L1 to level L5. For each mesh, the total number of cells N and its reciprocal 1/N were recorded together with the area-averaged Nusselt number. To facilitate comparison, the average Nusselt number of every mesh was normalized by the value obtained on the reference mesh L4, as reported in Table 5.1. The selected validation case, for the mesh independence study, represents the maximum-crossflow condition reported in reference [8], with operating and geometric parameters of Re_D = 30 000, H/D = 2.7, and P/D = 4.

Table 5.1 : Grid independence data: mesh size N, its reciprocal 1/N, and the average Nusselt number normalized by the L4 value.

Mesh level	N (mesh size)	1/N	Nu_{ave} / $Nu_{ave,L4}$
L1	3.90×10^{6}	2.57×10^{-7}	0.959
L2	5.10×10^{6}	1.96×10^{-7}	0.984
L3	7.10×10^{6}	1.41×10^{-7}	0.995
L4	1.01×10^{7}	9.90×10^{-8}	1.000
L5	1.41×10^{7}	7.10×10^{-8}	1.001

As the grid is refined, the inverse mesh size 1/N decreases and the normalized Nusselt number approaches unity, indicating convergence towards a grid independent solution. Variation of the normalized average Nusselt number with the inverse mesh size 1/N is illustrated in Figure 5.8. The relative change between the two finest meshes, L4 and L5, is approximately 0.1%, confirming that further refinement beyond L4 does not produce a significant change in the predicted heat transfer. Consequently, mesh L4 was adopted for the remainder of the study.

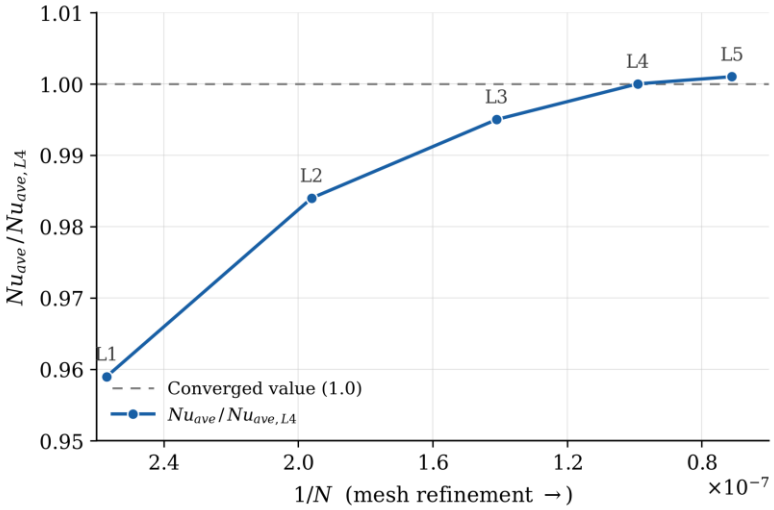

Figure 5.8 : Variation of the normalized average Nusselt number Nu_{ave} / $Nu_{ave,L4}$ with the inverse mesh size 1/N for meshes L1–L5.

In addition to grid independence, the quality of the selected mesh L4 was verified against standard mesh metrics. A boundary-layer inflation mesh comprising 24 layers with a first-layer thickness of 4 μm was applied to adequately resolve the near-wall gradients. The maximum cell aspect ratio and maximum skewness were 88.4 and 0.79, respectively, which are within acceptable limits for the present finite-volume solver. The mesh quality parameters for L4 are summarized in Table 5.2.

Table 5.2 : Mesh quality metrics for the selected reference mesh L4.

First layer thickness	Inflation layers	Max. aspect ratio	Max. skewness
4 μm	24	88.4	0.79

Based on the grid independence results and the mesh quality assessment, the L4 mesh is adopted for all cases considered in this study, as it is deemed adequate to satisfy the required mesh quality criteria while providing a grid independent solution at a reasonable computational cost.

5.2.2 Definition of the Reynolds and Nusselt numbers

The impingement target surface is treated as a constant heat-flux boundary, in line with the experimental procedure of Forster and Weigand [8]. The two non-dimensional groups used to express the validation and parametric data are defined as follows. The jet Reynolds number is built from the impingement-jet diameter,

$$Re_D = \frac{\rho u D}{\mu} = \frac{4\dot{m}}{\pi D \mu} \tag{5.1}$$

In Equation (5.1), ρ denotes the fluid density, u the mean axial jet velocity, D the jet diameter, and μ the dynamic viscosity of air; in principle each property could be evaluated locally at the cross-section of any individual jet, but in the present work all four are computed once for the array as a whole using the total inlet mass-flow rate ṁ given on the right-hand side of Equation (5.1). The mean per-jet mass-flow rate is then ṁ/9, since the nine jets share the manifold equally. The local Nusselt number is constructed from the heat-transfer coefficient h and the same length scale D as

$$Nu = \frac{hD}{k} \tag{5.2}$$

with k the thermal conductivity of the working fluid (air). The convective coefficient h is in turn extracted from the CFD solution by means of the surface-energy balance at the wall,

$$h = \frac{-k\left(\frac{\partial T}{\partial n}\right)_{wall}}{T_w - T_{ref}} \tag{5.3}$$

in which T_w is the wall temperature, T_{ref} is a reference fluid temperature, and the numerator on the right-hand side is the local conductive heat flux into the wall (i.e. the surface heat flux). As in [8], Tref is computed as the cross-sectionally averaged total temperature taken at the center of the nine impingement jet nozzles. The surface heat fluxes themselves are obtained directly from the converged CFD field, after which Equation (5.3) gives h pointwise and Equation (5.2) yields the local Nu.

5.2.3 Boundary conditions

The reference data used for validation were taken from the experiments of Forster and Weigand [8]. The chosen comparison case corresponds to the maximum-crossflow configuration of [8] and is parameterized by Re_D = 30 000, H/D = 2.7 & 4 and P/D = 4. At the inlet of the computational domain, a mass-flow-rate boundary condition is applied; the prescribed mass-flow value is the one that yields the desired jet Reynolds number, and the inlet stream is given a total temperature of 320 K together with a turbulence intensity of 10 % (with the turbulence length scale built from the local hydraulic diameter). At the downstream end of the model, a pressure-outlet condition fixes the static pressure at 101.325 kPa, replicating the homogeneous level seen experimentally in the outlet plenum. Every solid surface is treated as a no-slip wall; the concave impingement target is additionally constrained to the isothermal value T_w = 298.15 K. To keep recirculation from spuriously crossing the outlet plane, the pressure-outlet boundary is shifted artificially downstream by means of a short adiabatic-walled extension that is appended to the geometry. The full set of boundary types and values is summarized graphically in Figure 5.9.

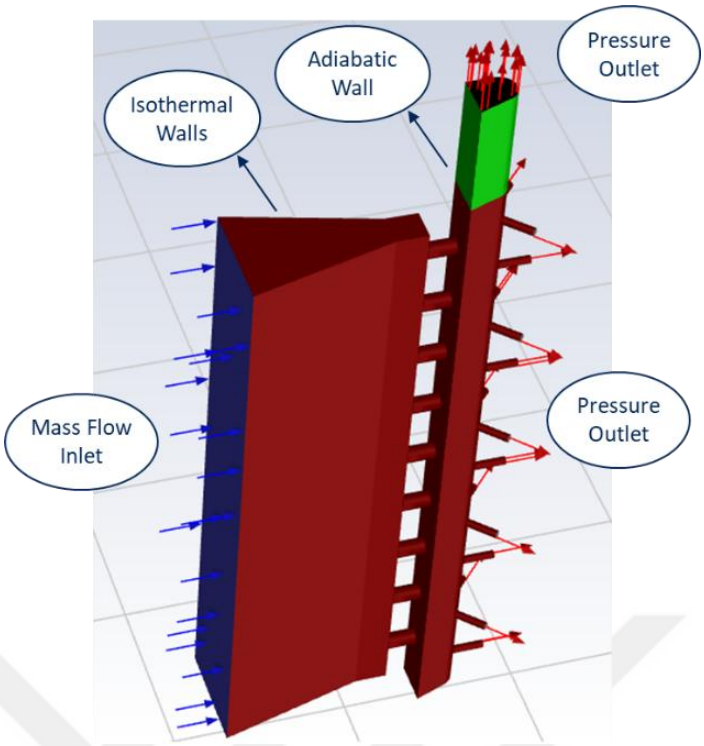

Figure 5.9 : Computational domain and boundary conditions used in the present simulations.

5.2.4 Solver settings and convergence check

All simulations were carried out using the three-dimensional pressure-based solver in ANSYS Fluent, with the energy equation switched on. Gravity is included along the positive z direction. Closure of the Reynolds-stress and turbulent-heat-flux terms is provided by the k–ω Shear Stress Transport model, whose suitability for problems featuring impingement, near-wall separation, and strong jet–crossflow coupling has already been documented in Section 4.4.

For the convective fluxes appearing in the momentum, turbulence, and energy equations, second-order upwind discretization was selected so as to reduce the leading-order numerical diffusion. The pressure–velocity coupling is handled by the Coupled algorithm, which solves the continuity and momentum systems implicitly in a single block and is generally more robust than the segregated SIMPLE-family schemes for steady impingement flows of the present type.

A five-level multigrid initialization procedure was applied at the beginning of the simulations to promote faster convergence and improve numerical stability during the early stages of the solution process. For the initial 300 iterations, the calculations were performed using a global automatic time-step formulation in order to facilitate stable

flow-field development and rapid residual reduction. After this phase, the simulations were continued with a fixed Courant–Friedrichs–Lewy (CFL) number of 1 throughout the remaining iterations to maintain stable convergence behavior and consistent temporal advancement of the solution. For all investigated cases, a minimum of 1600 total iterations was performed to ensure adequate convergence of the flow and thermal fields.

The run is declared converged only when two complementary criteria are met simultaneously: the scaled residuals fall below 10^{-5} for continuity and momentum, almost below 10^{-4} for the turbulence quantities, and below 10^{-6} for the energy equation; and the integral monitor variables, surface-averaged Nu on the target wall and the jet Reynolds number Re_D, each reach a steady plateau. Considering the previously described iteration procedure and convergence criteria, the convergence history of the scaled residuals corresponding to the case of Re_D=30,000, H/D=2.7, and P/D=4 is presented in Figure 5.10 as an example.

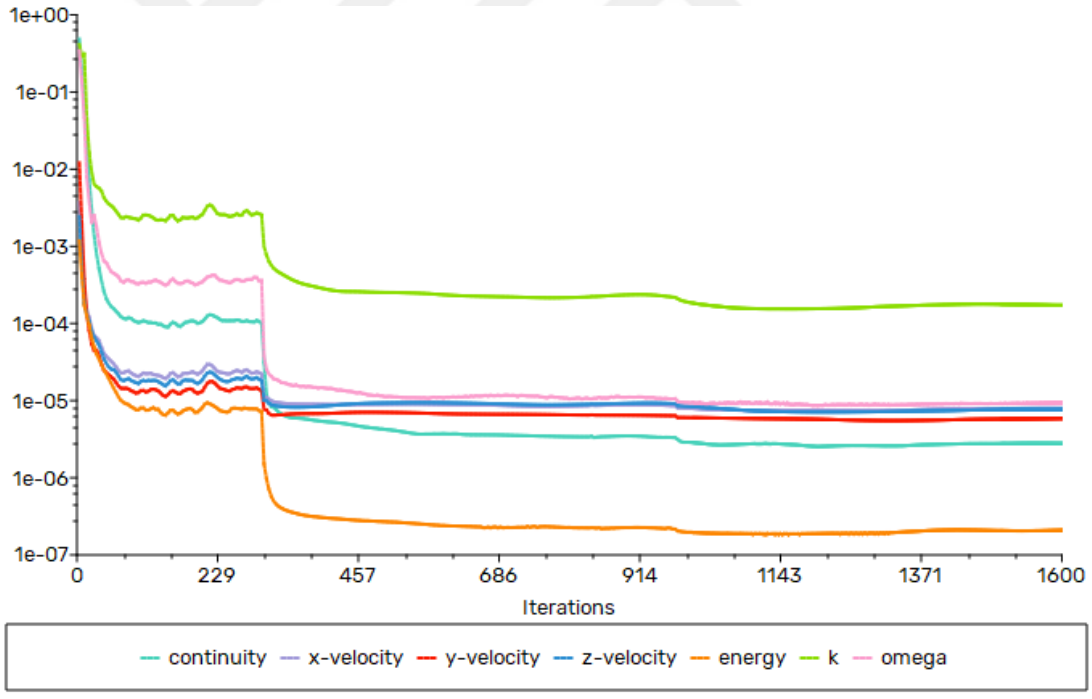

Figure 5.10 : Convergence history of scaled residuals for Re_D = 30 000, H/D = 2.7, P/D = 4.

In a similar manner, the monitored jet Reynolds number is plotted as a function of iteration count in Figure 5.11 to provide additional verification of the convergence characteristics of the numerical solution.

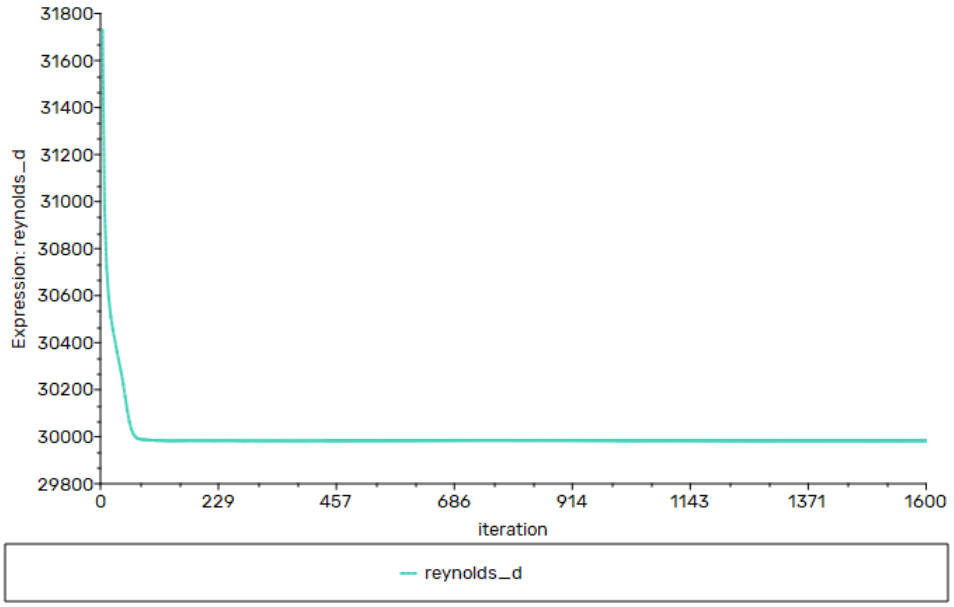

Figure 5.11 : Convergence history of jet Reynolds number for Re_D = 30 000, H/D = 2.7, P/D = 4.

Additionally, the iterative evolution of the surface-averaged Nusselt number over the leading-edge surface is illustrated in Figure 5.12 to provide further confirmation of the convergence characteristics associated with the thermal solution.

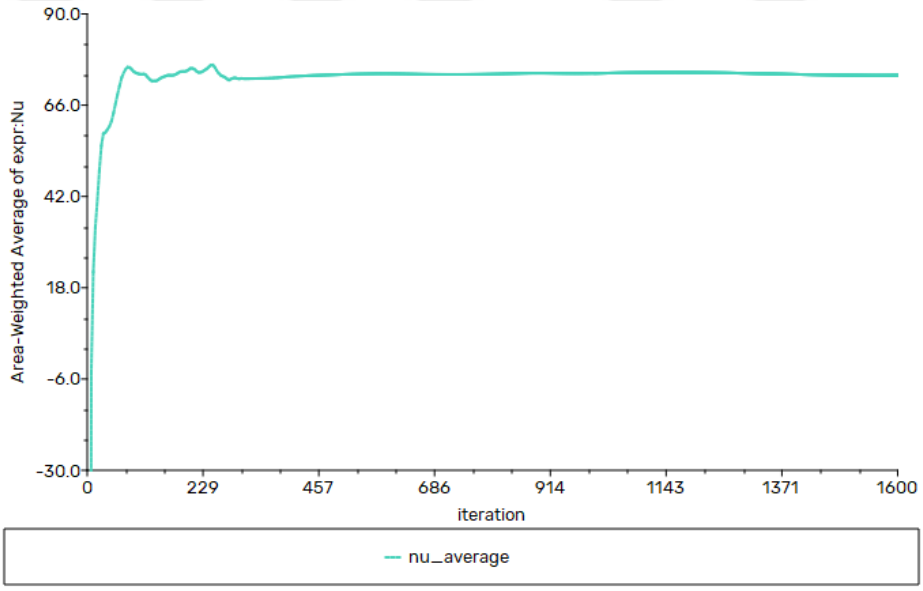

Figure 5.12 : Convergence history of surface-averaged Nusselt number for Re_D = 30 000, H/D = 2.7, P/D = 4.

5.3 Literature Validation Results

For validation purposes, the numerical methodology was compared against the experimental data of Forster and Weigand [8] for two representative maximum-

crossflow configurations. The first validation case (Case 1) corresponds to Re_D=30000, H/D=2.7, and P/D=4, whereas the second validation case (Case 2) is defined by Re_D=30000, H/D=4.0, and P/D=4. Prior to the heat-transfer comparisons, the near-wall mesh quality was evaluated through wall y+ distributions to ensure adequate resolution of the viscous sublayer and boundary-layer behavior.

Figure 5.13 presents the wall y+ distributions obtained for Case 1. The contour over the entire computational domain is illustrated in Figure 5.13(a), while the detailed wall y+ distribution on the leading-edge target surface, which constitutes the principal region of interest in the present heat-transfer investigation, is shown in Figure 5.13(b). The maximum wall y+ value within the overall computational domain was approximately 1.73, whereas the maximum y+ value on the leading-edge surface remained below 0.85. These results indicate that the near-wall mesh resolution was sufficiently refined to accurately resolve the viscous sublayer and capture the associated flow and thermal transport mechanisms.

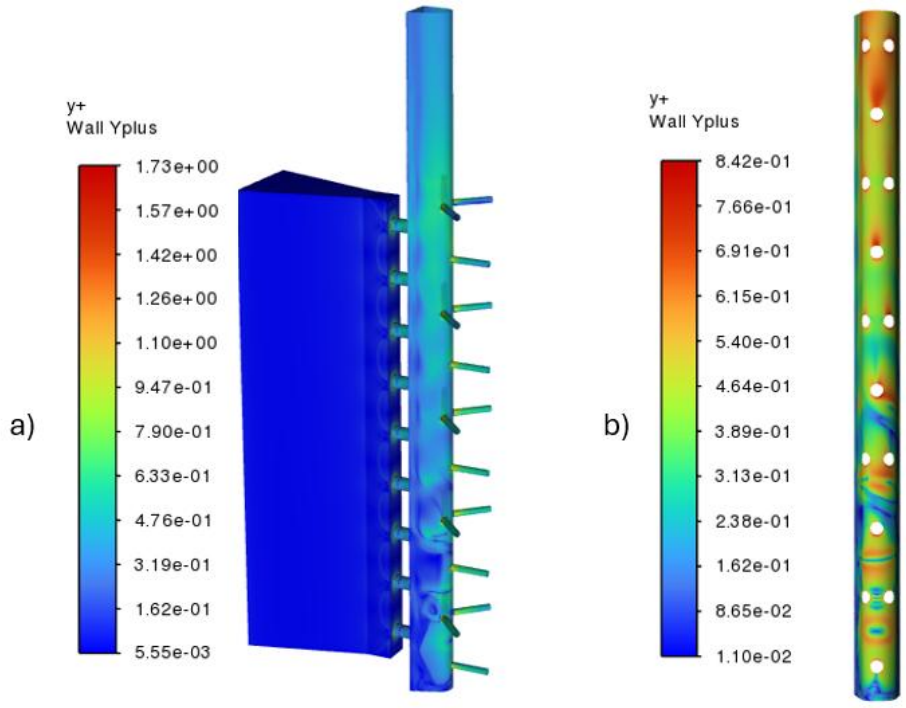

Figure 5.13 : y+ contours for Case 1: a) whole domain, b) leading-edge.

Similarly, Figure 5.14 illustrates the wall y+ contours obtained for Case 2. The overall wall y+ distribution throughout the computational domain is presented in Figure 5.14(a), whereas the detailed contour on the leading-edge target surface is shown in Figure 5.14(b). For this configuration, the maximum wall y+ value within the entire

computational domain was approximately 1.54, while the maximum value on the leading-edge surface remained below 0.77. The obtained y+ levels confirm that the mesh system provided sufficient near-wall refinement for accurate prediction of the boundary-layer development and heat-transfer characteristics under the investigated maximum-crossflow condition.

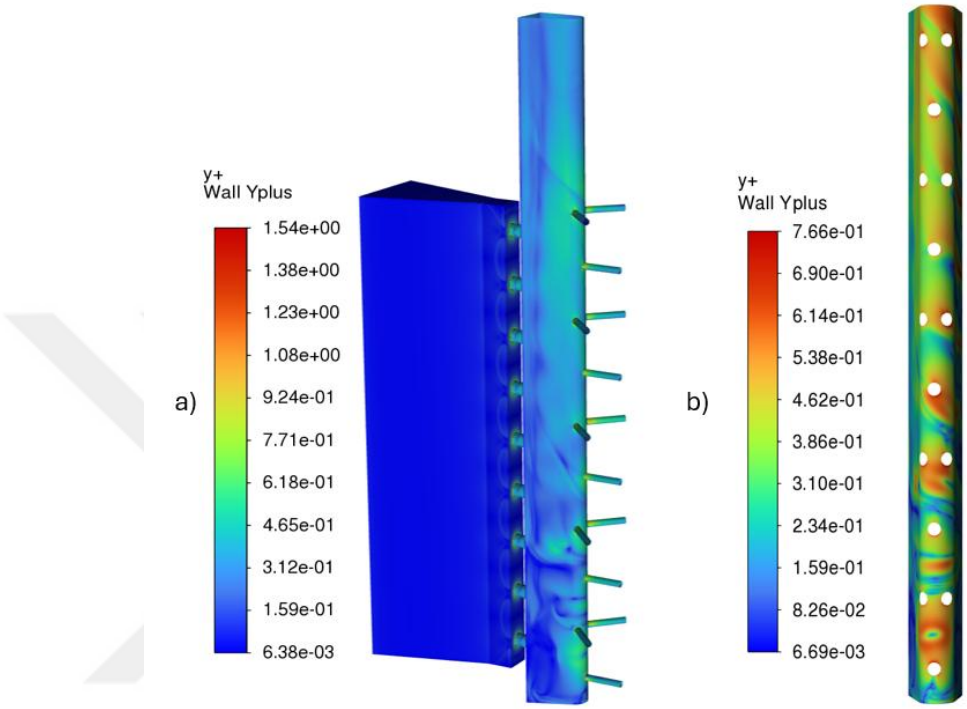

Figure 5.14 : y+ contours for Case 2: a) whole domain, b) leading-edge.

Overall, the low wall y+ values achieved for both validation cases demonstrate the adequacy of the generated mesh structure for resolving near-wall flow physics and performing reliable numerical heat-transfer simulations.

Figure 5.15 illustrates the leading-edge target surface considered in the present validation study. The primary region of interest for the heat-transfer analysis corresponds to the leading-edge surface highlighted in green. Consistent with the experimental methodology of Forster and Weigand [8], localized regions surrounding the film-cooling holes were excluded from the evaluation procedure to eliminate the direct influence of the hole geometry on the local heat-transfer measurements. These excluded regions are indicated in pink in the figure, and each excluded area was defined with a diameter of 1.5 D_{fc}, where D_{fc} represents the film-cooling-hole diameter.

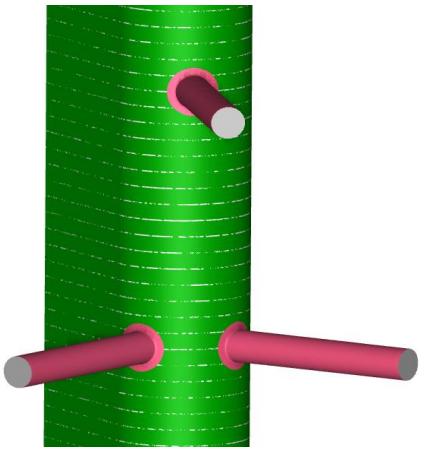

Figure 5.15 : Leading-edge data sampling locations and excluded regions.

In addition, the validation process involved the comparison of spanwise local Nusselt number distributions obtained along thin sampling surfaces extending circumferentially over the leading-edge region. These sampling locations, which effectively behave as line-like extraction surfaces for post-processing purposes, are represented by the white lines shown in Figure 5.15.

Figure 5.16 presents the comparison of the spanwise local Nusselt number distribution obtained for Case 1 between the experimental measurements of Forster and Weigand [8] and the present CFD results. The distribution is plotted along the spanwise direction in terms of Z/D_{jet} under the maximum-crossflow condition corresponding to Re_D=30000, H/D=2.7, and P/D=4.

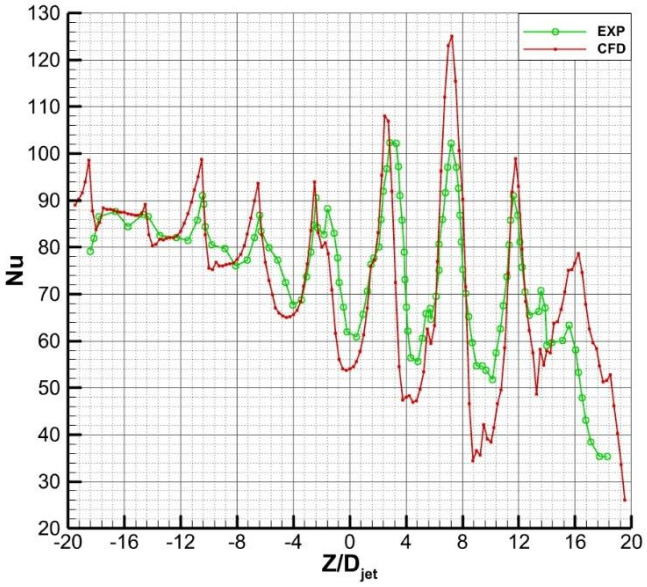

Figure 5.16 : Case 1 CFD vs. experiment [8] local Nusselt number distribution.

Figure 5.17 illustrates the comparison of the spanwise local Nusselt number distribution obtained for Case 2 between the experimental measurements of Forster and Weigand [8] and the present CFD predictions. The comparison corresponds to the maximum-crossflow configuration defined by Re_D=30000, H/D=4.0, and P/D=4.

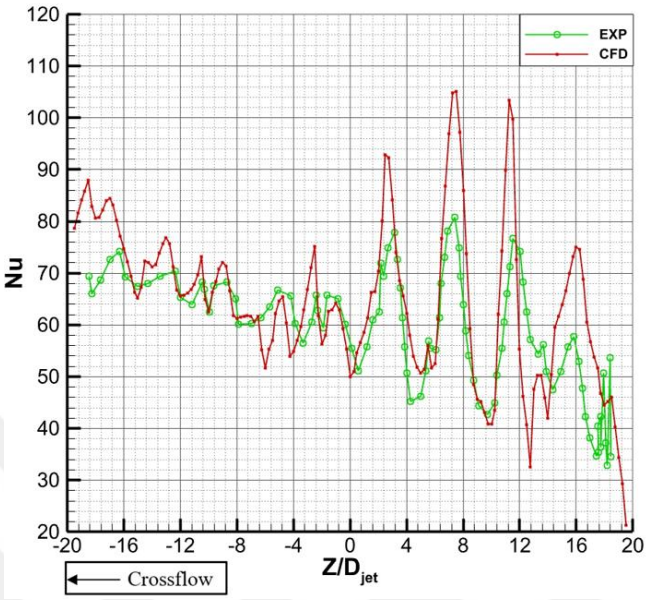

Figure 5.17 : Case 2 CFD vs. experiment [8] local Nusselt number distribution.

The numerical results demonstrate good overall agreement with the experimental data and successfully capture the principal heat-transfer trends, including the major peak and valley regions along the spanwise direction. Although certain deviations are observed in regions subjected to strong jet–crossflow interaction, the CFD model accurately reproduces the dominant thermal behavior over the leading-edge surface. These discrepancies are primarily associated with the highly three-dimensional and locally unsteady flow structures developing within the impingement region.

Table 5.3 compares the experimental area-averaged Nusselt number reported in [8] with the corresponding line- and area-averaged values extracted from the present CFD. For Case 1 the CFD area average underpredicts the experiment by about 2.4%, whereas for Case 2 it overpredicts by approximately 6.2%, with the line-averaged values following the same trend within 0.3 percentage points in both cases. Since the area-averaged definition integrates the local Nusselt distribution over the entire impinged surface, the CFD area-averaged Nusselt number is adopted as the reference Nu in the parametric study of the following chapters

Table 5.3 : CFD vs. experiment [8] area average Nusselt number.

Case Number	Experiment Area Average Nu	CFD Line Average Nu	CFD Area Average Nu
Case 1	74.7	73.1	72.9
Case 2	60.9	64.9	64.7

Finally, a visual comparison is provided in Figures 5.18 and 5.19: Figure 5.18 reproduces the CFD result of Forster and Weigand (2021), while Figure 5.19 shows the corresponding contour obtained from the present CFD. The comparison is performed in terms of the non-dimensional velocity U*, defined as the ratio of the local velocity to the area-averaged jet velocity used in the definition of Re_D.

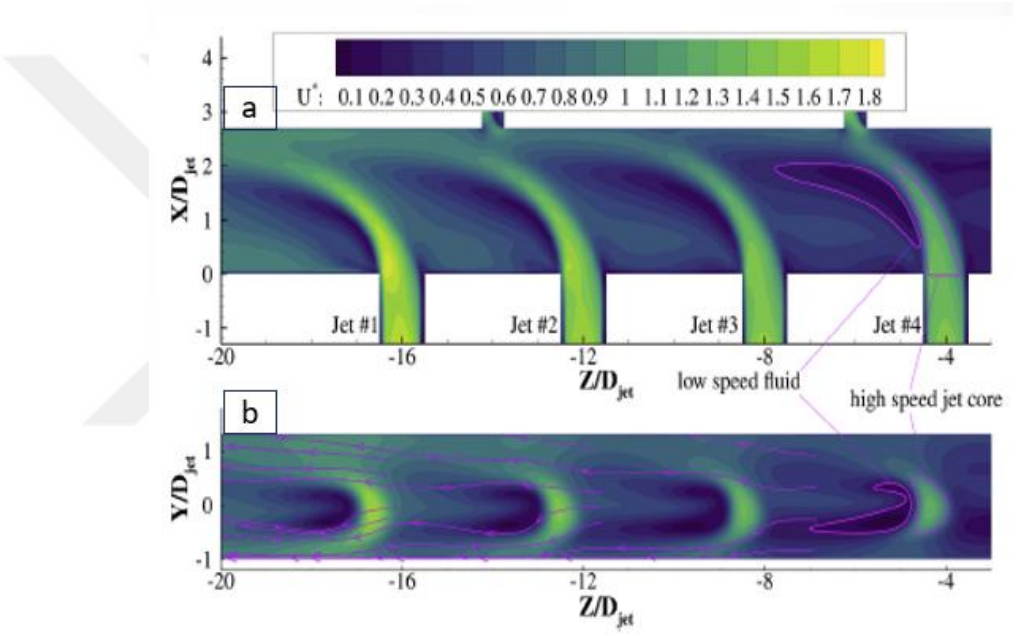

Figure 5.18 : Non-dimensional velocity contours from Forster and Weigand [8]: a) Center plane (Y=0), b) $X/D_{jet}=1$.

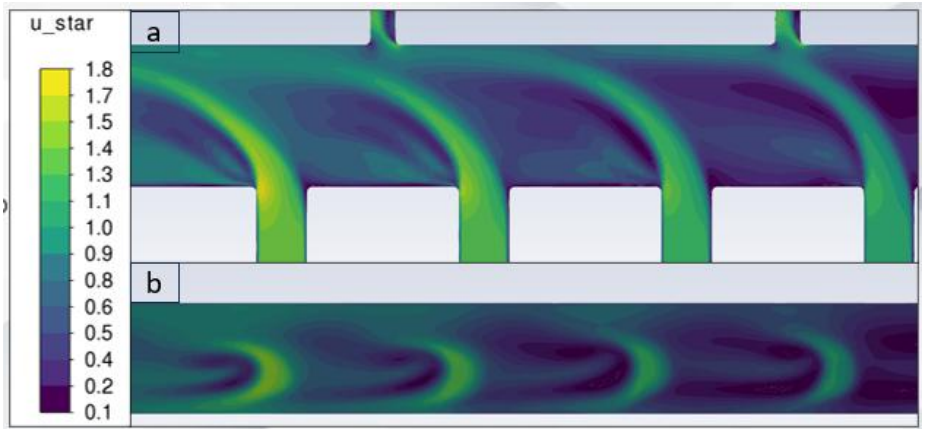

Figure 5.19 : Non-dimensional velocity contours of the present study: a) Center plane (Y=0), b) X/Djet=1.

6. CFD SIMULATIONS FOR CORRELATION

The numerical methodology described in detail in Section 5.2—including the polyhedral-dominant mesh with prism layers (Section 5.2.1), the boundary conditions (Section 5.2.2), the pressure-based steady-state solver with the k–ω SST turbulence model (Section 5.2.3), and the definitions of the jet Reynolds number and the Nusselt number (Section 5.2.4)—was applied identically across the entire parametric campaign of the present thesis. The mesh sizing strategy, the $y^+ \lesssim 1$ requirement, the inlet/outlet/wall boundary types, the inlet temperature of 320 K, the wall temperature of 298.15 K, the outlet static pressure of 101.325 kPa, the turbulence intensity of 10 %, the second-order upwind discretization, the Coupled pressure–velocity algorithm, and the residual-reduction convergence criteria were all kept exactly as described in Section 5.2 and are therefore not repeated here.

6.1 Methodology

The parametric campaign covers a three-dimensional design space spanned by the jet Reynolds number Re_D, the jet-to-surface spacing ratio H/D, and the jet-to-jet pitch ratio P/D. Each parameter varies at four discrete levels:

- the jet Reynolds number Re_D is varied as 10 000, 20 000, 30 000 and 40 000;
- the jet-to-surface spacing ratio H/D takes the values 1.4, 2.7, 4.0 and 5.3;
- the jet-to-jet pitch ratio P/D takes the values 2, 4, 6 and 8.

These ranges are chosen to span the practical design window of leading-edge impingement-cooling configurations encountered in modern gas-turbine blades, and to extend beyond the parameter ranges covered by the validation reference of Forster and Weigand [8] in order to support the development of an engineering correlation. The full Cartesian product of the three parameters yields $4 \times 4 \times 4 = 64$ independent configurations, for each of which a separate steady-state CFD simulation has been performed.

As an illustrative example, Figure 6.1 visualizes the geometric variation of the jet-to-surface spacing ratio, H/D, showing how changes in the distance between the jet exit and the target surface are represented relative to the jet diameter.

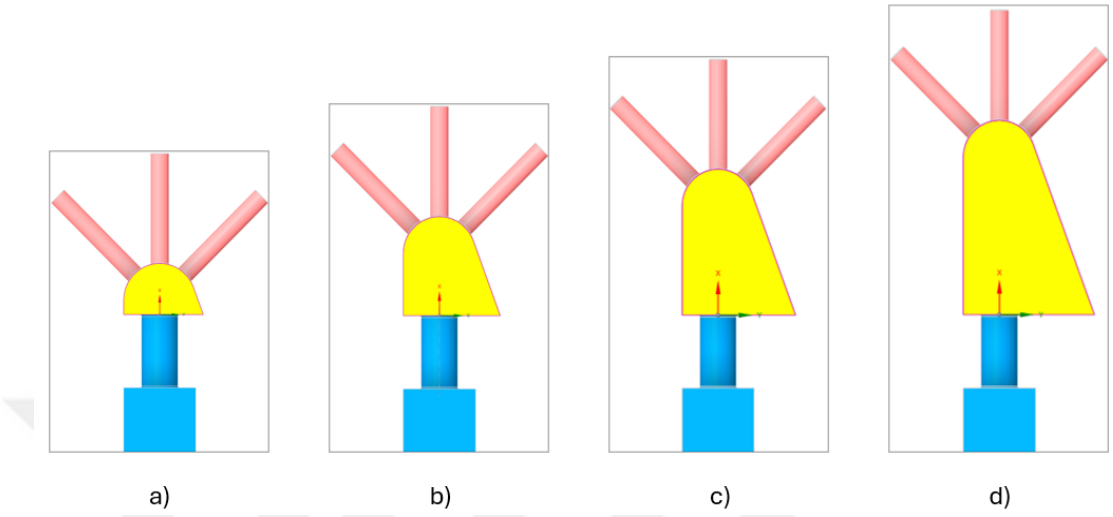

Figure 6.1 : Change of the domain for different H/D values: a) H/D=1.4, b) H/D=2.7, c) H/D=4.0, d) H/D=5.3.

Similarly, Figure 6.2 illustrates the geometric variation of the jet-to-jet pitch ratio, P/D, showing how the spacing between adjacent impingement jets changes relative to the jet diameter.

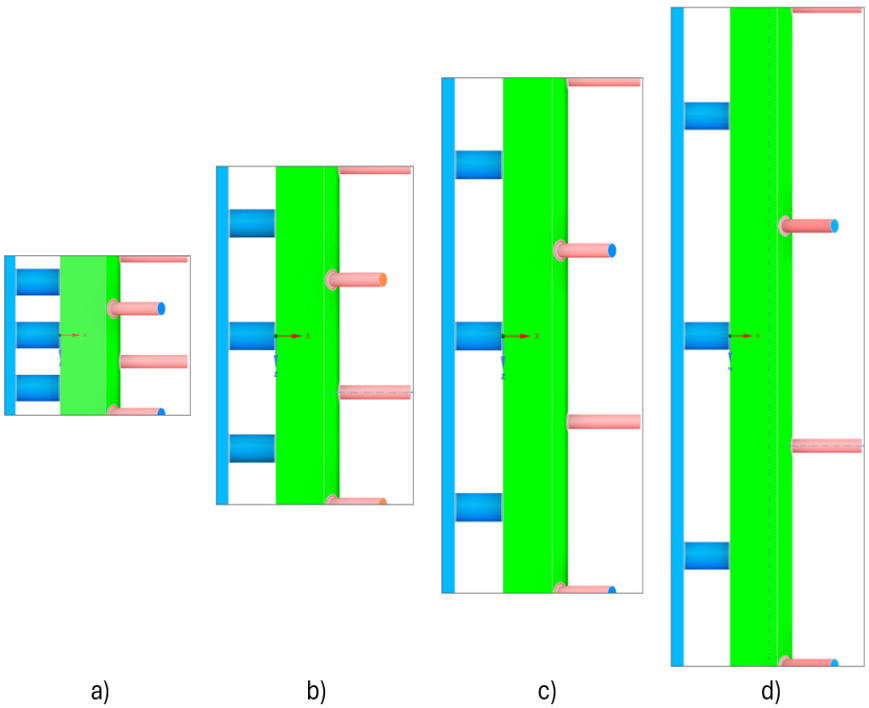

Figure 6.2 : Change of the domain for different P/D values: a) P/D=2, b) P/D=4, c) P/D=6, d) P/D=8.

For each parametric run, the jet Reynolds number is controlled solely by adjusting the imposed mass-flow rate at the inlet boundary, in accordance with Equation (5.1) of Section 5.2.4, while all other boundary conditions are kept identical to those of the validation case described in Section 5.2.2. The geometric parameters H and P are varied by exchanging the corresponding portion of the geometry, mirroring the way the impingement inlay was exchanged in the experimental setup of Forster and Weigand [8]. The crossflow intensity—here defined as the fraction of the inlet mass flow that exits through the streamwise crossflow outlet rather than through the film-cooling holes—is around 60 % across the entire parameter set, corresponding to the maximum-crossflow configuration of [8] but applied across all geometric and Reynolds-number variations of the present study. The case-by-case crossflow intensity varies slightly because the pressure losses are not identical across configurations, but this small variation is neglected in the analysis below.

6.2 Results and Correlation

The present chapter consolidates the parametric simulations into a discussion of how the surface-averaged Nusselt number on the impingement target responds to the three governing parameters of the study—the jet Reynolds number Re_D, the non-dimensional standoff H/D, and the non-dimensional inter-jet pitch P/D—all under the same prescribed level of internal crossflow. Throughout the campaign, the crossflow intensity (defined as the fraction of the total inlet mass flow that exits through the streamwise crossflow outlet rather than through the film-cooling holes) remains close to 60 %. Pressure-loss variations among configurations introduce small case-to-case fluctuations in this fraction, but the variation is sufficiently mild that it can be ignored without affecting the qualitative or quantitative trends discussed below. The 64 surface-averaged Nusselt numbers obtained from the CFD campaign are reported in Table 6.1, Table 6.2, Table 6.3 and Table 6.4. The tabulated results provide a systematic presentation of the heat-transfer performance obtained under this jet-to-surface spacing ratio, allowing a clear comparison of the effects of jet Reynolds number and jet-to-jet pitch ratio on the area-averaged thermal response of the target surface. To enhance readability, all 64 configurations were divided into four main tables according to their H/D values. Table 6.1 presents the results corresponding to H/D=1.4.

Table 6.1 : CFD surface-averaged Nusselt numbers for the H/D=1.4 configurations.

H/D	P/D	Re_D	Nu
1.4	2	10000	53.5
1.4	2	20000	88.9
1.4	2	30000	122.6
1.4	2	40000	152.5
1.4	4	10000	41.6
1.4	4	20000	73.1
1.4	4	30000	101.2
1.4	4	40000	128.3
1.4	6	10000	34.7
1.4	6	20000	61.7
1.4	6	30000	85.3
1.4	6	40000	110.1
1.4	8	10000	30.4
1.4	8	20000	54.0
1.4	8	30000	75.2
1.4	8	40000	97.4

Similarly, Table 6.2 summarizes the CFD-predicted surface-averaged Nusselt numbers for the configurations corresponding to H/D=2.7.

Table 6.2 : CFD surface-averaged Nusselt numbers for the H/D=2.7 configurations.

H/D	P/D	Re_D	Nu
2.7	2	10000	38.4
2.7	2	20000	68.0
2.7	2	30000	95.4
2.7	2	40000	120.1
2.7	4	10000	29.4
2.7	4	20000	52.6
2.7	4	30000	72.9
2.7	4	40000	93.4
2.7	6	10000	23.8
2.7	6	20000	43.9
2.7	6	30000	61.8
2.7	6	40000	80.0
2.7	8	10000	20.3
2.7	8	20000	36.9
2.7	8	30000	53.8
2.7	8	40000	68.4

In the same vein, Table 6.3 presents the CFD-derived surface-averaged Nusselt numbers for the configurations with H/D=4.0.

Table 6.3 : CFD surface-averaged Nusselt numbers for the H/D=4.0 configurations.

H/D	P/D	Re_D	Nu
4.0	2	10000	34.5
4.0	2	20000	60.7
4.0	2	30000	86.5
4.0	2	40000	107.4
4.0	4	10000	25.3
4.0	4	20000	46.6
4.0	4	30000	64.7
4.0	4	40000	85.2
4.0	6	10000	19.4
4.0	6	20000	35.7
4.0	6	30000	51.0
4.0	6	40000	66.7
4.0	8	10000	16.4
4.0	8	20000	30.2
4.0	8	30000	43.9
4.0	8	40000	55.8

Finally, the results for H/D=5.3 are presented in Table 6.4. Thus, all investigated configurations are systematically summarized.

Table 6.4 : CFD surface-averaged Nusselt numbers for the H/D=5.3 configurations.

H/D	P/D	Re_D	Nu
5.3	2	10000	30.9
5.3	2	20000	55.8
5.3	2	30000	76.3
5.3	2	40000	98.5
5.3	4	10000	22.2
5.3	4	20000	40.9
5.3	4	30000	57.7
5.3	4	40000	72.7
5.3	6	10000	17.4
5.3	6	20000	32.2
5.3	6	30000	45.9
5.3	6	40000	57.9
5.3	8	10000	14.4
5.3	8	20000	27.1
5.3	8	30000	39.1
5.3	8	40000	50.5

To compress the 64-point CFD data set into a single closed-form expression, a power-law ansatz was postulated for the dependence of Nu on the three governing parameters.

A non-linear least-squares regression was then performed on the full data, and the regression solver returned the coefficient and the three exponents that minimize the residual sum of squares between the CFD-predicted Nu values and those produced by the assumed functional form.

As a result of this curve-fitting procedure, the following empirical correlation was obtained:

$$Nu = 0.03424\, Re_D^{0.849} (H/D)^{-0.451} (P/D)^{-0.448} \tag{6.1}$$

The fidelity of the resulting correlation is most easily judged by plotting the values it predicts against the corresponding CFD values for every point in the data set; this comparison is presented in Figure 6.3. With only a few outliers, the cloud of points falls tightly along the 45° perfect-agreement line and stays well inside the ±10 % deviation bands. The visual impression therefore confirms that the assumed power-law form, calibrated as in Equation (6.1), reproduces the simulated dependence of Nu on the governing parameters across the full investigated range with engineering accuracy.

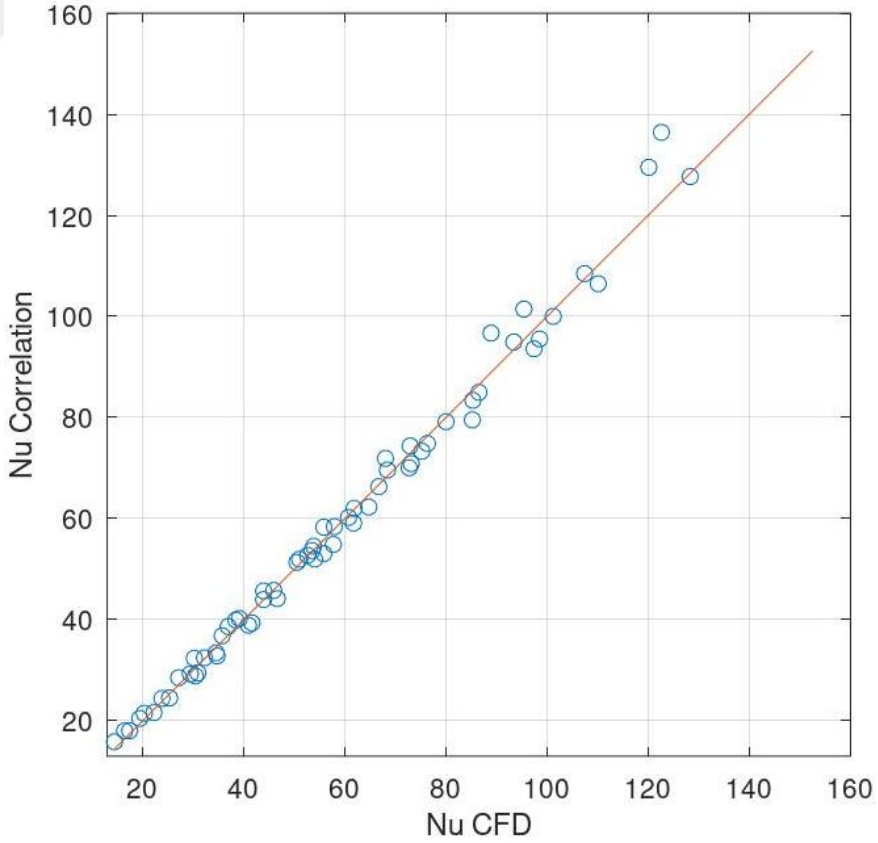

Figure 6.3 : Comparison of CFD data vs derived correlation.

For a quantitative measure of the fit quality, four standard error metrics—the coefficient of determination R^2, the mean absolute percentage error (MAPE), the mean absolute error (MAE), and the root mean square error (RMSE)—are reported in Table 6.5. The R^2 value of 0.983 indicates that the correlation explains nearly all of the variance in the CFD database, while the small numerical values of MAPE, MAE, and RMSE further confirm that the residual scatter is modest both in absolute and in relative terms. Taken together, these metrics support the conclusion that Equation (6.1) furnishes a statistically robust and physically reasonable engineering description of the high-crossflow impingement-cooling behaviour studied here.

Table 6.5 : Fit-quality parameters of the proposed correlation.

Fit-quality parameter	Value
R^2	0.983
MAPE	3.721 %
MAE	2.339
RMSE	4.059

6.3 Overall Heat-Transfer Characteristics

The 64-case data set shows that the area-averaged Nusselt number depends sensitively both on the jet Reynolds number and on the geometric ratios that fix the impingement layout, even when the cavity is operated under a strong, persistent crossflow. Across every geometry tested, raising Re_D from 10 000 to 40 000 produces a monotonic, near-linear growth of Nu, which underlines the central role played by jet inertia and the associated turbulence in driving the local convective transport. The simultaneous presence of a strong streamwise crossflow alters the classical free-impingement picture in several connected ways: the jets are bent downstream by the crossflow, the stagnation footprint is weakened, and the wall-jet shear-driven contribution becomes comparatively more important. Despite these compounded effects, the parameter dependence is sufficiently smooth and systematic across the campaign to be captured by the compact empirical relation given as Equation (6.1).

6.4 Effect of the Jet Reynolds Number

Among the three governing parameters, Re_D exerts the strongest control on the Nusselt number, a fact that is quantified by the dominant exponent 0.849 appearing in Equation

(6.1). The proximity of this exponent to unity tells us that, over the investigated range, the heat-transfer augmentation is driven primarily by inertial effects in the jet rather than by turbulent transport alone. Higher Re_D simultaneously deepens the jet penetration through the cavity and raises the turbulence level in the impingement region, both of which sharpen the near-wall velocity gradient and intensify the thermal mixing close to the target. A further mechanism becomes important under strong crossflow: a more energetic jet is more capable of penetrating the cross-stream and reaching the target with a trajectory close to the one it would follow in a quiescent environment, so the loss of impingement effectiveness due to deflection is partly mitigated as Re_D grows. These conclusions are consistent with the prior experimental and numerical literature on impingement under crossflow, which has long reported a Reynolds-number-dominated behaviour but with reduced absolute effectiveness compared with the no-crossflow case. The corresponding numerical evidence from the present campaign is summarized in Figure 6.4, where the surface-averaged Nu is plotted against Re_D at fixed P/D = 4 for the four examined values of H/D. Visual comparison of Nu contours for variable Re_D is given in Figure 6.5 for the same geometric configurations.

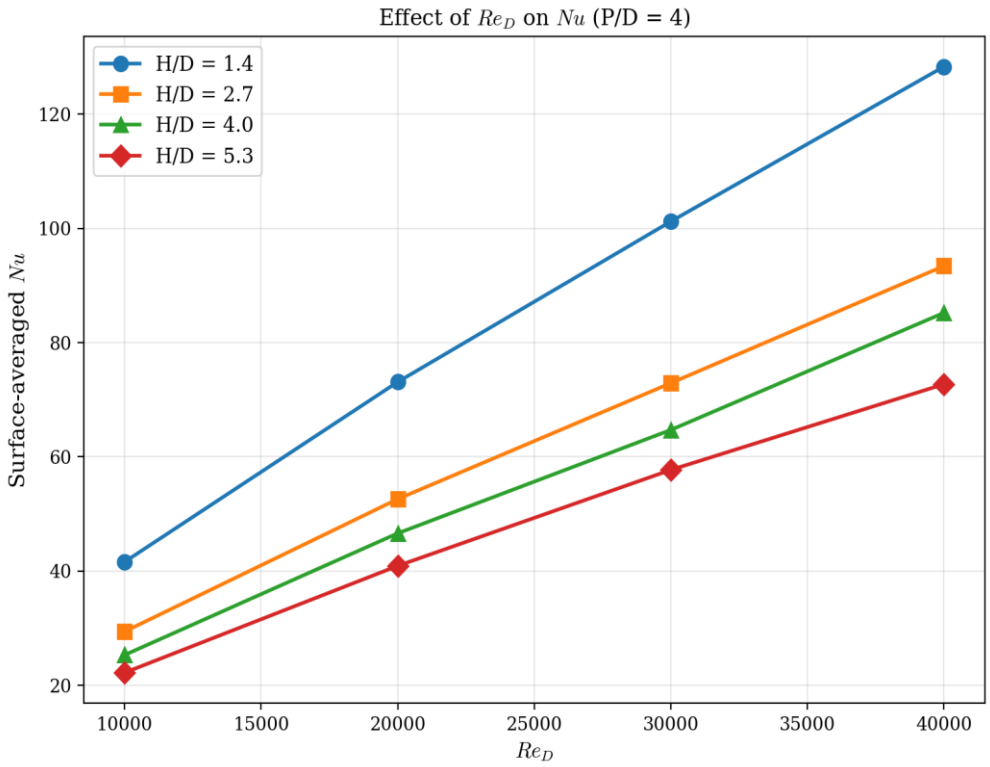

Figure 6.4 : Effect of the jet Reynolds number Re_D on the surface-averaged Nusselt number for fixed P/D = 4 and varying H/D.

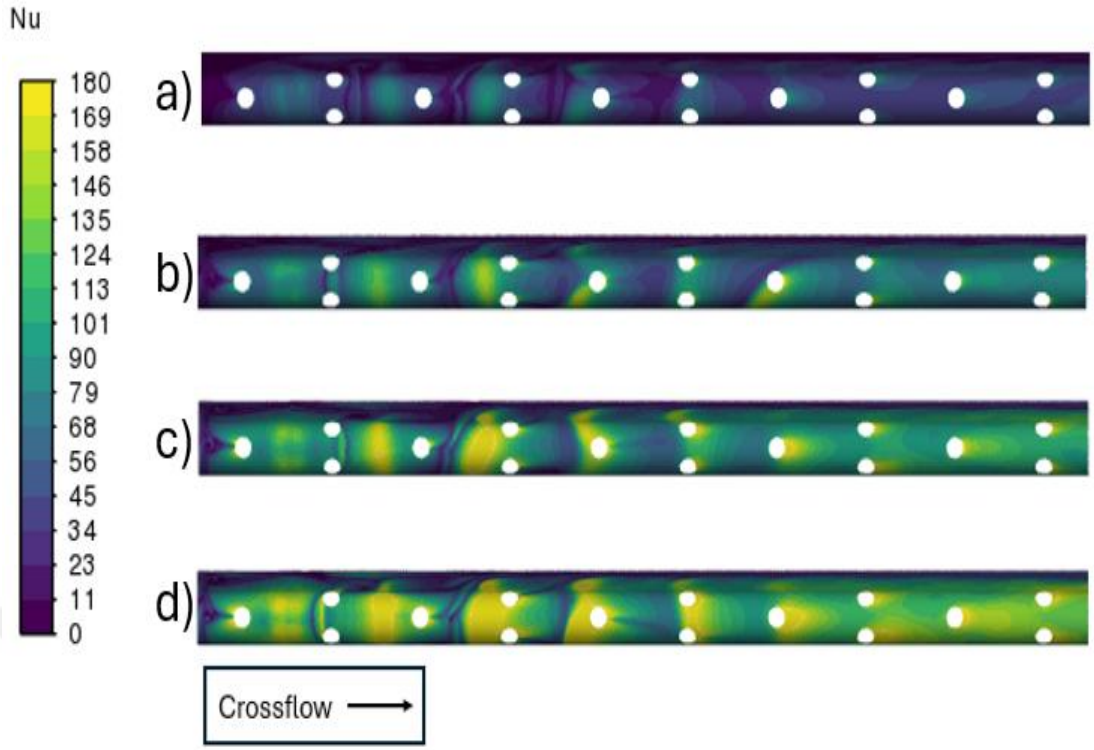

Figure 6.5 : Nu for H/D=2.7, P/D=4: a) $Re_D=10^3$, b) $Re_D=2x10^3$, c) $Re_D=3x10^3$, d) $Re_D=4x10^3$.

6.5 Effect of the Jet-to-Surface Spacing (H/D)

The standoff ratio H/D enters Equation (6.1) with a negative exponent of −0.451, which means that the surface-averaged Nu degrades as the jet exit is moved further from the target. The mechanism is well established in the impingement-cooling literature: as the jet travels a longer distance before striking the wall, viscous diffusion and turbulent mixing broadens the jet, the centerline momentum decays, and the strength of the stagnation region is correspondingly reduced. Conversely, smaller H/D values place the jet exit close enough to the target that the high-momentum core impinges essentially undiluted, generating a sharp stagnation footprint and an energetic radial wall-jet flow. Under high crossflow the situation is exacerbated, because a longer flight path leaves the jet exposed to crossflow deflection for longer, so its trajectory is bent more before it reaches the target and the resulting wall footprint is correspondingly weaker and more spread out. The fractional value of the exponent indicates that this is a moderately strong, non-linear dependence rather than an overwhelming one—H/D matters, but it is secondary to Re_D. The dependence is summarized in Figure 6.6, where Nu is plotted against H/D at fixed P/D = 4 for the four Re_D values of the campaign. The visual comparison is given in Figure 6.7.

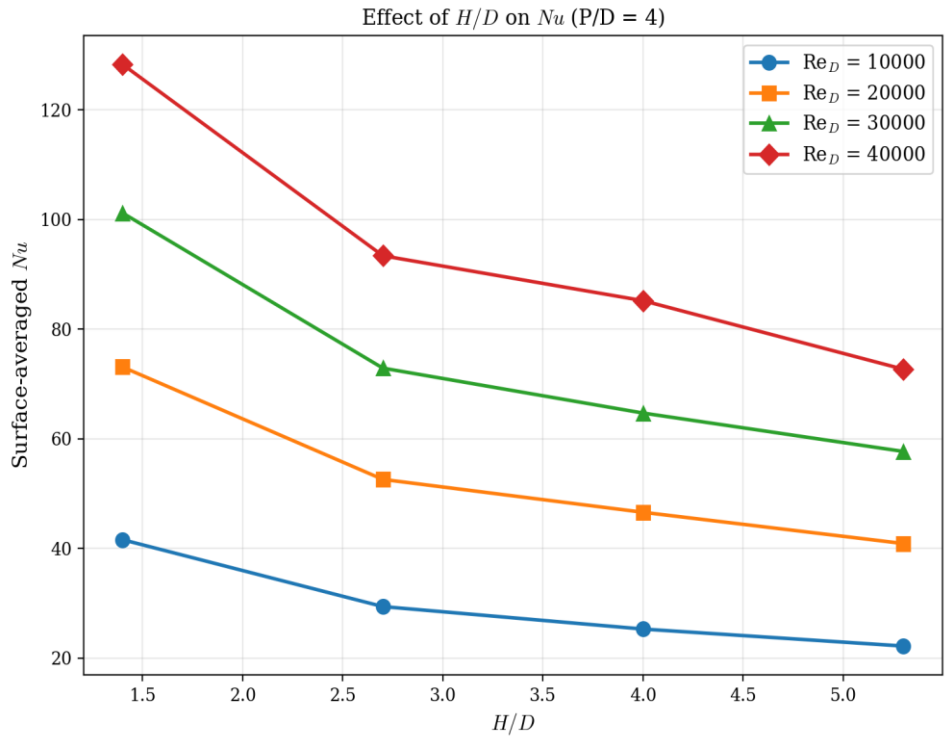

Figure 6.6 : Effect of the jet-to-surface spacing ratio H/D on the surface-averaged Nusselt number for fixed P/D = 4 and varying Re_D.

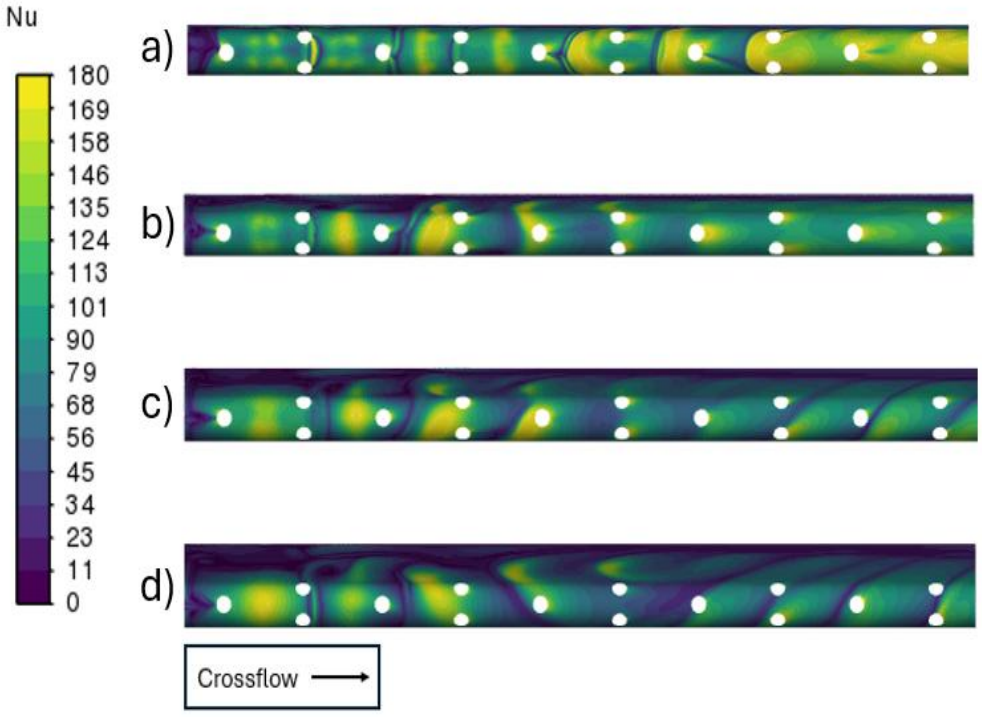

Figure 6.7 : Nu for Re_D=3x10^3, P/D=4: a) H/D=1.4, b) H/D=2.7, c) H/D=4.0, d) H/D=5.3.

6.6 Effect of the Jet-to-Jet Pitch (P/D)

The jet pitch ratio P/D also enters Equation (6.1) with a negative exponent (−0.448). Physically, larger P/D means the impingement jets are spaced further apart, so that the interaction between neighbouring jets is weakened, the collective turbulence level near the wall drops, and the array progressively behaves like a collection of essentially independent single jets. At the smaller pitch values examined, by contrast, adjacent jets sit close enough together that the spent flow from one jet visibly interferes with the next: the resulting fountain-like collisions and the heightened local turbulence both add to the surface heat-transfer rate. The crossflow amplifies this trend further—when the jets are widely spaced, a given jet is more easily diverted by the cross-stream before its neighbours have any chance to brace it, and the wall-normal momentum reaching the target is therefore more strongly reduced. The fact that the H/D and P/D exponents in Equation (6.1) come out almost equal in magnitude suggests that the two geometric parameters end up affecting Nu on a comparable scale, even though the underlying physics differs in each case, momentum dilution along the jet for H/D, versus inter-jet coupling for P/D. The corresponding behaviour is shown in Figure 6.8, where Nu is plotted against P/D at fixed H/D = 2.7 for the four Re_D values. Figure 6.9 visually compares the Nu contours for variable P/D values.

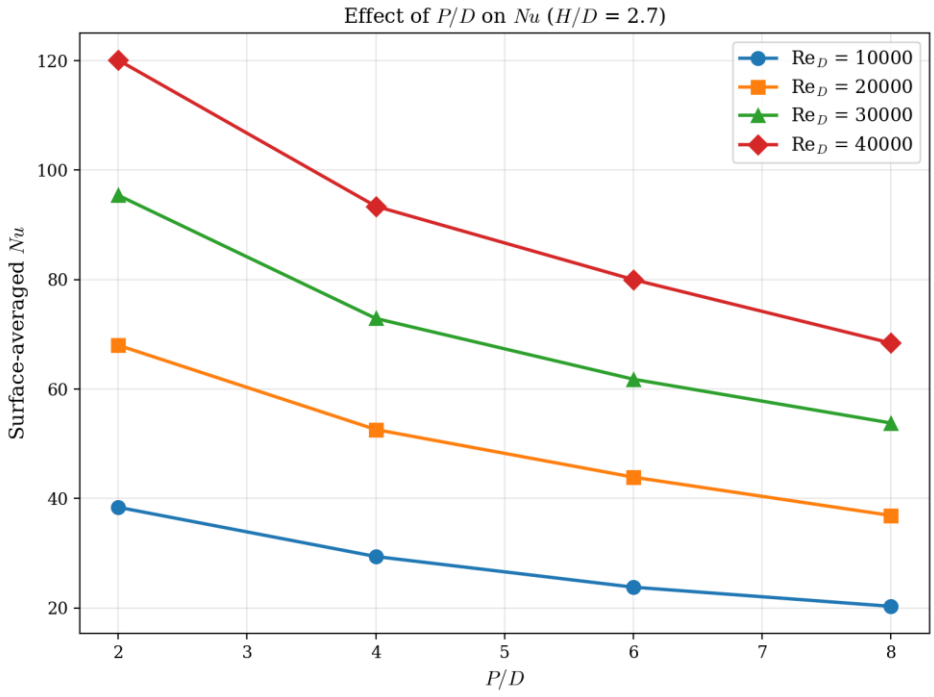

Figure 6.8 : Effect of the jet-to-jet pitch ratio P/D on the surface-averaged Nusselt number for fixed H/D = 2.7 and varying Re_D.

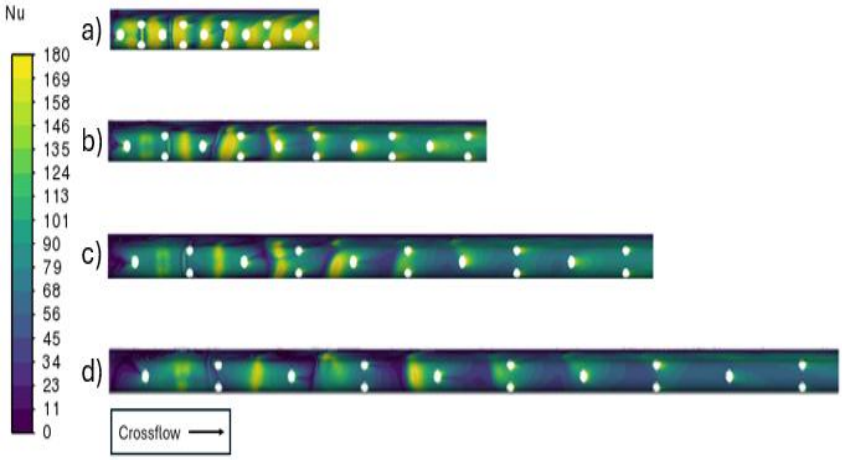

Figure 6.9 : Nu for $Re_D=3x10^3$, H/D=2.7: a) P/D=2, b) P/D=4, c) P/D=6, d) P/D=8.

6.7 Correlation Performance and Physical Consistency

On the present data set, Equation (6.1) reproduces the CFD Nusselt numbers with a mean absolute percentage error of 3.72 % a level of agreement that is acceptable for engineering use. The closed form is compact: a single dimensionless coefficient and three exponents are sufficient to capture the simultaneous influence of jet inertia, jet-to-target standoff, and inter-jet pitch over the entire investigated parameter window. The clear primacy of the Re_D contribution, together with the smaller but still appreciable geometric corrections, mirrors the physical balance among jet momentum, axial diffusion, and the deflection imposed by the crossflow that has been described qualitatively in Chapter 3. The near-equality of the H/D and P/D exponents underscores that, in design practice, both geometric ratios deserve comparable attention, loose pitches and large standoffs each erode the cooling performance, even though they do so through different physical pathways. In order to check the correlation performance, two additional CFD simulations with random parameters within the bound were conducted. Table 6.6 shows the difference between correlation and the real CFD analyses. It can be said that the performance of the correlation is acceptable.

Table 6.6 : Control runs for the correlation.

Re_D	H/D	P/D	Nu Correlation	Nu CFD	Difference
35000	3.5	2.5	93.1	95.2	-2.3%
15000	1.6	7.0	40.4	40.1	0.7%

7. CONCLUSIONS AND RECOMMENDATIONS

The present thesis investigated the convective heat-transfer characteristics of jet impingement cooling inside a generic gas-turbine blade leading-edge passage operated under a strong, persistent crossflow. A three-dimensional steady RANS framework with the k–ω SST turbulence model was developed in Ansys Fluent, validated against the experimental data of Forster and Weigand [8], and applied to a 64-case parametric campaign that covered the jet Reynolds number, the jet-to-surface spacing ratio, and the jet-to-jet pitch ratio. Based on the CFD database thereby generated, a compact engineering correlation was derived for the area-averaged Nusselt number on the impingement target. This final chapter summarizes the principal findings of the study, draws their practical implications, acknowledges the limitations of the adopted approach, and outlines the directions that the author considers most worthwhile for follow-up work.

7.1 Key Conclusions

The principal conclusions drawn from the validation exercise and from the parametric campaign can be stated as follows:

- The validated three-dimensional RANS k–ω SST framework reproduces the spanwise-resolved Nusselt-number distributions reported by Forster and Weigand [8] to within the deviation band that is typical of state-of-the-art impingement simulations, which confirms the adequacy of the closure for the high-crossflow operating window of practical interest.

- Across the entire 64-case design space, the jet Reynolds number Re^D is by far the most influential parameter governing the area-averaged Nusselt number. Its near-unity exponent (n = 0.849) indicates that the heat-transfer augmentation under high crossflow is driven predominantly by jet-inertial effects rather than by turbulent transport alone, and that a more energetic jet partially mitigates the loss of impingement effectiveness caused by crossflow deflection.

- Both geometric ratios exert a moderate, secondary, negative influence on Nu. Increasing the jet-to-surface spacing (H/D) reduces the centreline momentum reaching the target and exposes the jet to a longer crossflow path, both of which weaken the stagnation footprint. Increasing the jet-to-jet pitch (P/D) reduces the number of jets discharging per unit target area and amplifies the row-to-row accumulation of spent crossflow, which similarly degrades the area-averaged response. The fact that the two exponents ($m = -0.451$, $k = -0.448$) come out almost equal in magnitude indicates that, in the high-crossflow regime studied here, the geometric ratios act through closely related mechanisms.

- The proposed empirical correlation (Equation 6.1) reproduces the simulated dependence of Nu on the three governing parameters with engineering accuracy across the full investigated range, with a MAPE of 3.72 % and only a small number of outliers lying outside the ±10 % deviation band. The correlation therefore furnishes a statistically robust and physically reasonable engineering description of the high-crossflow impingement-cooling behaviour.

- Because the correlation is calibrated against a parameter window that already includes the high crossflow accumulation regions of cooled airfoils, it provides a more representative engineering estimate for these regions than do legacy correlations developed under low- or zero-crossflow conditions.

7.2 Practical Implications

From an engineering point of view, the correlation introduced in this thesis can be used at the preliminary-design stage to obtain a rapid first estimate of the area-averaged convective heat-transfer coefficient on an impingement-cooled leading-edge target without the need for a dedicated CFD campaign. Because it has been calibrated within parameter ranges that are representative of contemporary high-pressure turbine cooling layouts and under a crossflow intensity that matches realistic operating conditions, it is particularly suited to the early sizing of jet-plate geometries, to the initial allocation of coolant flow, and to comparative trade-off studies among candidate impingement architectures. Once a configuration has been narrowed down through such preliminary screening, a high-fidelity CFD simulation should still be performed to refine the local heat-transfer prediction and to evaluate the associated pressure

losses, but the correlation considerably reduces the number of CFD runs required to reach a converged design.

Beyond its direct use as a sizing tool, the correlation also provides a useful normalization against which experimental or computational heat-transfer data obtained under similar conditions can be compared. Departures from the correlation can highlight geometric features or operating points whose response differs from the smooth power-law trend captured here and can thereby help the analyst identify configurations that warrant more detailed investigation.

7.3 Recommendations for Future Work

Building on these conclusions, the following directions appear most promising for follow-up work:

- Extending the parameter window. The correlation should be tested, and if necessary recalibrated, for jet Reynolds numbers above 40 000 (which are increasingly relevant for next-generation high-bypass cores) and for jet-to-surface spacings below 1.4 (which arise in tightly packed leading-edge inserts). A wider range of crossflow intensities, including the very low-crossflow regime characteristic of the first impingement row of an array, should also be explored.

- Adding local-scale information. Future work should complement the area-averaged correlation with companion expressions for the peak Nu and for representative spatial moments of the local Nu distribution, so that the engineering description retains the practical compactness of a correlation while also conveying information about local thermal loading.

- Extending the correlation to low- and moderate-crossflow regimes. The present database has been generated at an essentially fixed crossflow intensity close to 60 % of the total inlet mass flow. To broaden the applicability of the proposed correlation, the parametric campaign should be repeated at lower crossflow fractions—for example, around 20 % and 40 % so as to cover the full range from near-quiescent impingement (characteristic of the first row of an array) to the high-crossflow conditions investigated here. Such an extension could be confirmation that a single power-law form remains adequate over a wider envelope. In addition to the medium or low crossflow regimes the range could be extended to zero crossflow condition.

REFERENCES

[1] **Naik, S.** (2017). Basic aspects of gas turbine heat transfer. In Murshed, S. M. S. and Lopes, M. M. (Eds.), *Heat Exchangers – Design, Experiment and Simulation* (ch. 6, pp. 111–143). Rijeka, Croatia: InTech.

[2] **Korpela, S. A.** (2011). *Principles of Turbomachinery*. Hoboken, NJ, USA: John Wiley & Sons.

[3] **Han, J.-C., Dutta, S. and Ekkad, S. V.** (2013). *Gas Turbine Heat Transfer and Cooling Technology* (2nd ed.). Boca Raton, FL, USA: CRC Press, Taylor & Francis Group.

[4] **Bathie, W. W.** (1995). *Fundamentals of Gas Turbines* (2nd ed.). New York, NY, USA: John Wiley & Sons.

[5] **Bunker, R. S.** (2007). Gas turbine heat transfer: Ten remaining hot gas path challenges, *Journal of Turbomachinery, 129*, 193–201.

[6] **Zuckerman, N. and Lior, N.** (2006). Jet impingement heat transfer: physics, correlations, and numerical modeling. In *Advances in Heat Transfer* (Vol. 39, pp. 565–631). Amsterdam, The Netherlands: Elsevier.

[7] **Han, J. C. and Dutta, S.** (2001). Recent developments in turbine blade internal cooling, *Annals of the New York Academy of Sciences, 934*, 162–178.

[8] **Forster, M. and Weigand, B.** (2021). Experimental and numerical investigation of jet impingement cooling onto a concave leading edge of a generic gas turbine blade, *International Journal of Thermal Sciences, 164*, 106862.

[9] **Florschuetz, L. W., Truman, C. R. and Metzger, D. E.** (1981). Streamwise flow and heat transfer distributions for jet array impingement with crossflow, *Journal of Heat Transfer, 103*, 337–342.

[10] **Han, J. C.** (2004). Recent studies in turbine blade cooling, *International Journal of Rotating Machinery, 10*, 443–457.

[11] **Martin, H.** (1977). Heat and mass transfer between impinging gas jets and solid surfaces. In Irvine, T. F. and Hartnett, J. P. (Eds.), *Advances in Heat Transfer* (Vol. 13, pp. 1–60). New York, NY, USA: Academic Press.

[12] **Viskanta, R.** (1993). Heat transfer to impinging isothermal gas and flame jets, *Experimental Thermal and Fluid Science, 6*, 111–134.

[13] **Chupp, R. E., Helms, H. E., McFadden, P. W. and Brown, T. R.** (1969). Evaluation of internal heat-transfer coefficients for impingement-cooled turbine airfoils, *Journal of Aircraft, 6*, 203–208.

[14] **Kercher, D. M. and Tabakoff, W.** (1970). Heat transfer by a square array of round air jets impinging perpendicular to a flat surface including the effect of spent air, *Journal of Engineering for Power, 92*, 73–82.

[15] **Metzger, D. E. and Korstad, R. J.** (1972). Effects of crossflow on impingement heat transfer, *Journal of Engineering for Power, 94*, 35–41.

[16] **Jambunathan, K., Lai, E., Moss, M. A. and Button, B. L.** (1992). A review of heat transfer data for single circular jet impingement, *International Journal of Heat and Fluid Flow, 13*, 106–115.

[17] **Weigand, B. and Spring, S.** (2011). Multiple jet impingement – A review, *Heat Transfer Research, 42*, 101–142. (Also: Proc. Int. Symp. on Heat Transfer in Gas Turbine Systems, Antalya, Turkey, August 2009.)

[18] **Cooper, D., Jackson, D. C., Launder, B. E. and Liao, G. X.** (1993). Impinging jet studies for turbulence model assessment – I. Flow-field experiments, *International Journal of Heat and Mass Transfer, 36*, 2675–2684.

[19] **Goldstein, R. J. and Franchett, M. E.** (1988). Heat transfer from a flat surface to an oblique impinging jet, *Journal of Heat Transfer, 110*, 84–90.

[20] **Goldstein, R. J. and Behbahani, A. I.** (1982). Impingement of a circular jet with and without cross flow, *International Journal of Heat and Mass Transfer, 25*, 1377–1382.

[21] **Metzger, D. E., Baltzer, R. T. and Jenkins, C. W.** (1972). Impingement cooling performance in gas turbine airfoils including effects of leading edge sharpness, *Journal of Engineering for Power, 94*, 219–225.

[22] **Bunker, R. S. and Metzger, D. E.** (1990). Local heat transfer in internally cooled turbine airfoil leading edge regions: Part I – Impingement cooling without film coolant extraction, *Journal of Turbomachinery, 112*, 451–458.

[23] **Madwesh, N., Purohit, S. and Karanth, K. V.** (2023). Computational flow and heat transfer study on impingement cooling in a turbine blade leading edge using an innovative convergent nozzle, *Journal of the Brazilian Society of Mechanical Sciences and Engineering, 45*, 86.

[24] **Florschuetz, L. W., Berry, R. A. and Metzger, D. E.** (1980). Periodic streamwise variations of heat transfer coefficients for inline and staggered arrays of circular jets with crossflow of spent air, *Journal of Heat Transfer, 102*, 132–137.

[25] **Florschuetz, L. W., Metzger, D. E. and Su, C. C.** (1984). Heat transfer characteristics for jet array impingement with initial crossflow, *Journal of Heat Transfer, 106*, 34–41.

[26] **Hollworth, B. R. and Cole, G. H.** (1987). Heat transfer to arrays of impinging jets in a crossflow, *Journal of Turbomachinery, 109*, 564–571.

[27] **San, J. Y. and Lai, M.-D.** (2001). Optimum jet-to-jet spacing of heat transfer for staggered arrays of impinging air jets, *International Journal of Heat and Mass Transfer, 44*, 3997–4007.

[28] **Amano, R. S. and Sundén, B. (Eds.).** (2014). *Impingement Jet Cooling in Gas Turbines* (Developments in Heat Transfer Series). Southampton, UK: WIT Press.

[29] **Miao, J.-M., Wu, C.-Y. and Chen, P.-H.** (2009). Numerical investigation of confined multiple-jet impingement cooling over a flat plate at different

crossflow orientations, *Numerical Heat Transfer, Part A: Applications, 55*, 1019–1050.

[30] **Wang, L., Sundén, B., Borg, A. and Abrahamsson, H.** (2011). Heat transfer characteristics of an impinging jet in crossflow, *Journal of Heat Transfer, 133*, 121701.

[31] **Ansys, Inc.** (2026). *Ansys Fluent Theory Guide, Release 2026 R1*. Canonsburg, PA, USA: Ansys, Inc.

[32] **Menter, F. R.** (1994). Two-equation eddy-viscosity turbulence models for engineering applications, *AIAA Journal, 32*, 1598–1605.

[33] **Behnia, M., Parneix, S. and Durbin, P. A.** (1998). Prediction of heat transfer in an axisymmetric turbulent jet impinging on a flat plate, *International Journal of Heat and Mass Transfer, 41*, 1845–1855.

CURRICULUM VITAE

Name Surname **:** Sefa YILMAZ

EDUCATION **:**

- **B.Sc.** **:** 2019, Istanbul Technical University Faculty of Mechanical Engineering, Mechanical Engineering

PROFESSIONAL EXPERIENCE AND REWARDS:

- 2023-Ongoing: TRMOTOR Power Systems, Turbine Aerodynamics Engineer
- 2021-2023: TUSAŞ Engine Industries, Thermal System Design Engineer

PUBLICATIONS, PRESENTATIONS AND PATENTS ON THE THESIS:

- **Yilmaz, S., Cadirci, S.** 2026: Computational Fluid Dynamics Simulations for Turbine Blade Cooling Using Jet Impingement. CMES 2026, April 24-26, 2026, Istanbul, Turkey. (Online)